Title
Voltage-Controlled Magnetic Dynamics in Nanoscale Magnetic Tunnel Junctions

Author
Alzate Vinasco, Juan Guillermo

Publication Date
2014

Peer reviewed|Thesis/dissertation

UNIVERSITY OF CALIFORNIA

Los Angeles

Voltage-Controlled Magnetic Dynamics in Nanoscale Magnetic Tunnel Junctions

A dissertation submitted in partial satisfaction of the

requirements for the degree Doctor of Philosophy

in Electrical Engineering

by

Juan Guillermo Alzate Vinasco

2014

ABSTRACT OF THE DISSERTATION

Voltage-Controlled Magnetic Dynamics in

Nanoscale Magnetic Tunnel Junctions

by

Juan Guillermo Alzate Vinasco

Doctor of Philosophy in Electrical Engineering

University of California, Los Angeles, 2014

Professor Kang L. Wang, Chair

Spintronic devices, i.e., those utilizing the interaction of magnetic moments with electric voltages and currents in magnetic nanostructures, offer an exceptionally promising set of candidates for future electronic memory needs. Recently, the possibility of reversing the magnetization of nanoscale magnetic tunnel junction (MTJ) devices using the spin transfer torque (STT) effect has attracted the attention of industry and academia, since STT-MRAM has been demonstrated to be a strong candidate for a high speed, high density, and high endurance nonvolatile memory. Further, by replacing the current-driven (e.g., STT) switching mechanism for a voltage-controlled effect, a novel magnetoelectric RAM (MeRAM) architecture could result in considerable improvements in terms of density and dissipated energy during switching, both factors which are limited in STT-MRAM by the large currents required.

In this dissertation, the possibility of exploiting the voltage-controlled magnetic anisotropy (VCMA) effect on nanoscale MTJ devices as the driving mechanism for MeRAM will be introduced. Experimental results on the demonstration of current-assisted and purely voltage-controlled switching in the thermally-activated and precessional regimes are presented. The write energies in VCMA-driven switching of nanoscale MTJs are shown to be at least one order of magnitude smaller compared to STT-based schemes. The advantages and challenges in terms of scalability and energy-efficiency of this voltage-driven approach are discussed. Further, a compact model for co-simulation of VCMA-driven MTJs with CMOS is established and validated against experimental data. The compact model is refined by the parameters extracted from a detailed characterization of the voltage-driven dynamics in these devices. This includes experimental results on the accurate characterization of the temperature dependence of the perpendicular anisotropy and the VCMA effect in MTJs, as well as on the influence of higher order anisotropies over MTJ dynamics measured via ferromagnetic resonance (FMR).

The dissertation of Juan Guillermo Alzate Vinasco is approved.

Yaroslav Tserkovnyak

Dejan Markovic

Kang L. Wang, Committee Chair

University of California, Los Angeles

2014

To my family

"Esto es por y para ustedes"

This dissertation is specially dedicated to the memory of my beloved uncle

"¿Q' hubo mijo?"

TABLE OF CONTENTS

LIST OF FIGURES

LIST OF TABLES

ACKNOWLEDGMENTS

First and foremost, I would like to thank my advisor, Prof. Kang L. Wang. My PhD journey under his guidance started with an interview on Dec 21, 2007. Now, almost seven years later, I only have a deep feeling of gratitude for the opportunity to carry my studies in his group and to learn from him as one of the best technologists for emerging devices in nanoelectronics. His vision about technologies pertaining future needs was a major point of this dissertation, starting from conversations very early in my PhD where he insisted on the need to move to electric-field-controlled magnetism. Prof. Wang's passion for science, technology and for his work is a lesson for all of us who have had the opportunity to join his research group.

I would also like to deeply thank my "co-advisor in the dark", Prof. Pedram Khalili Amiri. Pedram is not officially listed as a committee member for this dissertation since he just recently got the well-deserved title of Professor, but he was a fundamental part of this project. Pedram and I joined Prof. Wang's lab within a three-month difference, and had to start the MTJ program from scratch, including setting up probe stations and simulation environments for research in the area. I will always be grateful for his advises, energy and the hour-long discussions in front of the board of his office trying to decrypt the physics behind domain walls and canted states.

There are two other persons who were critical part of this project: First, Dr. Sergiy Cherepov, one of the most skilled experimentalists I have met so far. He taught me a lot about experiments, while providing his friendship accompanied by invaluable support and guidance for my PhD. Second, I would like to acknowledge Pramey Upadhyaya, who was the theory "side-kick" of this project, teaching me a lot of the physics of magnetism with his pristine vision, passion and understanding of engineering physics.

One of the advantages of being in Prof. Wang's lab was the opportunity to work in big projects where I got to develop fantastic collaborations for my PhD. First, I would like to acknowledge Dr. Juergen Langer and Dr. Berthold Ocker from Singulus AG for film deposition and Dr. Jordan Katine at HGST for nanoscale device patterning. Out of the great collaborators I could share valuable time with, I have the honor to have two as part of my PhD committee: Prof. Tserkovnyak and Prof. Markovic who, from completely different perspectives, have taught me the physics and circuit implications that bridge theoretical spintronics to the possibility of a real device, respectively. Also, I would like to acknowledge Prof. Ilya Krivorotov, I will always be impressed by how Prof. Krivorotov can explain such complicated stuff in such simple words.

I would also like to thank Prof. Oscar Stafsudd for being part of my committee. He is one of the icons of the EE department in UCLA, teaching grad students like me how to be successful by combining simultaneous passion for research and teaching. Big thanks also to the members of the sub-team on spintronics in the Device Research Laboratory (DRL) directed by Prof. Wang!

Obviously, it would not have been possible to live in LA as a grad student without financial support. During my M.S./PhD course, I acknowledge funding from different projects, starting from the MURI program on spin-waves on nanoparticles, then the DARPA STT-MRAM program, followed by the DARPA Non-volatile logic program, then the NSF TANMS center at UCLA (astoundingly directed by Prof. Carman, another great collaborator for this project), and finally, my last year of PhD was supported by the Qualcomm Innovation Fellowship. Thanks!

Last but not least, a big part of this and everything in my life comes down to the people who surrounded and supported me at many (many) times I lost confidence I would reach the end goal: Mama, Papa, Maria, Golita, uncles, aunts and cousins, Jennifer and my dearest friends… Gracias totales! Esto es por y para ustedes!

VITA

Education

2008-2011	M.S., Electrical Engineering University of California, Los Angeles, United States
2002-2007	B.S., Physics (*Summa Cum Laude*) Universidad de los Andes, Bogota, Colombia
2002-2007	B.S., Electronics Engineering (*Summa Cum Laude*) Universidad de los Andes, Bogota, Colombia

Employment history

2010	Graduate Research Intern – Components Research Group Intel Corporation, Hillsboro, Oregon, United States

Selected journal publications and conference presentations

- **J.G. Alzate**, P. Khalili Amiri, P. Upadhyaya, S.S. Cherepov, J. Zhu, M. Lewis, R. Dorrance, J.A. Katine, J. Langer, K. Galatsis, D. Markovic, I. Krivorotov and K.L. Wang, "Voltage-Induced Switching of Nanoscale Magnetic Tunnel Junctions", Technical Digest of the IEEE International Electron Devices Meeting (IEDM 2012), San Francisco, California, pp. 681-684, December 2012.

- **J.G. Alzate**, P. Khalili Amiri, G. Yu, P. Upadhyaya, J.A. Katine, J. Langer, B. Ocker, I.N. Krivorotov and K.L. Wang, "Temperature Dependence of the Voltage-Controlled Perpendicular Anisotropy in Nanoscale MgO|CoFeB|Ta Magnetic Tunnel Junctions", Applied Physics Letters, Vol. 104, No. 11, pp. 112410/1-5, 2014.

- **J.G. Alzate**, P. Khalili Amiri, P. Upadhyaya, S.S. Cherepov, J. Zhu, J.A. Katine, J. Langer, B. Ocker, I.N. Krivorotov and K.L. Wang, "Voltage-Induced Dynamics in Nanoscale Magnetic Tunnel Junctions: Higher-order Anisotropy Contributions to Ferromagnetic Resonance and Switching", Book of digests of IEEE International Magnetics Conference (Intermag 2014), p. AH-10, Dresden, Germany, May 2014. ***(Awarded Best Student Presentation Award)***

- **J.G. Alzate**, A. Kovalev, G. Rowlands, P.K. Amiri, Y. Tserkovnyak, I. Krivorotov, T. Rahman, A. Lyle, J.-P. Wang, K. Galatsis and K.L. Wang, "Micromagnetic States of Magnetic Tunnel Junction Memory Cells with Perpendicular Polarizer", Book of abstracts of 55th Conference on Magnetism and Magnetic Materials (MMM 2010), FC-02, Atlanta, Georgia, USA, November 2010.

- K.L. Wang, **J.G. Alzate** and P. Khalili Amiri, "Low-Power Nonvolatile Spintronic Memory: STT-RAM and Beyond", Journal of Physics D: Applied Physics, Vol. 46, No. 7, pp. 074003, 2013.

- R. Dorrance, **J.G. Alzate**, S.S. Cherepov, P. Upadhyaya, I.N. Krivorotov, J.A. Katine, J. Langer, K.L. Wang, P. Khalili Amiri and D. Markovic, "A Diode-MTJ Crossbar Memory Cell Using Voltage-Induced Unipolar Switching for High-Density MRAM", IEEE Electron Device Letters, Vol. 34, No. 6, pp. 753-755, 2013.

- A. Khitun, **J.G. Alzate**, P. Upadhyaya, M. Lewis, J. Nath, Y.T. Lin, K. Wong, S. Cherepov, P. Khalili Amiri, K. L. Wang, J. Hockel, G.P. Carman, J. Zhu, Y-J Chen, I. N. Krivorotov, J. Katine, J. Langer, P. Shabadi, S. Khasanvis, S. Narayanan and C. A. Moritz, "Spin Wave Nanofabric Update", IEEE/ACM International Symposium on Nanoscale Architectures (NANOARCH '12), Amsterdam, The Netherlands, July 2012.

- S. Cherepov, P. Khalili Amiri, **J.G. Alzate**, K. Wong, M. Lewis, P. Upadhyaya, J. Nath, M. Bao, A. Bur, T. Wu, G.P. Carman, A. Khitun and K.L. Wang, "Electric-field-induced spin wave generation using multiferroic magnetoelectric cells", Applied Physics Letters, Vol. 104, No. 8, pp. 082403/1-5, 2014.

- P. Khalili Amiri, P. Upadhyaya, **J.G. Alzate** and K.L. Wang, "Electric-Field-Induced Thermally-Assisted Switching of Monodomain Magnetic Bits", Journal of Applied Physics, Vol. 113, No. 2, pp. 013912, 2013.

- G. Yu, P. Upadhyaya, Y. Fan, **J.G. Alzate**, W. Jiang, K.L. Wong, S. Takei, S.A. Bender, L.T. Chang, Y. Jiang, M. Lang, J. Tang, Y. Wang, Y. Tserkovnyak, P. Khalili Amiri, K.L. Wang, "Switching of perpendicular magnetization by spin-orbit torques in the absence of external magnetic fields", Nature Nanotechnology, doi:10.1038/nnano.2014.94, May 2014.

- P.V. Ong, N. Kioussis, P. Khalili Amiri, **J.G. Alzate**, K.L. Wang, G.P. Carman, J. Hu and R. Wu, "Electric field control and effect of Pd capping on magnetocrystalline anisotropy in FePd thin films: A first-principles study", Physical Review B, Vol. 89, No. 9, pp. 094422/1-8, 2014.

- J. Zhu, J.A. Katine, G.E. Rowlands, Y.-J. Chen, Z. Duan, **J.G. Alzate**, P. Upadhyaya, J. Langer, P. Khalili Amiri, K.L. Wang and I.N. Krivorotov, "Voltage-Induced Ferromagnetic Resonance in Magnetic Tunnel Junctions", Physical Review Letters, Vol. 108, No. 19, pp. 197203/1-5, 2012.

Patents

- **J.G. Alzate**, P. Khalili Amiri and K.L. Wang, "Voltage-Controlled Magnetic Memory Element with Canted Magnetization", U.S. provisional patent 61/734,922.

- H. Lee, **J.G. Alzate**, P. Khalili Amiri and K.L. Wang, "Fast and Low-Power Sense Amplifier and Wrting Circuit for High-Speed MRAM", UCLA Case No. 2014-834.

CHAPTER 1: Introduction

1.1 From vacuum tubes to instant-on electronics

The history of electronics is one of the many examples of the capacity of human creativity and innovation. The advent of quantum mechanics at the early stage of the twentieth century opened the door to the invention of the transistor, and in little more than sixty years, the constant evolution of the transistor and related electronic devices (e.g., memory elements) has allowed a major transformation of our society, where such devices have penetrated the daily life of human beings, impacting the way we work, communicate, compute and even entertain ourselves.

At the same time, the field of electronics is one of the fastest paced in science and technology, driven by the never-ending demand for increased computing power and storage capacity. In less than a century of existence, we have already experienced two major technology changes [1], largely to overcome power-bottleneck issues, while the end of the current era of classical CMOS scaling seems to be quickly approaching [2]. As illustrated on Fig. 1.1, electronics has moved in such period from vacuum tubes to Bipolar Junction Transistors (BJTs) to Complementary Metal Oxide Semiconductor (CMOS) as the building block for electronic devices, where each transition has been accompanied by lessons that have become key to the development of the field. For example, when technology moved from vacuum tubes to BJTs, we learnt that having smaller, scalable devices was essential in order to build complex systems with increased computing capacities, and such systems should use small currents for density and power considerations. A critical transition then happened when BJTs were mostly replaced by CMOS, marked by a key insight for the future of electronic devices: Electric-field-controlled

devices (e.g., CMOS, controlled by voltages in the gate) allow for more energy efficient devices as compared to current-controlled devices (e.g., BJTs, "gated" by a base current). The capacitive mechanism of control in the gate of the CMOS has been one of the main reasons of the success of such technology, allowing integrating more than a billion transistors in a chip, while dissipating just enough power to still make it portable for computers and smartphones, and viable in terms of heat management (i.e., cooling, refrigeration and reliability of the systems) and other key system metrics.

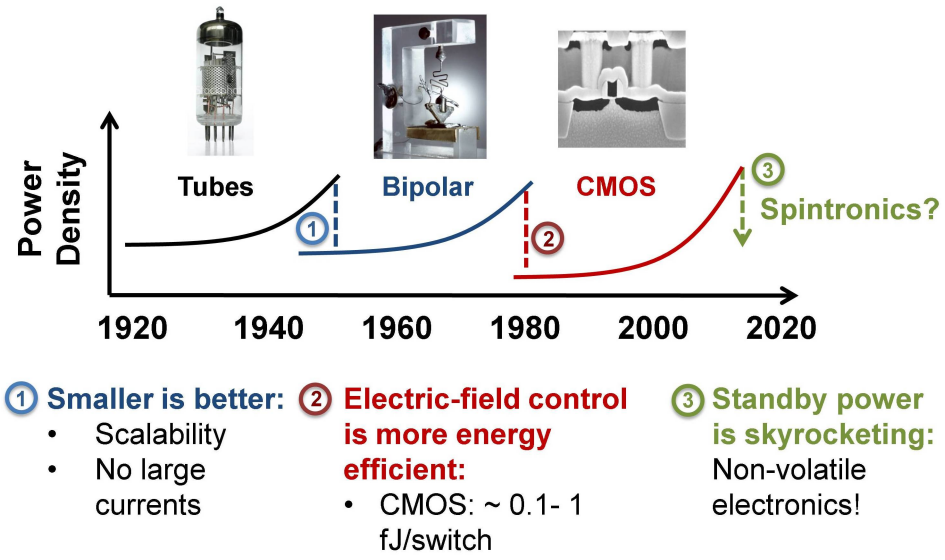

Fig. 1.1 In less than a century of existence, the field of electronics has already experienced two major technology changes, while the end of era of classical CMOS scaling seems to be quickly approaching. Each technology change has been marked by key findings to the progress of the field. Currently, the quest is to find a scalable device controlled by electric fields, in order to have low dynamic power dissipation, while being non-volatile to eliminate standby power. Spintronics is one of the candidates to accomplish such goal.

CMOS is currently the dominating semiconductor technology, where its success has been well outlined by the aggressive scaling predicted in Moore's law [3], pushing the channel of the transistor down to fewer than 200 atoms in length in the 22-nn node, and with strong prospects to

reach sub-10 nm nodes before 2018 [4]. However, the scaling of CMOS has also resulted in several challenges and issues, including [4, 5]: (1) the fundamental problem of running out of atoms in the channel, reaching quantum regimes and losing electrostatic control of the electrons travelling in the channel by the gate, (2) the increase in the cost per gate for smaller technology nodes (opposite to the desired trend via scaling), a consequence of the additional processes and innovations required in patterning and architecture itself of the device in order to make the scaled CMOS functional, and (3) power bottle-neck issues, resulting in an rapid increase of the dissipated power density, as outlined in Fig. 1.1. For the latter, Fig. 1.2 shows the trend of the increase of the dynamic and static (standby) power as a function of technology node. It can be clearly observed that, for small technology nodes, the static power dissipation becomes dominant due to the increase in leakage currents [6], motivating the need for non-volatile devices and circuits that could be incorporated next to the inherently volatile CMOS to alleviate this problem. For example, the integration of a fast, energy-efficient non-volatile memory technology with CMOS can make electronic products non-volatile at the transistor, gate, circuit and system levels, hence allowing for continued scaling with improved energy efficiency by eliminating static power dissipation, and leading to instant-on electronic devices, where the information will remain stored in the non-volatile devices while the system is off, and will be readily available and instantaneously restored at the moment of restarting the system [7].

Nevertheless, the challenges faced by CMOS have opened a big opportunity in the device community to look for alternative systems that could complement or help CMOS continue its "scaling", probably redefining its meaning and focusing on delivering more energy efficient systems with increased functionalities [8], or even going beyond CMOS, creating a new paradigm in electronics with new state variables, architectures and/or devices [2]. In both of

these scenarios, spintronics, i.e., utilizing the fundamental interaction of magnetic moments with electric voltages and currents, has been considered one of the strongest candidates for CMOS-compatible and beyond CMOS computation due to its intrinsic possibility to engineer non-volatile systems with ultralow power devices dissipation. In the next section, the concept of spintronics is briefly introduced.

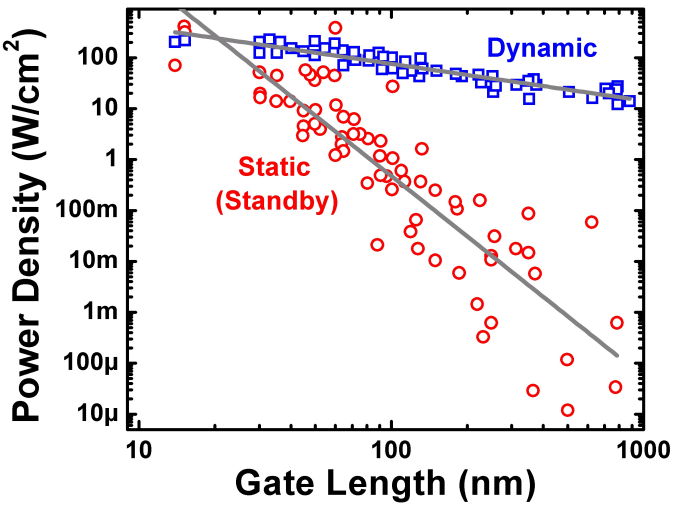

Fig. 1.2 As the CMOS transistor is scaled down, the loss of electrostatic control of the gate translates into a drastic increase of the dissipated static power density. The scaling trend shows how static power has become a major component into the total dissipated power for current technology nodes. This is one of the motivations for non-volatile electronics: Alleviating the static power dissipation problem and allowing for instant-on electronics (Modified from Ref. [6]).

1.2 A short introduction to spintronics

Spintronics is an active and growing area of research and development (R&D) where the spin degree of freedom in condensed matter is exploited to engineer electronic devices for computation, sensing and storage. Although the exploration of magnetic phenomena in nature can be traced back to before 600 BC [9], the theoretical foundation behind the concept of spin in quantum mechanics, and the physics of magnetic materials, have been laid down only in the last

century, giving rise to the birth of spintronics with the discovery of the giant magnetoresistance (GMR) effect by Nobel laureates Prof. Peter Grunberg [10] and Prof. Albert Fert [11] in 1986 and 1988, respectively.

Using spin-based state variables/information carriers for electronic devices provides intriguing opportunities compared to CMOS (or charge-based approaches in general), making spintronics a viable and interesting approach for beyond CMOS as discussed in the previous section. For example, ferromagnetic materials can be engineered to provide non-volatile magnetization states with zero standby power dissipation, making them ideal to construct memory devices. Also, the use of spin-waves [12, 13] or pure spin currents [14] can eliminate the power dissipation due to ohmic losses or Joule heating resulting from the flow of charge currents, and could translate into much more energy efficient devices for logic like spin-wave-based logic gates [15, 16] or the spinFET [17]. Further, by going into Quantum Hall regime [18] or exploiting non-trivial topologies (e.g., topological insulators) [19], completely dissipation-less spin currents or novel electromagnet phenomena emerge, opening the door for systems with ultimate energy efficiency or sensors with novel coupling between electric and magnetic fields respectively [20]. Fig. 1.3 provides a summary of the state variables/information carriers mostly used currently in spintronics, along the most common spintronics devices.

Albeit its fascinating advantages, most of the spintronics devices have important challenges to overcome before they can become marketable. In particular, many of the demonstrations of spin-based devices are limited to very small signals, only detectable in laboratory settings, or at low temperatures, both of these limiting the possibility to connect millions or billions of those devices while operating around room temperature. Furthermore, before any major and substantial technological revolution that moves displays, sensors and other

complementary electronic devices also to the spin domain, spintronics devices must develop efficient mechanisms to translate signals from the spin to the electrical domain and vice versa. The most frequently used mechanisms for inputs/control (electrical to spin) and outputs (spin to electrical domain) are also summarized in Fig. 1.3.

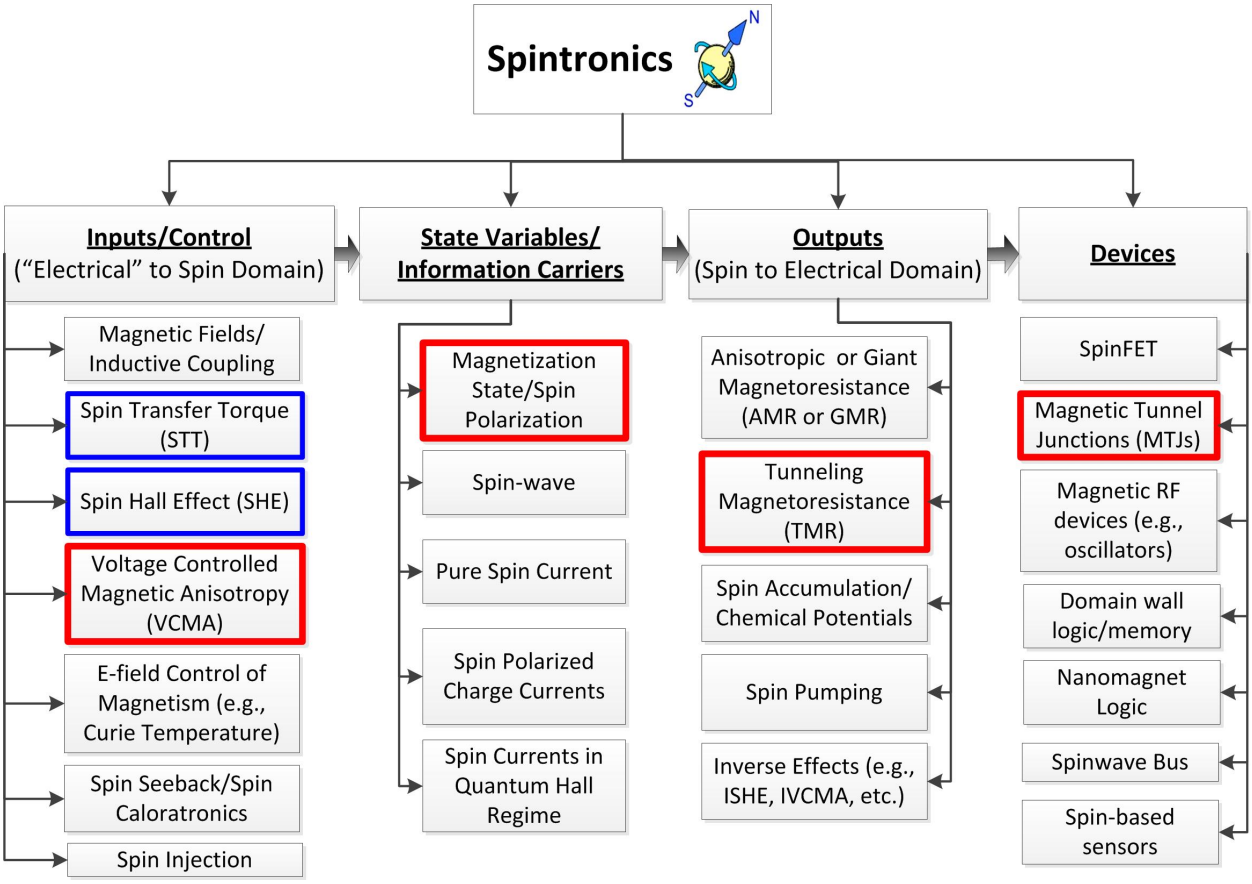

Fig. 1.3 Summary of the most frequent phenomena, state variables and devices in spintronics. In order to exploit the advantages of the spin-based state variables/information carriers, and build viable spintronic devices, efficient mechanisms to translate signals from the electrical to the spin domain (Inputs/Control), and from the spin to electrical domain (Outputs) are required. Highlighted in red and blue are the concepts that are exploited throughout this work and benchmarked against, respectively.

One of the major challenges being currently explored in spintronics is how to efficiently convert spin signals, or magnetization states, to the electrical domain (Output mechanisms in Fig.

1.3). Whereas phenomena like spin accumulation/detection (see Chapter 6 of Ref. [21]), spin pumping [22] and the inverse effects (e.g., inverse spin Hall effect [23]) produce voltages with very low signal to noise ratio at room temperature for practical purpose, the usage of the anisotropic or giant magnetoresistance (AMR or GMR) effects (see Chapter 2 of Ref. [24]) is also limited by the small on/off ratio obtained in both cases [25]. However, the discovery of the larger tunneling magnetoresistance (TMR) effect in magnetic tunnel junctions (MTJs) [26, 27] opened the door for MTJs to be used as a viable option with a reliable read-out (e.g., output) mechanism. The TMR effect is small under practical conditions as of now compared to transistors and other charge-based memory devices, where the maximum on/off ratio of the TMR effect is 2 or 3 (corresponding to TMR ratios of 100% to 200% respectively, see section 1.3) versus on/off ratios of orders of magnitude in charge-based devices. However, the TMR effect is the mechanism in spintronics that provides the largest signal to noise ratio as an output so far, in a range usable for products integrating large number of MTJ devices with CMOS transistors. In fact, MTJs using the TMR effect for read-out have become the cornerstone of the few commercial spintronics devices in the market, including magnetic random access memory (MRAM) and magnetic sensors, such as the read head in hard disks. This is one of the reasons why this dissertation concentrates on magnetic tunnel junctions. Consequently, the next section will describe the structure and physics of MTJ devices, including the TMR effect.

In terms of converting electrical signals to the spin domain (Inputs/Control in Fig. 1.3), it is desirable to use currents or voltages to control the magnetization dynamics in the devices instead of using magnetic fields for this purpose. Magnetic fields couple naturally to magnetic phenomena and, for this reason, they were mostly used in the past to control magnetic materials. However, generating magnetic fields to drive spintronics devices, especially on-chip, usually

requires large currents, greatly reducing the energy efficiency and scalability of the systems (see for example the discussion on field-driven MRAM on section 1.5). Therefore, there are multiple interesting efforts to couple "electrical" and spin domains currently on-going [28] such as trying to improve the electrical spin injection into magnetic nanostructures [29], controlling the magnetization via spin caloritronics [30] (e.g., via the spin Seeback effect), modifying the magnetic properties of materials using currents or electric fields (e.g., turning on/off the ferromagnetism by depleting/accumulating charge carriers in diluted magnetic semiconductors [31]), etc., all of them being currently in early research stages. On the other hand, the discovery of the spin transfer torque (STT) effect [32, 33] spurred a major revolution in the field, allowing controlling magnetization dynamics using spin-polarized charge currents, and resulting in a reliable mechanism to induce switching, oscillations and other interesting magnetic dynamics in spintronics devices, including MTJs [34, 35]. The success of STT has been accompanied by the emergence of STT-MRAM as a strong candidate for a non-volatile memory in embedded or stand-alone applications [36]. The usage of the STT effect to generate switching in MTJ devices and STT-MRAM technology will be discussed in section 1.6. Further, the recent discovery of the giant spin Hall effect (SHE) in materials with a high spin-orbit coupling (SOC) [37, 38] (also called spin orbitronics) provides an additional mechanism to control magnetization dynamics, with the possibility to reduce the relatively large currents required in STT-based phenomena by, at least, one order of magnitude. A short discussion on SHE is presented in section 1.7.

Nevertheless, both STT and SHE effects are based on the flow of charge currents, and therefore, the energy required to control the magnetization of the devices is still governed by undesired ohmic losses. Following the lessons learnt from the BJT to CMOS transition (see Fig. 1.1), replacing charge-driven control mechanisms (STT or SHE) by an electric-field-driven

effect would result, not only in an increase of the energy efficiency of the device, but also in other advantages that will be discussed later in this work in terms of scalability and cell size of a possible memory architecture. Although there are currently different approaches on how to control magnetism with electric fields [28, 39], this dissertation concentrates on exploring and utilizing the voltage-controlled magnetic anisotropy (VCMA) effect [40-43] observed in MTJ devices. The physics of the VCMA effect, its detailed characterization in nanoscale MTJ devices and the usage of VCMA to induce switching for memory applications will be presented starting Chapter 2 of this dissertation.

1.3 Magnetic tunnel junctions (MTJs) and the tunneling magnetoresistance (TMR) effect

Magnetic tunnel junctions (MTJs) are very likely the most successful spintronics device so far, emerging as the preferred building block of spintronics circuits mostly due to their large tunneling magnetoresistance (TMR) ratios (thus, allowing a large read-out signal), and the possibility of integration with conventional semiconductor electronics [44]. Although a real MTJ device is composed by a "sandwich" of many thin film layers, the "heart" of an MTJ is rather simple: It is composed by two ferromagnetic layers, one with a magnetization which is fixed in a given direction (called "fixed layer"), and a second layer with a magnetization that can point at equilibrium either parallel or antiparallel to the fixed layer (called "free layer"), both of them separated by a non-magnetic tunneling oxide. Fig. 1.4(a) and (b) shows the concept schematically and presents a typical resistance versus magnetic field (R-H) loop measured for an MTJ device, where it can be clearly observed that the state of the free layer with respect to the fixed layer can be extracted by determining the electrical resistance of the device. Specifically,

the resistance is minimum when the fixed and free layer are parallel (P) to each other (R_P for the P state), and it switches to a maximum value once the free layer becomes anti-parallel (AP) to the fixed layer (R_{AP} for the AP state). The TMR ratio is therefore defined as

$$TMR = \frac{R_{AP} - R_P}{R_P} \tag{1.1}$$

The change of the resistance depending on the relative alignment of the free and fixed layers in MTJs is due to the tunneling magnetoresistance (TMR) effect. The TMR effect was initially proposed by Jullière in 1975 [45], but its practical realization did not come until 1995 with the demonstration of a TMR ratio of up to 12% in CoFe|Al_2O_3|Co [46] and 18% in Fe|Al_2O_3|Fe [47] at room temperature, in both cases using ultrathin amorphous Al-O as a tunneling barrier.

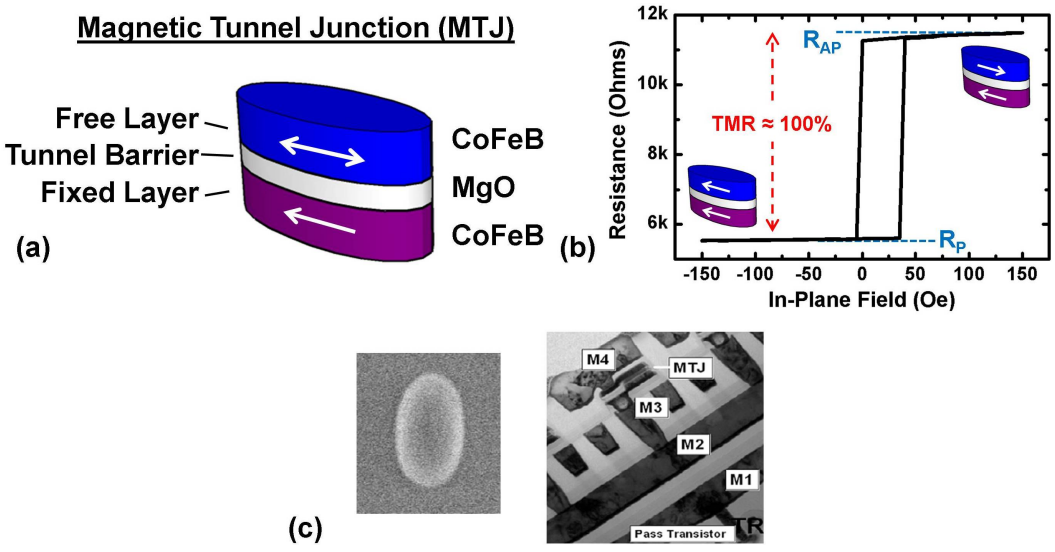

Fig. 1.4 (a) The "heart" of an MTJ device is composed by two ferromagnetic materials (free and fixed layers) separated by a tunneling barrier. The most common combination so far is the CoFeB|MgO|CoFeB stack. (b) The TMR effect serves as the read-out mechanism in MTJ devices. The resistance changes from a minimum (R_P) to a maximum value (R_{AP}) when the free layer goes from being parallel to antiparallel to the fixed layer. The figure shows a typical experimental R-H curve with a TMR ratio close to 100% for a 150 × 70 nm^2 MTJ device. (c) MTJ can be integrated to conventional semiconductor electronics as part of the BOEL processes, for example between metals 3 and 4 (M3 to M4) in the demonstration of Ref. [44].

The TMR effect can be explained, in a simple toy-model, as follows: In ferromagnets, the exchange interaction lifts the spin degeneracy in the band structure and thus the bands are split into spin-up and spin-down bands [9] (see Fig. 1.5(a)). If we consider a typical ferromagnetic metallic material such as Fe or Co, one of the conduction bands will have a lower energy (the majority band in Fig. 1.5(a)) and therefore the majority of the electrons will have their spins aligned into this preferred direction, translating into a total net spin polarization (magnetization) in the ferromagnetic material. In other words, the spin polarization of the majority band will be directly related to the magnetization state of the material.

The differences in the band structure for spin-up and spin-down electrons translate into different conduction and scattering rates, as well as different Fermi surfaces for each kind of electrons, making the transport heavily spin-dependent. Therefore, as a first-order approximation, we could think of the transport though a ferromagnetic material as being composed by two separate conduction channels, one for each kind of spins. In an MTJ device, the electrons travel from one ferromagnetic electrode to the other by tunneling through an oxide, where it is desired that the electrons do not lose their spin polarization during the tunneling process (i.e., very high quality, ultrathin oxides are required). We consider two transport scenarios for an MTJ: If the magnetizations of both ferromagnetic electrodes in the device are in the same direction, the transport process is decrypted in Fig. 1.5(b). In this scenario, a large number of electrons can tunnel to a large number of available states in one of the channels, resulting in a small resistance for this channel, and an overall small resistance since the transport will be dominated by the conduction through this path. Hence, the resistance of the MTJ will be small when the magnetizations are parallel to each other. In the second scenario, when the magnetizations are opposite (anti-parallel), there will be either few electrons in one channel, or few available states

to tunnel to in the other, and therefore the overall resistance will be high. This scenario is shown in Fig. 1.5(c). In conclusion, the dependence of the tunneling current on the relative magnetization directions of both free and fixed layers (ferromagnetic electrodes) is responsible for the TMR observed in MTJs, being the dominant mechanism aluminum oxide Al-O-based MTJs [9, 48].

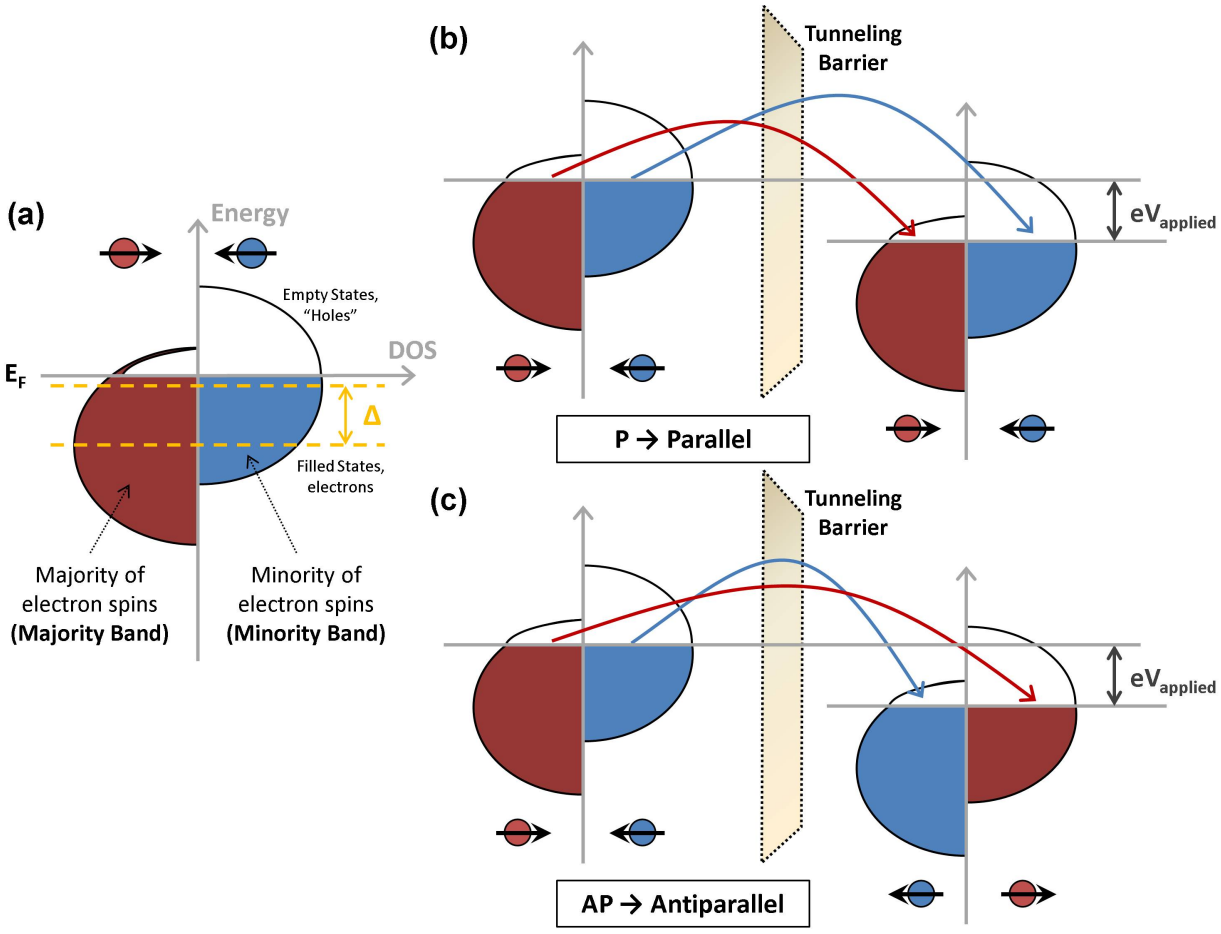

Fig. 1.5 (a) The strong exchange interaction in ferromagnets breaks the degeneracy between different spin states and results in a spin-dependent band structure. The shift in the energy bands (Δ) due to exchange produces a band where the majority of electrons lie, translating into a net magnetic momentum related to the spin polarity of the majority band [9]. Figures (b) and (c) decrypt the two channel model for the tunneling between two ferromagnetic electrodes with parallel and antiparallel magnetization, respectively. The resistance in the parallel state would be dominated by one channel (minority band), leading to an overall small resistance. The antiparallel state will have a higher resistance due to the small number of start/end states for both channels [48].

The TMR ratio in Al-O-based MTJs with Fe- or Co-based ferromagnetic electrodes progressively increased to ~70% by 2004 [49], time when the focus shifted to MTJs using (001) oriented MgO as tunneling barrier because of the major technological breakthrough independently reported by Parkin, *et al.,* [26] and Yuasa, *et al.,* [27] on the demonstration of a TMR ratio larger than 180% at room temperature. The larger TMR compared to amorphous Al-O barriers can be attributed to an additional spin filtering mechanism in crystalline MgO [50, 51], which can be explained as follows: In oriented 3d ferromagnets, electrons near the Fermi energy are characterized by Bloch states with different symmetries, depending on the orbital contribution to each band. The symmetries in Fe, for example, are Δ_1 (spd hybridization), Δ_2 (pd hybridization) and Δ_5 (d orbital). Electrons with Δ_1 symmetry are particularly important since first principles calculations indicate that they are highly spin polarized, with a polarization close to 100% [50]. When these Bloch states tunnel through an oxide, they couple with evanescent states in the oxide with the same symmetry, making the tunneling probability dependent on the symmetry of the states for the case of crystalline MgO. Fortunately, the symmetry with the highest tunneling probability (i.e., the slowest decay while tunneling) in (001) MgO is also the Δ_1 symmetry, and therefore, the MgO acts as an additional spin filtering, only favoring the tunneling of highly spin polarized states of the 3d ferromagnetic electrode, and rejecting other symmetries with low or negative spin polarization [49]. Notice that this is not the case for Al-O barriers, where the amorphous phase does not prefer any particular Bloch state and all the symmetries have the same tunneling probability, explaining the larger TMR observed in MgO versus Al-O barriers. Also it is important to note that the high spin polarization of the Δ_1 symmetry is predicted via first principle calculations for various 3d bcc ferromagnets such as Fe, Co, CoFe and CoFeB [49].

So far, the CoFeB|MgO|CoFeB "sandwich" in MTJs has developed into the equivalent to the $Si|SiO_2$ combination for the CMOS transistor community. This stack has become the most frequently used to build MTJ devices because of several practical advantages, including: (1) The stack can be fully sputter deposited, including depositions over large scale wafers. (2) The MTJ is composed by back-end of the line (BEOL) friendly materials, making it compatible with the fabrication of conventional semiconductor technology. Specifically, Fig. 1.4(c) shows that MTJs can be integrated to CMOS in the metallization stage by depositing and patterning the MTJs between metals 3 and 4 (M3 and M4) in the particular case of Ref. [44]. (3) The usage of amorphous (as deposited) CoFeB allows the MgO to grow (001) oriented on top of it. Then, when the devices are annealed, the boron diffuses out and allows the CoFe(B) to crystallize bcc (001) next to the already oriented MgO, with lattice constants very close to each other [49]. This results in TMR ratios for MTJ devices with in-plane magnetization as high as 604% at room temperature when the devices are annealed at temperatures above 500°C [52], or larger than 150-200% in more practical circumstances [53], taking into account the limited thermal budget of the BEOL processes in CMOS fabrication. Reference [53] presents a thorough summary of the TMR ratios obtained for different in-plane and perpendicular MTJ systems.

In summary, MTJs using CoFeB|MgO-based stacks offer the possibility to obtain a large read-out signal due to the TMR effect, even in CMOS-compatible conditions. There are currently multiple efforts in materials science, exploring alternative ferromagnetic materials (including half metals) or oxides different than MgO in order to increase the TMR effect beyond the CoFeB|MgO combination. However, this dissertation exploits the already established CoFeB|MgO|CoFeB combination for read-out and focuses on the critical issue of writing the information into this kind of MTJ devices. Before going into this topic, the next section will

describe how the information is stored in in-plane and perpendicular MTJ devices, making the MTJs a strong candidate as a non-volatile memory.

1.4 In-plane and perpendicular MTJ devices: Thermal stability and scalability

MTJ devices use the magnetization of the free layer as a state variable to store information, generate or detect RF power, sense magnetic fields, etc. For memory applications, as discussed previously, the information can be encoded in the relative alignment of the free layer with respect to the fixed layer. Due to the presence of different types of anisotropies in ferromagnetic systems [9] (i.e., the energy of the free layer is minimized along certain axis or axes for the magnetization), it is possible to engineer two or more thermally stable equilibrium conditions for the magnetization of the free layer, becoming those the memory states of the MTJ. The configuration of such equilibrium states and the degree of non-volatility of the MTJ, as defined by the thermal stability parameter defined later on in this section, are determined by the competition between the different anisotropies and any bias magnetic field sensed by the free layer. As for the configuration of the equilibrium states, in MTJ devices it is usually desired to have two free layer equilibrium states with orientations parallel and anti-parallel to the fixed layer respectively in order to maximize the resistance change due to the TMR effect when the device switches from one equilibrium state to the other. On the other hand, the degree of non-volatility is a critical parameter for the MTJ performance, where this parameter will greatly influence the sizing and scalability of the device as will be studied throughout this section. It is important to note that the exact amount of non-volatility required for the MTJ is a design parameter depending on the specific application (e.g., long-term storage versus working

memory), noting that there is typically a trade-off between the degree of non-volatility and the energy required to write the information into the MJT, the scalability, the sizing and the required materials specifications (e.g., strength of the anisotropies), hence explaining the importance of this critical parameter.

This section focuses on studying the thermal stability as a measure of the non-volatility of the MTJ devices, including the requirements on sizing, material specifications and the challenges for the scalability of MTJs for different applications. The discussion will focus on the two most frequent configurations for MTJs: In-plane and perpendicular devices (See Fig. 1.6). However, before discussing these two configurations, the concepts of demagnetization and the thermal stability factor Δ are defined.

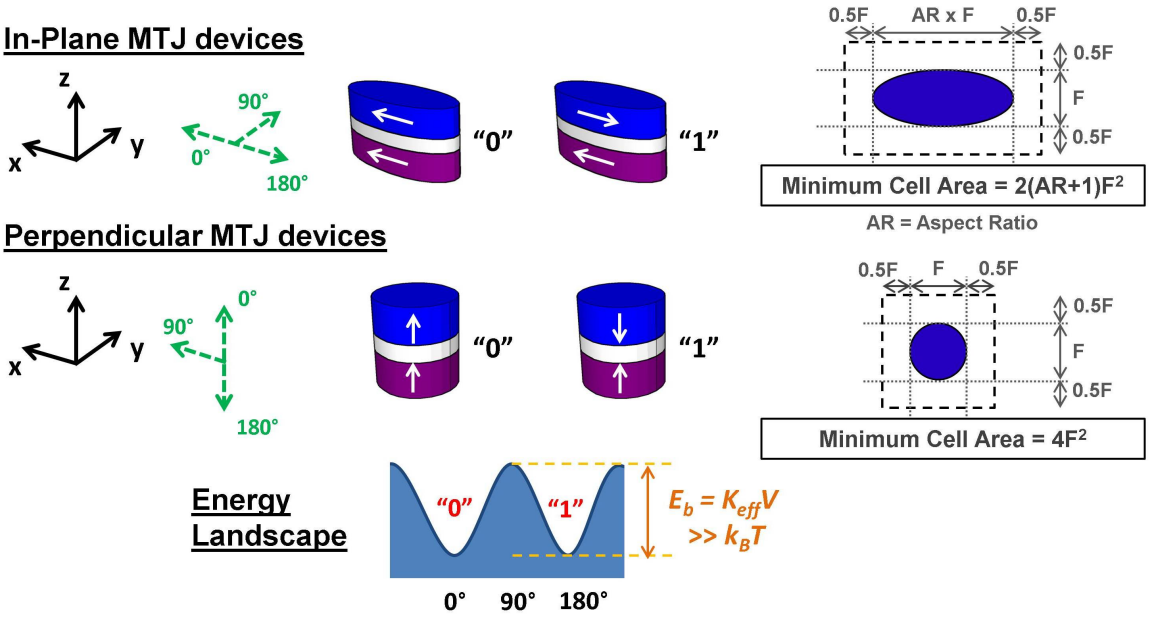

Fig. 1.6 The two most common configurations for the equilibruim conditions of the free layer when using the MTJs for memory applications are the in-plane and prependicular devices. In each case, the magnetization has two in-plane or perpendicular equilibrium states, separated by an energy barrier at the hard axis. In-plane MTJ devices exploit the ellipsoidal shape to create two equilibrium states, but also result in a larger area, which depends on the aspect ratio (AR) of the ellipse.

1.4.1 Demagnetization and the thermal stability factor (Δ)

Usually, the thickness of the free layer (set during the deposition of the MTJ stack) is smaller than the lateral dimensions of the MTJ, or in other words, the free layer is a thin-film ferromagnet. In the single-domain approximation, where all spins in the ferromagnetic material are aligned into the same direction to form an overall magnetization vector, thin-films tend to minimize the magnetic energy by favoring an in-plane magnetization configuration since it translates into a flux-closing path of least energy for the stray field, as illustrated in Fig. 1.7(a), where the stray fields for in-plane versus perpendicular magnetizations for the free layer are compared. The internal field that tends to favor a magnetization configuration that minimizes such energy is called the demagnetization field $\overrightarrow{H_d}$ [9] and can be directly calculated taking into account Maxwell equations, the geometry of the film and the constitutive parameters for the material. The average demagnetizing field acting on the free layer is typically written as [9, 54]

$$\overrightarrow{H_d} = -4\pi \overleftrightarrow{N} \cdot \overrightarrow{M} = -4\pi M_s \overrightarrow{N} \cdot \overrightarrow{m} \tag{1.2}$$

where $\overleftrightarrow{N}$ is the geometrical demagnetization tensor, $\overrightarrow{M}$ the magnetization vector, $\overrightarrow{m} = \overrightarrow{M} / M_s = (m_x, m_y, m_z)$ the unit vector in the direction of the magnetization and M_s the saturation magnetization. In simple geometries, as the ones typically used for the free layer in MTJ devices, it is found that a good approximation for the demagnetization tensor is obtained by only considering the diagonal components of the tensor, hence resulting in a reduced geometrical demagnetization vector given by $\overrightarrow{N} = (N_x, N_y, N_z)$ with $N_x + N_y + N_z = 1$. Fig. 1.7(a) compares also the demagnetization fields in a thin-film when the magnetization is in-plane versus perpendicular (out-of-plane), illustrating that the larger stray field of the perpendicular configuration translates into a larger equivalent demagnetization field, where the geometrical

demagnetization factor in the z-direction N_z is much larger than the ones in the in the plane of the film (N_x and N_y). Finally, the magnetic energy E_d due to demagnetization can be calculated as [9]

$$E_d = -\frac{1}{2}\int_V \overrightarrow{M} \cdot \overrightarrow{H_d}\, dV \tag{1.3}$$

thus, the demagnetization energy density, e.g., the demagnetization energy per unit volume, can be approximated to be $E_d / V = (1/2)4\pi M_s \overleftrightarrow{N} \cdot \overrightarrow{m} \cdot \overrightarrow{M} = 2\pi M_s^2 (N_x m_x^2 + N_y m_y^2 + N_z m_z^2)$ in the single-domain approximation, where the magnetization vector $\overrightarrow{M}$ is considered to be constant across the volume V , and the average demagnetization field $\overrightarrow{H_d}$ defined in equation (1.2) is considered. Consequently, it can be clearly observed that the large demagnetization field in the perpendicular direction tends to constrain the magnetization of the free layer into the plane of the thin-film, minimizing the demagnetization energy when the magnetization is in the in-plane direction.

Further, by patterning the MTJ into an ellipsoidal shape, an additional preference in the in-plane direction can be introduced. As observed in Fig. 1.7(b), the demagnetization field, or the equivalent amount of "magnetic charges", are minimized if the magnetization lies along the long axis of the ellipse, hence named as easy-axis for the free layer. If the magnetization is oriented along the short axis of the ellipse, the demagnetization field and energy are maximized, therefore creating a hard-axis for the magnetization. In Fig. 1.7, the equivalent demagnetization fields are presented for each configuration, where $N_z \gg N_y > N_x$ due to the geometry of the free layer. It should be noted that the ratio N_y / N_x can be enhanced by increasing the aspect ratio (AR) of the ellipsoidal shape.

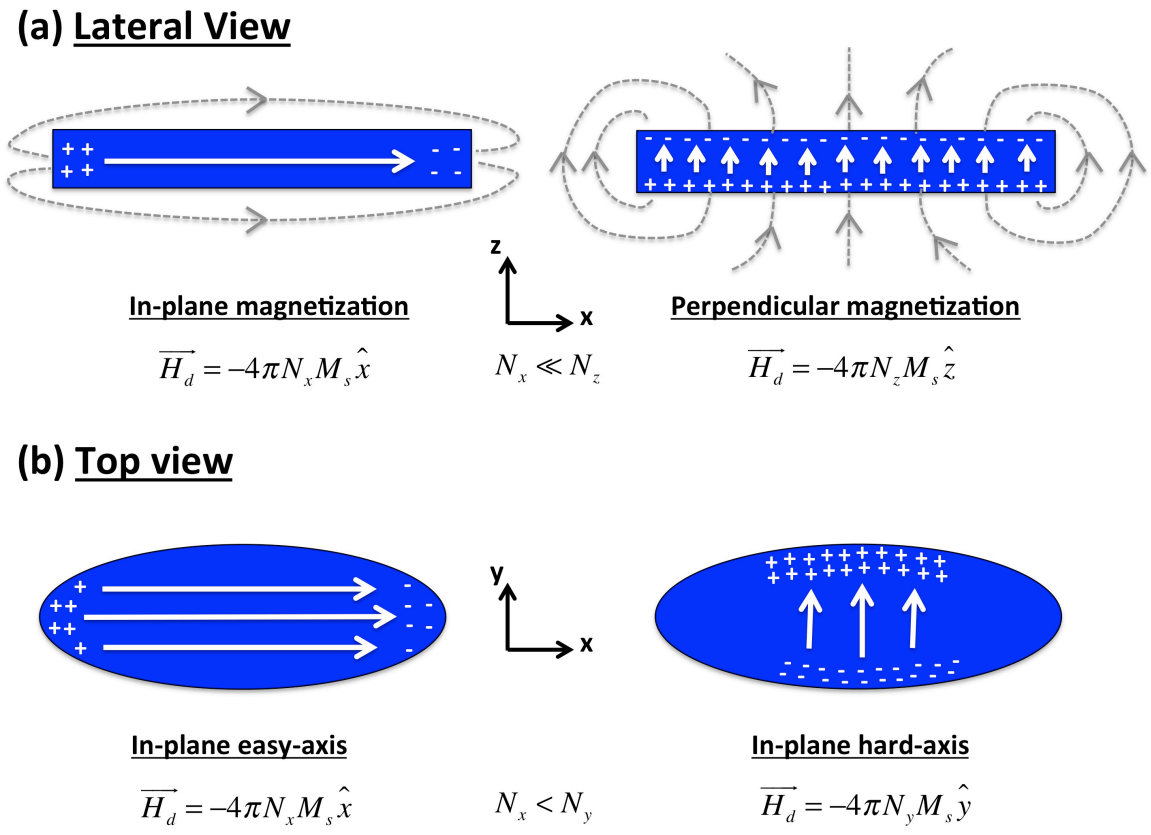

Fig. 1.7 (a) The lateral view of the free layer compares the stray fields for the cases where the magnetization is in the in-plane versus the perpendicular (out-of-plane) configuration. The in-plane configuration is preferred to minimize the demagnetization field $\overrightarrow{H_d}$. (b) The top view shows the free layer patterned as an ellipse, creating an easy-axis for the magnetization along the long axis of the ellipse (x-direction). The larger amount of "magnetic charges" when the magnetization is aligned along the y-direction results in a larger stray field, hence creating a hard-axis along such direction.

The preference for the magnetization to align along certain axis (the x-axis in the case of Fig. 1.7) because of the shape and geometry of the free layer is known as shape anisotropy [9]. The ellipsoidal shape for the thin-film free layer generates an easy-axis along the direction of the long axis of the ellipse, resulting in energy minimums, for example, in the +x and –x directions in Fig. 1.6 and Fig. 1.7. Then, if the fixed layer is pinned along the +x direction, the digital "0" for the memory could be defined as a parallel alignment of the layers (minimum resistance),

while the digital "1" would be related to the antiparallel alignment (maximum resistance). It is worth mentioning that the ellipsoidal shape is preferred in this configuration for several reasons, including avoiding corners that could create textures or pinning centers for the magnetization and also, because of patterning concerns, where smooth geometries (like an ellipse) are preferred. Notice also that only proper geometrical patterning of the ferromagnetic free layer is required in order to engineer the non-volatile magnetization states for the memory, explaining why the first generations of MTJ devices are based on the in-plane configuration.

As discussed in the introduction to the present section, a critical parameter for the performance of MTJs as a memory element is the degree of non-volatility of the free layer, measured by how thermally stable are the states that store the information. This can be quantified by the thermal stability factor Δ, which is related to the dwell-time of the state $<\tau>$, i.e., the average time it would take for the magnetization to escape the state and get randomized because of thermal fluctuation, hence, losing the information stored in the memory. These two quantities are related by the Néel-Arrhenius relaxation time equation (see p. 169 in Ref. [21])

$$<\tau>=\tau_0 \exp(\Delta) \tag{1.4}$$

where τ_0 is the attempt time and it is on the order of the inverse of the resonant frequency of the ferromagnetic layer ($\tau_0 \sim 1$ ns). At the same time, the thermal stability factor Δ can be related to the smallest energy barrier that the magnetization could escape from, in the presence of thermal fluctuations. Specifically, the thermal stability factor Δ is defined as

$$\Delta = \frac{E_b}{kT} \tag{1.5}$$

where E_b is the height of the energy barrier, k is the Boltzmann constant and T the temperature of operation of the device. Obviously, it is desired to have $E_b \gg kT$ in order to make the

memory states indeed non-volatile, however, making E_b too large compared to kT would imply that larger energies are required to write the information into the MTJ, and will also result in unnecessary additional requirements in terms of sizing and material specifications to allow for scalability, as will be shown below. Hence, Δ is engineered to be as small as possible, with a lower limit set by the specific application intended for the MTJ. Specifically, a thermal stability factor of $\Delta \approx 40$ would result in a dwell-time close to ten years for a given discrete device, enough to assure non-volatility of the memory for applications where long-term storage of the information is required. However, there are multiple applications where the requirement for the degree of non-volatility of the MTJ could be relaxed, depending on several design considerations such as how frequently the memory is written and the period of time where the design requires ensuring the non-volatility of the memory elements. For example, a thermal stability factor of $\Delta \approx 25$ is enough to assure a retention time on the order of 1 minute for a discrete MTJ device, allowing designing a non-volatile circuit for an application where such retention time is acceptable. However, here it is important to note two important considerations for the design of the thermal stability factor Δ: (1) Due to the dependence of Δ on temperature (see equation (1.5)), larger energy barriers are needed if the temperature range of operation for the circuit includes temperatures above room temperature. Therefore, the energy barrier E_b must be designed such that the non-volatility is assured across the temperature range of operation of the system. For example, if a given device has a $\Delta \approx 40$ at room temperature (300 K), the value of Δ at room temperature needs to be increased to $\Delta \approx 53.3$ in order to assure that, once the device operates at 125°C (400 K), the thermal stability factor will be 40 at such temperature. The latter assumes that the energy barrier E_b does not depend on temperature, which is typically not the case since both the magnetization saturation and the anisotropies tend to decrease with

temperature [55], in consequence resulting in a requirement to overestimate the value of Δ at room temperature for operation at temperatures above it. (2) The discussion above assumes a single device. However, if the non-volatility of an array of MTJs needs to be assured, an increase of the single device Δ is required in order to statistically assure that the whole array remains non-volatile. This obviously would depend on the number of MTJ devices, how the specific circuit that corrects for errors works, etc., however a detailed probabilistic study on the topic is out of the scope of this work.

1.4.2 In-Plane MTJ devices

As mentioned in the previous subsection, the first generations of MTJ devices are mostly based in the in-plane configuration; therefore, in this subsection the thermal stability and scalability of in-plane MTJ devices is analyzed, in the frame of the single-domain approximation. In the case of in-plane MTJ devices, the demagnetization field H_d that constrains the magnetization to the plane is very large (of the order of $H_d \sim 4\pi M_s$ from equation (1.2), with $N_z \gg N_x, N_y$), thus, the smallest energy barrier is related to an in-plane rotation of the magnetization. Fig. 1.6 shows the energy landscape for this trajectory, where the energy becomes maximum along the y-direction (hard-axis at 90° in Fig. 1.6) because of the shape anisotropy. Specifically, the height of the energy barrier is given by $E_b = K_{eff} V$, where K_{eff} is the effective anisotropy energy, i.e., the subtraction of the shape anisotropy energies along the hard- and easy-axis, and V is the volume of the free layer. Taking into account that K_{eff} can be written in terms of the effective anisotropy field $H_{k,eff}$ as $K_{eff} = M_s H_{k,eff} / 2$ (see equation (1.3) for the relation between magnetic energies and equivalent fields), the thermal stability for an in-plane MTJ device can be approximated to be

$$\Delta = \frac{K_{eff}V}{kT} = \frac{M_s H_{k,eff} V}{2kT} = \frac{4\pi(N_y - N_x)M_s^2 At}{2kT} \tag{1.6}$$

where the effective anisotropy field $H_{k,eff} = 4\pi(N_y - N_x)M_s$ corresponds to the subtraction of the demagnetization fields along the y- and x-direction (see Fig. 1.7), A is the area and t the thickness of the free layer. Subsequently, the thermal stability is set by the saturation magnetization M_s, the area A, the thickness t of the free layer, and by the difference of the demagnetization factors $N_y - N_x$, where this geometrical quantity is directly related to the aspect ratio (AR) of the ellipse. In consequence, depending on the desired value for the thermal stability of the MTJ, the design parameters for the free layer are mostly its volume and the aspect ratio of the ellipse, given that the saturation magnetization regularly does not change much in between the different ferromagnetic materials that show a large TMR ratio up to now.

In-plane MTJ devices possess advantages such as having larger TMR ratios and lower damping factors [53, 56, 57]. However, using an ellipsoidal shape results in a minimum cell area of $2(AR+1)F^2$, where F is the minimum feature size for the technology node. Taking into account that the area of a minimum size transistor is on the order of $6\text{-}8F^2$, the sizing and aspect ratio of the MTJ would be desired to be such that there is no penalty in terms of memory density when adding the MTJ device to the circuit. Further, for situations where high density for the memory is needed, a more compact circular shape (minimum area of $4F^2$, see Fig. 1.6) is preferred, motivating the need perpendicular MTJ devices.

In terms of scalability, as the area is reduced, the aspect ratio of the in-plane device would have to be incremented in order to retain the thermal stability, or the thickness of the free layer would have to be increased to keep the volume constant [58]. The first approach is practical only up to certain values of AR, not only because of the penalty in minimum cell area size as AR

increases, but also because of the difficulties in patterning high aspect ratio memory bits. As for the second approach, it has limitations for very small technology nodes, where the required thickness would become comparable or larger than the lateral dimensions of the MTJ, making the thermal stability dominated by other energy barriers different to an in-plane rotation of the magnetization. Also, experimental studies in scaled devices at this new regime where the thickness of the free layer is comparable to its lateral dimensions are required to validate such scaling approach and neglect the possible emergence of other micromagnetic or structural effects. Finally, it is worth noting that, in principle, it would be possible to thermally stabilize in-plane MTJs by having a large in-plane uniaxial anisotropy in the material of the free layer. However, up to now, there have not been experimental reports in the literature of such strong anisotropy in materials with even a moderate TMR ratio.

1.4.3 Perpendicular MTJ devices

An alternative approach is making the fixed and free layers perpendicular to the plane of the thin-films, resulting in the perpendicular MTJ device shown in Fig. 1.6. In order to overcome the large demagnetization field previously discussed, a large uniaxial anisotropy energy (K_u , in units of energy per unit volume) in the perpendicular (z-direction in Fig. 1.6) is required. Such anisotropy may be the result of a preference for the spins to align in the perpendicular direction due to magnetocrystalline or interfacial effects [9, 21], different from the origin based on geometry for the thermal stability in in-plane devices.

In particular, the demagnetization energy for a perpendicular MTJ device can be estimated from Fig. 1.7(a) as the difference between the energies in the perpendicular and in-plane directions, in other words (see section 3.2 of Ref. [54])

$$K_d = \frac{M_s H_d}{2} = \frac{M_s \cdot 4\pi (N_z - N_{x,y}) M_s}{2} \approx 2\pi M_s^2 \tag{1.7}$$

where N_z is the demagnetization factor in the z-direction, $N_{x,y} = N_x = N_y$ assuming a circular shape for the MTJ and, if the free layer is much thinner than the lateral dimensions of the MTJ, we can approximate $N_z \approx 1$ and $N_{x,y} \approx 0$. Hence, in order to make a layer perpendicular, the condition $K_u > 2\pi M_s^2$ must be met, setting a requirement for the strength of the uniaxial anisotropy energy required to obtain a perpendicular MTJ device.

One of the advantages of the perpendicular configuration is that the thermal stability is no longer dominated by the shape of the MTJ, but rather by the uniaxial anisotropy. In this case, considering the single-domain approximation once again, the trajectory that determines the thermal stability is related to the magnetization travelling between the +z to the –z direction via the in-plane state (maximum energy at 90° in the in-plane direction, which becomes the hard-axis as illustrated in Fig. 1.6). The effective anisotropy field in this configuration will be given by $H_{k,eff}^{\perp} \approx H_{k\perp} - 4\pi M_s$, where $H_{k\perp} = 2K_u / M_s$ is the effective field due to the uniaxial perpendicular anisotropy, which favors the perpendicular direction, and $H_d \sim 4\pi M_s$ is the demagnetization field that tends to make the magnetization in-plane. Thus, the thermal stability for a perpendicular MTJ can be approximated to

$$\Delta = \frac{M_s H_{k,eff}^{\perp} V}{2kT} \approx \frac{M_s \left(\frac{2K_u}{M_s} - 4\pi M_s \right) V}{2kT} = \frac{(K_u - 2\pi M_s^2) At}{kT} = \frac{K_{eff} At}{kT} \tag{1.8}$$

where we have defined the effective perpendicular anisotropy energy as $K_{eff} = K_u - 2\pi M_s^2$. It is clear that, in order to maintain the thermal stability as the device is scaled down, the product $K_{eff} \times t$ must increase in the same proportion as the area A is reduced.

Several material systems with large bulk perpendicular anisotropies are currently being explored, including $L1_0$ ordered materials (e.g., FePd and FePt), rare-earth alloys and Co/(Pt,Pd) superlattices [59]. These materials show a large K_u, which can be, for example, as high as $K_u \sim 7\times10^7$ erg/cm^3 for FePt [60]. Further, they have a positive scalability trend since both the thickness or K_u can be separately increased in order to achieve the thermal stability required for the MTJ. However, they still have several challenges to overcome before becoming an option to construct MTJs for memory applications, including high damping, no or low TMR and high thermal budgets, not compatible with BEOL processing.

Finally, an interesting alternative approach was demonstrated by Ikeda, *et. al.* [61], reporting on the large interfacial perpendicular anisotropy in Fe-rich CoFeB, allowing to construct perpendicular MTJ devices with a TMR ratio larger than 100%. In this case, the surface uniaxial anisotropy energy can be written as $K_u = S_i / t$ due to the interfacial nature of the anisotropy, where S_i is the interfacial anisotropy energy (in units of erg/cm^2), and for the case of Ta|Fe-rich CoFeB|MgO, it has a value on the order of 1 erg/cm^2 [61]. Therefore, by tuning the thickness, the condition $S_i / t > 2\pi M_s^2$ can be met in order to obtain a perpendicular MTJ device. Also, by modifying equation (1.8) to account for an interfacial anisotropy, the thermal stability becomes

$$\Delta = \frac{\left(\frac{S_i}{t} - 2\pi M_s^2\right)At}{kT} = \frac{(S_i - 2\pi M_s^2 t)A}{kT} \tag{1.9}$$

Thus, the desired thermal stability for the perpendicular MTJ can be achieved by either tuning the interfacial anisotropy or by decreasing the thickness of the material. From equation (1.9) it is clear that the second approach has a weaker effect due to the $2\pi M_s^2 t$ becoming smaller to

subtract from S_i in the factor $S_i - 2\pi M_s^2 t$, while the area A appears with a multiplication effect. Further, there are additional concerns and practical challenges for reducing the thickness of the free layer such as lower TMR, higher damping and reduced reliability. Therefore, increasing the interfacial anisotropy S_i is required to achieve small technology nodes, the latter becoming especially important to obtain MTJ devices with sizes comparable to current and future CMOS transistor feature sizes. Section 2.4 will present a scaling analysis on the required values for S_i as a function of the different technology nodes.

Lastly, given that no shape anisotropy is required in order to assure the thermal stability of the device, MTJs can be patterned in circles, reaching the smallest possible cell area for a 2-terminal device without considering possible 3D stacking: $4F^2$ (see Fig. 1.6). Another advantage of using perpendicular MTJ devices is that the coupling between devices in a dense array is reduced by going from the in-plane to the perpendicular configuration [62]. But more importantly, for the case of the interface anisotropy, the fact that such perpendicular anisotropy can be modulated by electric fields in the MgO layer is the basis for the electric-field-controlled scheme that will be exploited in this work. As discussed in the previous section, writing efficiently the information in MTJs is a major bottleneck for current MTJ technology, and electric-field control of the anisotropy is one of the possible approaches to address such issue. Starting from Chapter 2, this phenomenon will be discussed in detail, whereas the rest of this chapter will present the conventional writing mechanisms currently being used for MTJs.

1.5 Magnetoresistive Random Access Memory (MRAM)

The usage of MTJ devices next to CMOS technology allows constructing a memory architecture where each individual bit can be randomly accessed with reading and writing times

on the order of tens-hundreds of nanoseconds at most, features that are not possible in other magnetic memory technologies such as hard-disks (HDDs) or magnetic tapes. The resulting architecture, named Magnetoresistive Random Access Memory (MRAM), has become an attractive emerging technology due to its advantages as a fast, fairly low-power, high-endurance, radiation-resistant non-volatile memory that can be easily integrated to conventional semiconductor processing [7]. The concept behind MRAM was initially proposed in 1960s [63], but its development was only possible after the discovery of the magnetoresistive effects (GMR and mainly, TMR) to read-out the information. In terms of writing, different mechanisms have been proposed and studied, going from magnetic fields to spin-polarized currents (STT effect) and recently, to magnetoelectric effects (i.e., electric fields, the topic of this dissertation), resulting in several families of MRAM: Oersted-field-switched (toggle) MRAM, STT-MRAM, and MeRAM, the proposed memory technology in this work.

The first generations of MRAM utilized the Oersted fields generated by running currents in adjacent conducting lines to the memory cells in order to switch the magnetization via field-induced reversal. Fig. 1.8 illustrates the typical memory cell for the first generations of MRAM, where each cell includes an MTJ device, an access (isolation) transistor, and conducting wires for creating the magnetic fields needed to switch the device. In order to read the information, the access transistor is activated, allowing the flow of a sensing current I_{Sense} that will used later to decode the information into the MTJ. For writing the bit, the currents I_{Easy} (Write word line) and I_{Hard} (Bit line) would flow perpendicularly selecting a single bit in the array, where I_{Hard} generates a magnetic field that reduces the energy barrier between the two memory states, while the magnetic field generated by I_{Easy} completes the reversal process, and determines the switching direction depending on the sign of I_{Easy}.

Albeit its advantages, the first generations of MRAM were not very successful (only limited to small niche markets) because of scalability and density problems: First, the need for complex wiring to create the magnetic fields to write the information limit the cell size to minimum 20-30 F^2 [35]. Second, the current needed to write the bit is high (in the mA range) and this problem becomes even larger as the device is scaled since the switching current is inversely proportional to the volume of the cell [48, 56]. Finally, as the cells are closer to each other, stray fields can switch adjacent bits.

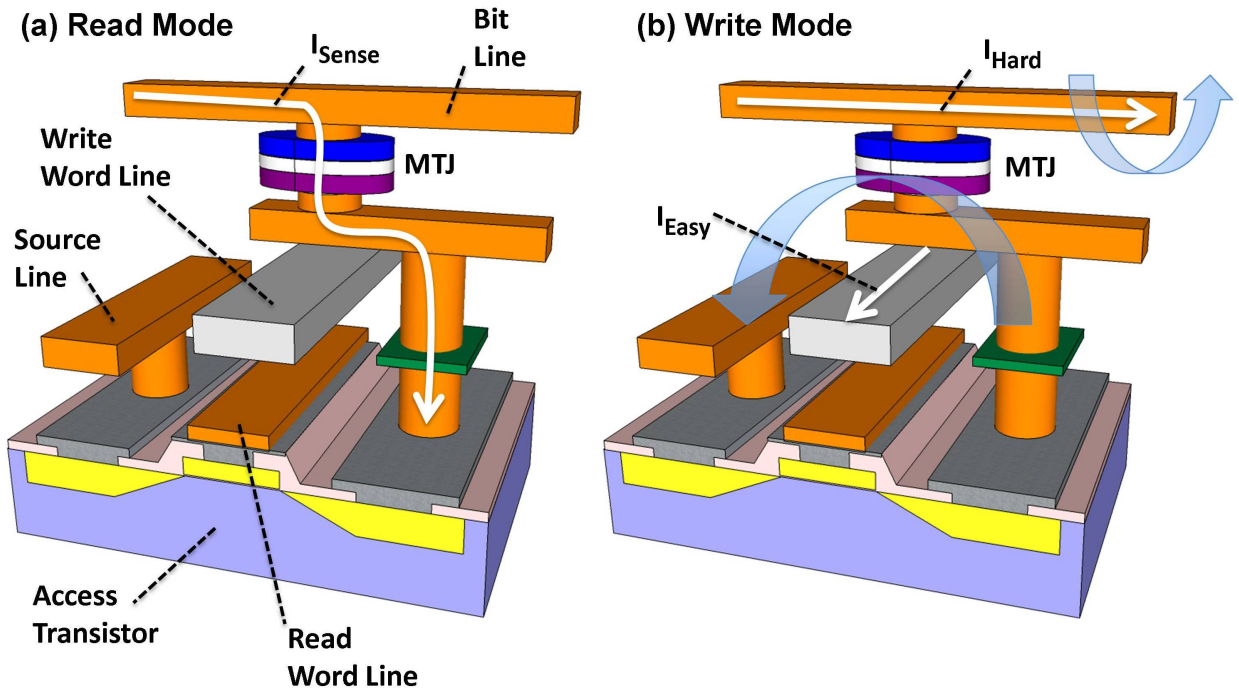

Fig. 1.8 The typical Oersted-field-switched MRAM cell includes an MTJ device, an access (isolation) transistor and wiring for reading and writing the bit. (a) To read-out the information, the access transistor allows a small sensing current to be used to decode the resistance (i.e., the state) of the MTJ. (b) Magnetic fields in the easy and hard axis of the MTJ are generated by currents in the write word line and bit line respectively. These fields are used to switch the magnetization of the MTJ device.

In conclusion, most of the limitations of the first MRAM prototypes were related to the field-driven writing mechanism. Therefore, the manipulation of magnetic moments by currents

or electric voltages is required to overcome the shortcomings of Oersted-field- switched MRAM. The emergence of the STT effect (current-driven writing mechanism) has spurred the interest in MRAM in the last years, paving the way for the development of this technology. The advantages of STT, and the challenges that motivate the usage of magnoelectric effects beyond STT are discussed in the next section.

1.6 Spin transfer torque (STT) as a switching mechanism

The discovery of the possibility to manipulate and induce switching of the magnetization by spin-polarized currents via the spin transfer torque (STT) effect [32, 33] in nanomagnets has been the key motivating force behind the recent rise of interest in MRAM, and particularly STT-MRAM [35, 64, 65]. STT-MRAM conserves the advantages of Oersted-field-switched (toggle) MRAM (high speed, very high endurance, non-volatility), but the current-driven switching mechanism makes STT-MRAM more scalable and allows for smaller switching energies (on the order of ~100 fJ/switch) compared to Oersted-field-switched MRAM (> 10 pJ/switch).

In STT-MRAM, the writing process is performed by passing a spin-polarized current, which transfers some of its momentum to the free layer, inducing a torque that can result in switching of the MTJ. The direction of the reversal process (i.e., P to AP or AP to P) depends on the direction of the current flow, thus different current polarities are used to switch the MTJ in between opposite states [48]. Given that the writing process can be performed using the same wiring as the one use for reading the MTJ device, the MRAM memory cell can be simplified to the structure shown in Fig. 1.9, illustrating a typical 1T-1R (One transistor, one MTJ resistor) STT-MRAM configuration. The elimination of the additional lines required to generate magnetic fields to write the information results in an increase of the density, allowing a minimum cell size

of 6-8 F^2 in STT-MRAM, i.e., the area of a minimum size transistor, but could be lowered to $4F^2$ using vertical transistors [35, 56, 57]. However, the real cell size will be mostly determined by the sizing of the access transistor, which cannot be of minimum size in order to allow enough drive current to write the MTJ cell [66], where the large write currents (on the order of ~100 μA) are regularly a limiting factor in STT-MRAM.

In this section we will briefly consider three different designs for STT-MRAM devices (referred to as I-STT, C-STT and P-STT standing for In-plane, Combined, and Perpendicular), which offer different characteristics and performances due to their configuration of magnetization direction and anisotropies of the free and fixed layers.

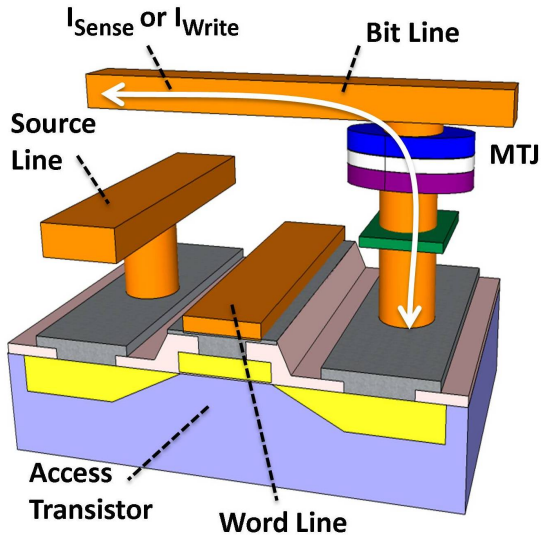

Fig. 1.9 Typical architecture for a 1 transistor – 1 MTJ (1T-1R) memory cell in STT-MRAM. The absence of a write word line allows for a more compact design, with minimum cell densities down to 6-$8F^2$ (when using a minimum size access transistor). In this configuration, writing of the information is achieved by passing a larger current through the same terminals as the sensing (read) operation, while the direction of the write current will determine the final state of the MTJ.

1.6.1 In-Plane free layers

Two of the device configurations where the magnetization of the free layer lies in the plane of the thin-film (in-plane configuration) are shown on Fig. 1.10(a) and (b). In the I-STT

(In-plane STT) configuration, the polarizer (pinned layer) is in the same plane of the free layer, while the C-STT (Combination-STT) structure includes an additional polarizer for reasons to be discussed later in this section.

One of the key challenges for STT-MRAM is to reduce the switching current density J_{c0}, or more importantly, the switching current I_{c0}, while keeping the target for the thermal stability factor Δ depending on the application intended for the memory. In particular, for the I-STT configuration, the switching current density is given by (the detailed derivation can be found in Ref. [67])

$$J_{c0} = \frac{I_{c0}}{A} = \frac{2e\alpha M_s t}{\hbar\eta}\left(H_{k,eff} + \frac{H_d}{2} \right) \tag{1.10}$$

where α is the free layer damping factor, A is the area, η is the spin-transfer efficiency, M_s and t are the free layer saturation magnetization and thickness, $H_{k,eff}$ is the in-plane shape-induced anisotropy field and $H_d \gg H_{k,eff}$ is the demagnetization field in the z-direction, as defined in section 1.4. The derivation of equation (1.10) assumes that the spin-polarized electrons transfer their angular momentum $\hbar/2$ with efficiency η, causing a torque on the magnetization. The torque is introduced into the Landau–Lifshitz–Gilbert (LLG) equation that describes magnetization dynamics (see section 2.6) and the critical current I_{c0} is defined as when the torque is large enough to destabilize the magnetization from its equilibrium.

By comparing equations (1.6) and (1.10), it is clear that I-STT devices generally require a trade-off between the switching current density J_{c0} and the thermal stability factor Δ. In particular, it can be observed that the switching current is dominated by the out-of-plane demagnetizing field H_d, which typically does not determine the thermal stability, given that $H_{k,eff} \ll H_d$ (see discussion in section 1.4.2), explaining in part why large switching currents are

typically needed to switch MTJ devices. Hence, the goal for optimization is to minimize the figure of merit I_{c0}/Δ, while preserving a given target for the thermal stability factor.

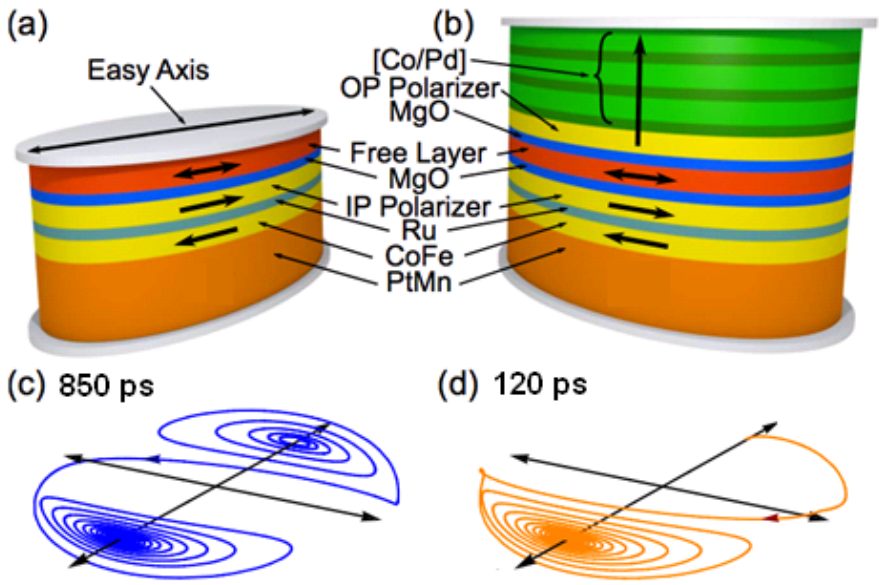

Fig. 1.10 (a) The layered structure for I-STT device, including a synthetic antiferromagnetic (SAF) to compensate for the dipole fields from the pinned layer acting on the fixed layer. (b) The inclusion of an additional perpendicular polarizer results in a C-STT configuration, where the added polarizer results in a spin polarization that creates a large initial torque for the free layer switching. (c) Macrospin simulations showing the intrinsic limitation of I-STT due to the incubation time required for a switching event. (d) The perpendicular polarizer in C-STT results in precessional switching, hence eliminating the initial incubation, and allowing for switching with pulses of the order of 100 ps [68].

On the other hand, I-STT suffers from a small spin torque during the initial incubation stage of magnetization switching, a consequence of its parallel-magnetized equilibrium states, resulting in switching speeds on the order of ~ 1 ns [68, 69]. An alternative to eliminate the initial incubation of I-STT devices is to include an additional out-of-plane polarizer (see Fig. 1.10(b)), resulting in the C-STT configuration, also referred to as orthogonal STT-RAM [68-70]. C-STT uses a combination of in-plane and perpendicular polarizers, where the in-plane polarizer provides TMR for readout of the in-plane free layer state, while the spin torque from the

perpendicular polarizer causes the free layer magnetization to go out-of-plane, where it precesses around the large demagnetizing field in the z-direction, allowing for ultrafast precessional switching limited only by the ferromagnetic resonance (FMR) frequency of the bit [69]. As observed in the macrospin simulations of Fig. 1.10(c) and (d), the torque provided by the out-of-plane polarizer eliminates the initial incubation resulting in precessional switching on the order of ~ 100 ps. In fact, switching with pulses down to 130 ps in MTJs [68, 71], and down to 50 ps in spin-valves [72] has been demonstrated experimentally. C-STT usually requires larger switching currents compared to I-STT, however, if we take into account that the write energy is given by $E = I_c^2 Rt$, the reduction of the required pulse time t outpaces the potential increase in the required switching current I_c for C-STT, resulting in a reduction of the switching energy larger than 50% as compared to an I-STT device with an otherwise similar layered structure [68, 71].

As mentioned previously, one of the key challenges in STT-MRAM is to reduce the large write currents/energies required, where the typical switching energies are at least two orders of magnitude larger compared to CMOS (~ 100 fJ versus ~ 1 fJ/switch respectively). To reduce the write energy in STT-MRAM, one could perform optimization on both the free layer as well as the MgO tunneling barrier. If the switching energy is written as $E = I_c^2 Rt = J_c^2 A^2 Rt$, it is evident that the energy can be further decreased in I-STT devices by (1) reducing the resistance R of the MTJ, or by (2) decreasing the switching current density. The first strategy is limited by practical reasons, since reducing the resistance of the MTJ requires thinner MgO barriers, which may result in reduction of the TMR ratio, endurance or breakdown voltage, increase of the damping of the free layer, as well as in undesired device-to-device variability [36, 73]. Furthermore, scaling of STT-MRAM generally requires moving to thinner MgO barriers, i.e., reducing the resistance-area (RA) product is needed to prevent the resistance of the device to increase when

scaling the area in order to keep the required switching current with the same voltage levels. Consequently, the MgO thickness is generally set by considerations other than energy.

Another strategy to decrease the switching energy requires the reduction of the switching current. For I-STT devices, by dividing equation (1.10) into equation (1.6) and, the switching current to thermal stability figure of merit is given by

$$\frac{I_{c0}}{\Delta} = \frac{4e\alpha kT}{\hbar\eta}\left(1+\frac{H_d}{2H_{k,eff}}\right) \tag{1.11}$$

where $H_d \gg H_{k,eff}$ in I-STT devices, as discussed above. Notice that I_{c0}/Δ of I-STT decreases (desired trend) within the scaling trend derived in section 1.4.2 for Δ in in-plane devices, given that an increase of the free layer thickness will reduce the demagnetization field H_d, while $H_{k,eff}$ will remain approximately constant to keep the value of Δ as the device is scaled. This positive scaling trend remains valid up to the point where $H_{k,eff}$ and H_d become comparable, hence making the in-plane configuration thermally unstable and equation (1.11) invalid. As mentioned previously, the study and experiment demonstration of the scaling of in-plane MTJs to very small sizes (<30 nm) is still pending in order to validate the predicted positive scaling trend as the thickness of the free layer is increased, including the reduction of I_{c0}/Δ when the area is decreased.

Another promising method to decrease the switching current without sacrificing the thermal stability is to decrease the demagnetizing field H_d by the introduction of perpendicular anisotropy in the free layer [56, 74, 75]. In particular, by exploiting the significant interface-induced perpendicular anisotropy in Fe-rich CoFeB|MgO junction discussed in section 1.4.3, a perpendicular anisotropy field $H_{k\perp}$ can be introduced in order to cancel the demagnetizing field, such that the switching current over thermal stability ratio can become much smaller, specifically

$$\frac{I_{c0}}{\Delta} = \frac{4e\alpha kT}{\hbar\eta}\left(1 + \frac{H_d - H_{k\perp}}{2H_{k,eff}}\right) \tag{1.12}$$

This concept has been demonstrated experimentally as reported in the literature [74, 75]. For example, the work by Khalili Amiri*, et al.,* demonstrated a reduction of the average quasi-static switching current density by >40% (from ~2.8 MA/cm^2 to ~1.6 MA/cm^2) due to the presence of the perpendicular anisotropy [75]. However, the figure of merit cannot be reduced beyond the constant $4e\alpha kT/\hbar\eta$, which corresponds to the case of a perpendicular MTJ device ($H_{k\perp} \sim H_d$).

1.6.2 Perpendicular free layers

If the perpendicular anisotropy of the free and fixed layers are large enough to overcome their respective demagnetizing fields (i.e., $H_{k\perp} > H_d$), the magnetizations of the layers become perpendicular, giving rise to a fully-perpendicular (P-STT) configuration (see section 1.4.3). In the P-STT configuration, the demagnetizing field is fully cancelled and therefore, different to in-plane devices, the barrier that determines the thermal stability is the same as the one that STT effect has to overcome to induce a magnetization reversal (within the single-domain approximation). In the latter scenario, the switching current density is given by

$$J_{c0} = \frac{I_{c0}}{A} = \frac{2e\alpha M_s H_{k,eff}^{\perp} t}{\hbar\eta} \tag{1.13}$$

By dividing equation (1.13) into equation (1.8) the switching current over thermal stability (I_{c0}/Δ) figure of merit is calculated to be

$$\frac{I_{c0}}{\Delta} = \frac{4e\alpha kT}{\hbar\eta} \tag{1.14}$$

It can be noticed that the elimination of the demagnetizing field leads to a potentially smaller I_{c0}/Δ for P-STT compared to I-STT devices. In fact, several works have recently

demonstrated P-STT structures utilizing the interfacial perpendicular anisotropy of Fe-rich CoFeB layers in MgO MTJs [61, 76, 77], with switching currents < 2 MA/cm^2 [76]. However, larger damping α and lower spin-transfer efficiency η are typically observed in perpendicular free layers so far, so even though P-STT has a theoretically smaller I_{c0}/Δ, I-STT devices may reach smaller currents at scaled nodes because of the better material parameters and a predicted positive scaling trend [78]. From equation (1.14) it is clear that, in principle, perpendicular MTJ devices, independent of their size, will require an approximately constant switching current I_{c0} once the target for Δ is established based on the requirements for the MTJs depending on the application. This presents a fundamental problem for the scaling trend of perpendicular MTJ devices, as the transistors needed to drive this constant switching current will not significantly shrink with successive technology nodes [79, 80], hence limiting the possibility to scale the transistors to drive the MTJs and hence, making the cell area of the memory constrained by the area the transistors instead of the MTJ memory element. However, a recent work by Sato *et al*., [81] experimentally studying the scaling of I_{c0} and Δ on perpendicular devices down to 11 nm shows that, even though the scaling trend predicted in section 1.4.3 is accurately followed for Δ, the figure of merit I_{c0}/Δ is experimentally observed to decrease as the device shrinks (desired trend), which is initially attributed to the reduction of the effective damping in equation (1.14) during the switching process for smaller devices.

Albeit the obvious advantages of STT-MRAM versus Oersted-field- switched MRAM, the large switching currents in the former translate into challenges in terms of dissipated energy and density (i.e., large transistors are required to drive the write current, making the memory cell area dominated by the access transistor footprint, see discussion on section 2.5). Multiple research groups in industry and academia are currently trying to lower the switching currents

well below 0.1-1 MA/cm^2, critical to reduce the switching energy, increase the density and allow to scale to very small technology nodes, by improving the damping of the free layers and the spin transfer efficiency (e.g., by using half-metals or materials with higher spin polarization). Also, it is worth mentioning that there are alternative approaches being explored to reduce the switching current in STT-MRAM bits such as bias-assisted [82] and thermally-assisted switching [83, 84], both of these in research stages. Finally, other writing mechanisms different to STT are being explored, being the spin Hall effect (SHE, current-controlled) one of the options, as discussed in the following section, while this work will concentrate in magnetoelectric (i.e., electric-field controlled) effects starting on the next chapter.

1.7 Spin Hall effect (SHE)

Although one of the pioneer experimental report on the spin Hall effect (SHE) can be traced back to the work of Kato, *et al.*, in 2004 [85], SHE, or more general, spin-orbit torques (SOTs) where SHE is one of them, have been considered an alternative to replace STT as a switching mechanism only after the demonstration by Liu, *et al.*, in 2012 [37] on the possibility to switch an MTJ device by a charge current flowing in an adjacent metallic layer with large spin-orbit coupling (SOC) such as Ta. The current flowing in the high-SOC material generates a spin current through the MTJ (via the so-called giant spin Hall effect), which is large enough to induce switching in the device. The device structure is shown in Fig. 1.11, where the electrical current J_c flowing between terminals A and C induces a spin current $J_s = \theta_{SH} J_c$ through the MTJ device, being θ_{SH} referred to as the spin Hall angle. The polarization of the spin current is in the direction of the cross product between J_c and J_s, i.e., the spin current has an in-plane polarization [37]. However, the direction of the current J_c controls the direction of the in-plane

polarization of J_s and therefore, the switching direction will be determined by the sign of J_c. By using the β-phase of Ta, the spin Hall angle θ_{SH} can be as large as ~12% without further increase of the damping of the adjacent CoFeB free layer [37]. However, it has also been demonstrated that the spin Hall angle can be as large as 30% in tungsten [86], comparable to the spin-current-efficiency for regular two terminal MTJ devices ($\eta \sim 60\%$).

The usage of SHE, or spin-orbit torques in general, to switch MTJ devices addresses some specific challenges of STT-MRAM: First, the current density required to switch the MTJ can be tuned by engineering the dimensions of the metal (e.g. Ta) wire, without disturbing the thermal stability of the MTJ. In particular, the ratio of the switching current due to spin Hall (I_{SH}) to the required current for STT (I_{STT}) can be approximated by

$$\frac{I_{SH}}{I_{STT}} \approx \frac{\eta}{\theta_{SH}} \frac{A_{SOC}}{A_{MTJ}} \tag{1.15}$$

where A_{SOC} and A_{MTJ} are the cross-sectional area of the underlying high-SOC metal layer, and the MTJ device respectively (see Fig. 1.11). Thus, considering that the area of the metal layer (interconnect) A_{SOC} could be engineered to be as much as one order of magnitude smaller as compared to A_{MTJ} by reducing the thickness of the metal < 5 nm, the switching current can be lowered by nearly one order of magnitude compared to STT-based switching. Second, the read (terminal B to A or C in Fig. 1.11) and write paths (A to C) would be separated, allowing disturb-free read operations. At the same time, this allows to optimize the MTJ for conditions that increase TMR, reduce the damping of the free layer, etc., without affecting the write process. Also, the reliability of the device should be enhanced since the large writing current will flow through the high-SOC metal, while a smaller current through the MTJ could be used for the read operation. Third, the switching from P to AP and, from AP to P becomes symmetric, which is

not possible in STT-MRAM due to the asymmetry for the MTJ when the write current flows from free to fixed layer and vice versa. Finally, in terms of switching energy, the smaller switching current would flow through a lower resistance metallic wire (e.g. ~ 0.3 ohm-um^2 for a L = 200 nm Ta wire as compared to an MTJ), leading to switching energy levels around one order of magnitude lower than STT (~ 10 fJ/switch).

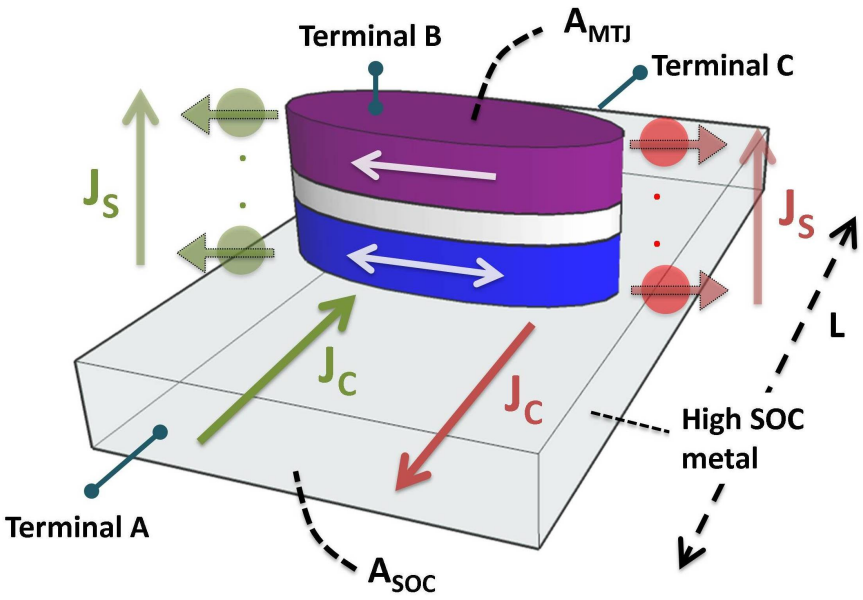

Fig. 1.11 Three terminal device configuration exploiting the giant spin Hall effect in a high spin-orbit coupling (SOC) metal adjacent to an MTJ device. By running a current J_C through the high SOC wire (between terminals A and C), a pure spin current J_S through the MTJ is induced, which can be used for switching the free layer. The spin polarization of the spin current J_S will depend on the direction of J_C. One of the advantages of this three terminal configuration is that the required current can be tuned by engineering the lateral area of the wire A_{SOC}, meanwhile A_{MTJ} can be designed to account for a given thermal stability factor. By symmetry considerations, this three-terminal structure cannot be used alone to generate controllable switching of perpendicular magnets, but recent works [87, 88] have proposed symmetry breaking strategies to overcome this issue.

However, spin Hall has additional challenges and issues: First, the device goes from two terminals to three terminals, translating into penalties in terms of memory density and

complexity to fabricate the device. Second, replacing STT by SHE only provides a one-time gain in terms of the reduction of the switching current; however, the SHE configuration has the same scaling concerns discussed in the previous section for STT. In fact, a constant-current scaling rule for SHE would require reducing A_{SOC} by the same amount as A_{MTJ}, resulting in ultrathin high-SOC films with larger resistance (therefore, larger switching energies), but also, that could have continuity and high resistivity issues.

As discussed in the previous sections, perpendicular MTJ devices are of high interest due to their smaller size and potential scalability over in-plane MTJs (see sections 1.4.3 and 1.6.2); hence, it would be greatly desired to use SHE, or spin-orbit torques, as a writing mechanism in perpendicular devices. A recent work by Yu, Upadhyaya, *et al.*, [87] provides a detailed symmetry analysis for the three-terminal structure in Fig. 1.11, showing that an in-plane current flowing through the high SOC metal does not have any preference for "up" or "down" perpendicular states, hence SHE or spin-orbit torques alone cannot create controllable switching for a perpendicular free layer in this three-terminal configuration. In order to solve this issue, Yu, Upadhyaya, *et al.*, propose a structural symmetry breaking by introducing a wedged oxide in the lateral direction of the MTJ. This symmetry breaking is experimentally shown to result in controllable switching of perpendicular magnets by hypothetically introducing a field-like torque in perpendicular direction. It should be noted that the microscopic picture of this demonstration is still missing; therefore, modeling on the critical switching current and the scalability of this approach is still an open research question up to the moment. An alternative approach is to replace the structural symmetry breaking by an applied bias magnetic field in the in-plane direction that breaks the required symmetry [88]. The in-plane field tilts the magnetization of the perpendicular magnets, allowing controllable switching. In this situation, the scalability will still

be described in principle by the analysis in section 1.6.2, taking into account the reduction on the switching current due to SHE and the reduction of the thermal stability due to the applied bias field. However, a detailed analysis and experimental study on the scalability of this approach is also still missing up to now in the literature.

The field of spin Hall, or in general spin-orbit torques (also called spin orbitronics [89]), is currently a very active area of research, therefore significant breakthroughs like the recent report on a spin Hall angle three orders of magnitude larger in topological insulators operating at 1.9 K [38] could translate into a future highly energy-efficient SOT-MRAM architecture. An alternative to the still current-controlled spin-orbit torques is the utilization of electric-field-driven mechanisms, with the potential to further reduce the energies required to manipulate magnetic systems. This is one of the motivations to exploit magnetoelectric effects to control and switch MTJ devices.

CHAPTER 2:Voltage-Controlled Magnetic Anisotropy (VCMA)

2.1 Motivation

Nanomagnetic systems may be easily engineered to become non-volatile (i.e., having zero stand-by power dissipation), thus becoming a great alternative to classical volatile electronic devices. However, the dynamic power needed to manipulate magnetic systems is typically much higher compared to the one required in electronic devices. Therefore, finding a mechanism that reduces the dynamic power dissipation of these magnetic systems, especially MTJs, to levels comparable or even lower than CMOS may lead to a major paradigm change in the field of electronic and spintronics devices for logic and memory. In particular, making the energy efficiency of MTJ devices comparable to CMOS may allow constructing hybrid instant-on CMOS-MTJ circuits for non-volatile logic [12], where the memory elements could be switched as frequently as the transistors, task which is not currently possible due to the large power dissipation needed for manipulating the MTJs, hence resulting in a intolerable increase on the dissipated power in order to make the system non-volatile. Further, a highly efficient write mechanisms for MTJs may pave the way for an improved memory architecture over STT-MRAM, well suited for both embedded and stand-alone applications.

As discussed in the previous chapter, albeit the remarkable series of discoveries over the past decade in current-controlled mechanisms to manipulate magnetic systems, and in particular MTJ devices, the dynamic energy dissipation by using the STT or SHE effects still remains at least 1-2 orders of magnitude larger compared to CMOS. One of the reasons behind the energy-efficiency of the CMOS technology is the usage of electric fields to control the gate of the transistor. Translating the success of CMOS in electronics to the world of magnetism would

require developing efficient and practical schemes to manipulate magnetic phenomena via voltages or electric fields, also termed as magnetoelectric (ME) effects. The use of electric fields allows for much lower power dissipation since in principle no charge flow is required for such voltage-controlled devices to operate, hence reducing or even eliminating Ohmic losses and Joule heating. In fact, electric field control of magnetism could replace STT and SHE in a similar transition to the one experienced in electronics when BJTs (current-controlled) were mostly replaced by CMOS (electric-field-controlled) mainly because of power concerns.

Recent works by Nikonov, *et al.*, [90-92] provide a thoughtful benchmarking effort of emerging devices versus scaled CMOS, where nanomagnetic systems are considered one of the strongest alternatives for beyond CMOS computation. In particular, Fig. 2.1 shows an energy-delay chart comparing STT, SHE and ME effects versus scaled high-performance (HP) and low-power (LP) CMOS. The dynamic energy E_w of the different spintronics approaches presented in Fig. 2.1 (in red) is calculated as

$$E_w = CV_c^2 + \left(V_c^2 / R\right)t_w \tag{2.1}$$

where $V_c = I_c R$ is the voltage required to switch the device (dynamic energy), R the resistance and t_w is the switching time (delay). On the other hand, the energy-delay number of HP and LP transistor were obtained from experimental measurements over scaled Intel transistors [90-92].

As discussed previously in section 1.6.2 and later in section 2.4 and throughout Chapter 5, switching of spintronics device in the thermally activated regime is limited to times t_w (delay) larger than the attempt time τ_0 defined previously in equation (1.4), where the attempt time τ_0 is on the order 1 ns. On the other hand, precessional switching is only limited by ferromagnetic resonance and can achieve switching times t_w < 100 ps, but usually results in a penalty in terms

of V_c required (see sections 1.6.2 and 2.4). In terms of dissipated energy, the energies required for STT and SHE reported in Fig. 2.1 are mostly due to Ohmic losses (second term in equation (2.1)), where the switching current $I_c = V_c / R$ decreases when going from I-STT to P-STT and finally to SHE, as mentioned before in sections 1.6 and 1.7.

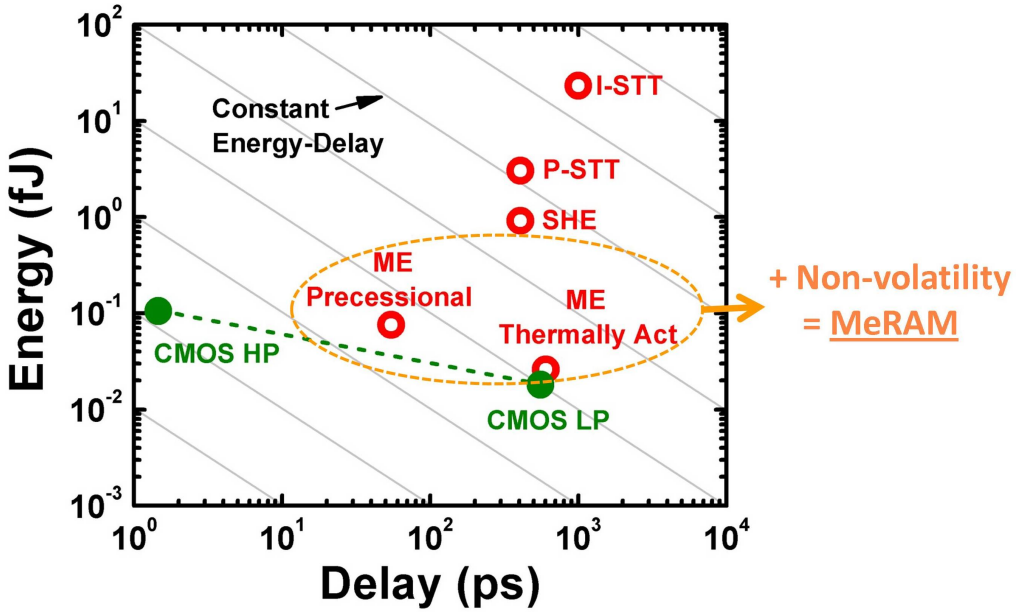

Fig. 2.1 Energy-delay chart comparing the current- and electric-field-based switching mechanisms for MTJs (in red) versus high-performance (HP) and low-power (LP) CMOS (in green), assuming conditions for scaled technology nodes (< 14 nm) to CMOS and using equation (2.1) to calculate the energy for spintronics approaches [91, 92]. Due to Joule losses, the current-controlled mechanisms STT and SHE are still 1-2 orders of magnitude less energy efficient compared to CMOS. Only the usage of magnetoelectric (ME) effects, either in the thermally activated or precessional regime, may allow to reach the energy effiiency of CMOS. The calculation only takes into account dynamic energy dissipation, however the non-volatile magnetic systems also lead to zero stand-by (static) dissipation. The combination of a low dynamic power and zero static dissipation may lead to novel magnetoelectric memory architecture such as MeRAM (Modified from Refs. [91, 92]).

It can be clearly observed that only by using ME effects, it is possible to reach energy levels on the line between HP and LP CMOS. ME effects eliminate the need for the flow of charge currents in order to achieve switching, hence removing the contribution to the energy

coming from the second term in equation (2.1), which dominates the losses in STT and SHE. Consequently, the dynamic energy is only limited by the capacitive (first) term in equation (2.1) in both CMOS and ME in MTJs. Notice that the capacitances of CMOS versus MTJs, as well as the voltages required to switch the two devices have comparable values, therefore resulting in similar energy values as reported in Fig. 2.1.

In terms of delay, current MTJ technology can well compete against LP CMOS, however in order to reach the short delay times of HP CMOS, using antiferromagnetic/ferrimagnetic systems may be required. These kinds of materials are out of the scope of this work, but there is no fundamental reason why electric field control of such systems may be developed in the future.

In this chapter, the possibility of controlling magnetic phenomena via electric fields will be discussed, focusing on the modulation of the perpendicular anisotropy in MTJ devices via the voltage-controlled magnetic anisotropy (VCMA) effect as an electric-field-driven mechanism. Further, the prospect of a new magnetoelectric RAM (MeRAM) architecture with improved energy efficiency and scalability compared to STT-MRAM or SOT-MRAM will be presented.

2.2 Coupling mechanisms for electric field control of magnetism

Controlling magnetic phenomena via electric fields is currently an intense area of research in spintronics, looking to develop efficient mechanisms to translate electric fields into effective magnetic fields that can be exploited to manipulate magnetic materials and devices. Coupling magnetic phenomena to electric fields is not an easy task, especially in the metallic ferromagnetic materials like Fe and Co (e.g., those also showing the largest TMR ratios so far), where electric fields will be mostly bound to the surfaces. Multiple approaches are currently

being explored, each one of them with promising features but also specific challenges that need to be addresses via further research.

The quest for magnetoelectric (ME) effects to manipulate magnetic materials can be traced back to the 1950s and 1960s, with the pioneering works on multiferroic materials [93]. In multiferroic systems, at least two ferric properties simultaneously exist, being each one coupled to the other. For example, by having ferroelectricity and ferromagnetism in the same system, an electric field can alter the ferroelectric properties, and due to the coupling between the ferric properties, the ferromagnetic properties will be control by the applied electric field in consequence [94, 95].

Multiferroic materials can be divided into two categories: single-phase and composite multiferroic. There are currently only a few thin-film single-phase multiferroic materials that can operate near or above room temperature (e.g., $YMnO_3$, $LaMnO_3$, $BiMnO_3$, $BiFeO_3$), hence, considerable effort is being invested in finding novel materials which exhibit this fascinating property [93, 96]. Interestingly, a recent work by Heron, *et al.*, [97] demonstrated the possibility to obtain electric-field-induced 180° rotation of the magnetization, becoming an interesting proof of concept of the potential of single phase multiferroics as a vehicle towards efficient electric field control of magnetism. However, existing single-phase materials are exotic, thus they are difficult to grow and manufacture in processes friendly to conventional semiconductor fabrication, limiting their applicability for electronic devices as of now.

In composite multiferroics, two or more ferric materials are coupled to form the multiferroic system [95, 96, 98]. This is an attractive alterative to the single-phase option, given that well established ferromagnetic/ferroelectric materials can be used, opening the range of combinations to construct the multiferroic system. Even though two different materials are used,

a strong coupling between the ferric phases can be obtained; for example, when using the strain from a piezoelectric material in response to the application an electric field, the strain can be transmitted to an adjacent ferromagnetic material, and if the latter has magnetostrictive properties, the strain will change the magnetic anisotropy of the ferromagnetic phase [99].

A composite multiferroic can be formed, for example, by patterning an MTJ device on top of a thin-film piezoelectric material, such as Lead zirconate titanate (PZT) or lead magnesium niobate-lead titanate (PMN-PT) [100]. The piezoelectric will be actuated by electric fields, straining the free layer and modifying its the magnetic anisotropy. On the other hand, a typical TMR structure would be used to read-out the information. The device concept is illustrated Fig. 2.2(a), meanwhile Fig. 2.2(b) shows a proof of concept demonstrating the effect of strain over the magnetic anisotropy of a nanoscale MTJ device. The experimental curves in Fig. 2.2(b) show measurements of the resistance of the MTJ versus magnetic field for a 150 × 70 nm^2 MTJ device without any strain, and in the presence of 500 μstrains (500 ppm), i.e., simulating the effect of a compressive strain due to the application of an electric field into a piezoelectric (see Fig. 2.2(a)). The curves clearly show that strain effect is able to almost close the coercivity of the free layer, hence, reconfiguring the magnetic easy axis of the free layer. This principle has been also demonstrated by Wu, *et al.*, [99] in Ni films grown over PMN-PT substrates. In the cited work, it is shown that 500 μstrains can be obtained by applying electric fields smaller than 1 MV/m = 1 mV/nm in the piezoelectric substrate, hence, magnetic reorientation and switching could be obtained in composite multiferroics with voltages in the mV range once the piezoelectrics are scaled to nm thin films. Albeit the impressive efficiency of the energy transfer from the electric field into the magnetic anisotropy via strain, the integration of piezoelectrics to CMOS technology is not straightforward due to the complexity of the materials,

and also, it is currently unknown what would be the behavior of such thin-films composite multiferroic in terms of endurance, fatigue, leakage, clamping and even the strength itself of the piezoelectric coefficients once the films are scaled to the nanometer scale.

Other approaches for electric field control of magnetism are: (1) modulation of the carrier-mediated ferromagnetism in dilute magnetic semiconductors via gate voltages [31, 101]. In this approach, typical semiconductor materials such as Ge are doped with magnetic impurities, and therefore the fabrication is, in principle, friendly to CMOS processing. There are currently multiple efforts to increase the Curie temperature of such systems, while the main concern is the very small signal to noise ratio obtained from the diluted magnetic material, even in controlled experiments; (2) control of the ferromagnetic phase transition (i.e., Curie temperature) by electric fields [102, 103]. This mechanism is of significant interest since magnetism could be in principle turned on and off in ultrathin metallic ferromagnets with the application of electric fields. As of now, the effect is rather small in experiments (change of ~12 K in the Curie temperature in Ref. [103]), and therefore, it requires films with Curie temperatures very close to room temperature, which is impractical for devices operating across a wide temperature range; (3) electric field control of the ferromagnetic/antiferromagnetic transition [104, 105]. For this mechanism, strain or temperatures are used to induce small displacements of the atoms in the crystal structure, leading to a phase transition between ferromagnetic and antiferromagnetic phases. In the first demonstrations, FeRh was the material used, however, further research may lead more materials showing this effect.

It should be noted that most of these mechanisms are in early research stages, and critical demonstrations such as reliable read-out of the information and manufacturing in practical

conditions are still required these options before plausible and effective options for electric field control in nanomagnetic devices that can compete against current semiconductor technology.

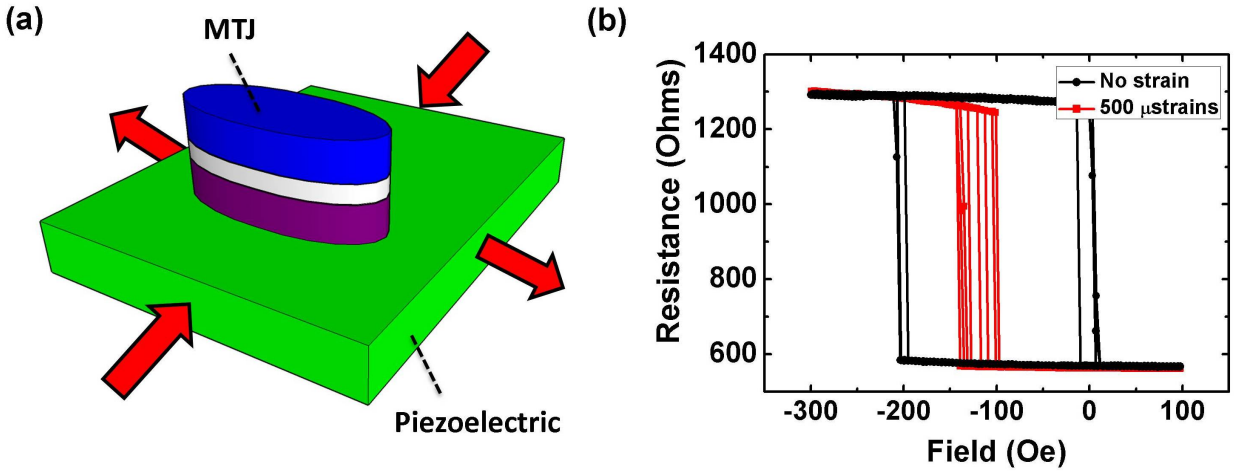

Fig. 2.2 (a) Device concept of a composite multiferroic, including an MJT device for read-out. In the figure, the piezoelectric creates a compressive strain that is transmitted to the magnostrictive free layer. (b) Experimental curves on a nanoscale 150 × 70 nm^2 MTJ device showing that a small strain can almost completely close the coercivity, leading to a reconfiguration of the magnetic easy axis of the MTJ (Data pending to be published).

Finally, a particularly promising approach relies on the electric field control of the interfacial magnetic anisotropy in ultrathin magnetic films. The practical promise of this voltage-controlled magnetic anisotropy (VCMA) effect relies in part on the fact that it can be realized in materials very similar to those used in regular MTJs, such as those utilized in STT devices. Hence, VCMA devices can benefit from the significant existing body of knowledge on materials and manufacturing of MRAM devices. While only a subset of the entire body of research on electric field control of magnetism, recent developments on VCMA-driven MTJs point to the possibility of using these devices in practical MRAM chips for memory and logic applications, and therefore VCMA will be mechanism used throughout this work.

2.3 Voltage-controlled magnetic anisotropy (VCMA) in ultrathin films

The most common ferromagnetic materials are metallic; hence, any external electric field would only penetrate a few Angstroms into the material, where such distance is named the Thomas-Fermi screening length. The concentration of the electric field near the surface is a limitation for electric field control of the magnetic properties of these materials. However, by making the ferromagnetic films ultrathin, the material becomes more sensitive to any phenomena that couples the applied electric field to the magnetic properties of the material via interfacial mechanisms. Thus, manipulating metallic ferromagnets via interfacial effects is one of the possibilities for electric-field control of magnetism in ultrathin films.

In the previous section, the possibility of controlling the Curie temperature in ultrathin films via electric fields in the interfaces was introduced. However, not only the Curie temperature, but also other magnetic properties can be tuned via interfacial effects. One particularly interesting parameter is the magnetic anisotropy, a critical quantity that can be related to the thermal stability and the switching threshold for a magnetic device (see for example the discussions in sections 1.4 and 1.6 for MTJ devices, and later in this section). The so-called voltage-controlled magnetic anisotropy, or VCMA effect, allows controlling the interfacial anisotropy of ultrathin ferromagnet|oxide stacks by applying electric fields through the oxide. This effect has been subject to considerable attention in the last years, including multiple experimental and theoretical studies [40-43, 106-111]. Also, the VCMA effect is of practical interest, as mentioned at the end of the last section, and allows inducing electric-field-driven switching of the magnetization in MTJ devices [112-115]. Hence, this work concentrates on studying and exploiting the VCMA effect in nanoscale magnetic tunnel junctions.

One of the pioneer theoretical works predicting the existence of the VCMA effect can be attributed to Duan, *et al.*, in 2006 [40]. In their prediction, they considered an Fe|$BaTiO_3$ composite multiferroic sandwich. By running *ab-initio* calculations, they observed that electric fields in the $BaTiO_3$ dielectric modulate the magnetic moment of the interfacial Fe atoms via orbital modification, e.g., changes in the bonding at the Fe|$BaTiO_3$ interface (see section 2.3.1 for a more detailed discussion). The effect was carefully studied to be fundamentally different from magnetostriction (i.e., any strain-induced effect from the $BaTiO_3$ was eliminated), opening a new route for electric field control of magnetism. Further, Rondinelli, *et al.,* in 2008 [116] enriched the theoretical foundation behind the VCMA effect by expanding it to any interface between a dielectric and a spin-polarized metal, interpreting their first principle calculations in terms of a first-order magnetic response of the system to an applied electric field.

Regarding experiments, in 2008, Weisheit, *et al.*, [41] performed the first demonstration of the VCMA effect by observing a maximum 4.5% change in the coercivity of FePt and FePd thin-films, which are submerged into an electrolyte solution allowing for charges to accumulate at the surface of the films upon application of an electric field. An important breakthrough on the field was then reported by Maruyama, *et al.*, in 2009 [42] on the first observation of a sizable VCMA effect in an all-solid-state system. One of the key points of this demonstration was the usage of an Fe|MgO sandwich, one of the most relevant material combinations in spintronics due to its large TMR ratio (see discussion in section 1.3). The work by Maruyama, *et al.,* was the precursor for exploiting the VCMA effect in MTJ devices.

During the last years, the VCMA effect has attracted considerable attention of the community, with multiple reports on the characterization of the effect in different material systems utilizing magneto-optical Kerr [42, 106], anomalous Hall [107] or ferromagnetic

resonance (FMR) [108-110] techniques, actively looking for materials that could increase the strength of the VCMA. In terms of exploring the effect in devices, our group has been one of the pioneers in the investigation of the VCMA in CoFeB|MgO-based nanoscale MTJ devices, being one of the first groups to demonstrate electric-field-induced switching of MTJ devices [112, 113] along with the reports by Wang, *et al.*, [114] and Shiota, *et al.*, [115].

To illustrate the influence of the VCMA effect over nanoscale MTJ devices, Fig. 2.3 shows experimental measurements of resistance versus out-of-plane magnetic field in a perpendicular 80 × 80 nm^2 device. The utilized material stack is discussed later in detail on section 5.5. When no voltage (electric-field) is applied, the device shows a square loop, indicating that the free layer has a stable perpendicular configuration at equilibrium. If the MgO is thick enough (~ 1.2 nm) to make the MTJ act more as a capacitor, the application of a voltage will result in an electric field through the MgO oxide and, in the accumulation of charges near the interface between the MgO and the CoFeB free layer. The presence of an electric field/charge accumulation translates into changes in the magnetic anisotropy depending on the polarity of the applied voltage. Specifically, negative voltages are observed to increase the coercivity of the free layer in the perpendicular direction for this particular material stack, i.e., the perpendicular magnetic anisotropy is increased at V = −1 V in Fig. 2.3. On the other hand, by applying a positive voltage of V = +1 V, the measured curve shows hard-axis-like behavior, indicating the perpendicular anisotropy is decreased and the new minimum energy condition for the free layer is in the in-plane direction. The principle of reconfiguring the magnetic easy axis of the free layer via the VCMA effect is critical to allow for switching of the free layer using electric fields, and will be discussed in detail in Chapter 5 where multiple switching schemes are studied.

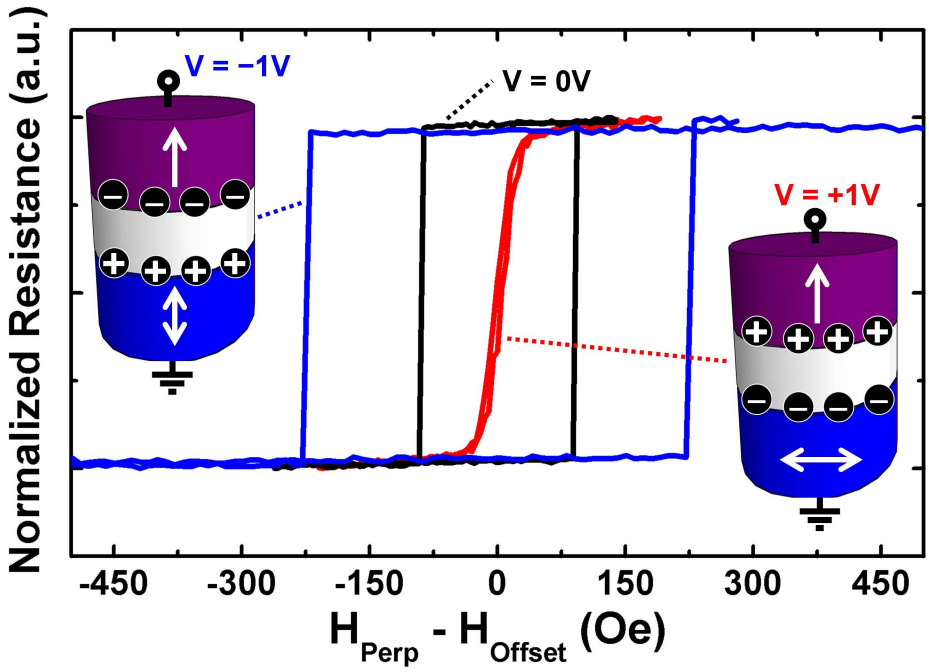

Fig. 2.3 Measurements of the normalized resistance versus the perpendicular (out-of-plane) field after subtraction of the offset field, in a CoFeB|MgO|CoFeB 80 × 80 nm^2 MTJ device. The exact material stack of the MTJ is discussed in detail later on section 5.5. Also, the resistance is normalized in between different voltages in order to compensate for the dependence of the MTJ resistance and TMR effect on the applied voltage. Notice that the MTJ has an equilibrium perpendicular configuration, as indicated by the square loop a V = 0V (black). The application of a negative voltage (blue) further increases the coercivity, representing an increase of the perpendicular anisotropy. However, a positive voltage results in a hard-axis curve, showing that the reduction of the perpendicular anisotropy due to the VCMA effect can reconfigure the magnetic easy axis to the in-plane direction (Data pending to be published).

At present, the detailed physics behind the mechanisms that allows for VCMA effect is still an active research area. The first theoretical works proposed an orbital-based explanation that was widely accepted in the community. However, a work by Barnes, *et al.*, in 2014 [43] provides an alternative explanation based on the Rashba effect at the interface, providing a model for experiments that could not be explained in the frame of the orbital-based theory. It is likely that both mechanisms actually contribute to the VCMA effect; therefore, the next subsections will try to briefly touch on the differences between these two mechanisms. At the

end of the section, a macrospin description where the effect is lumped as an effective change of the magnetic anisotropy is presented. This description is independent of the exact mechanism that drives the VCMA effect and allows parameterizing the strength of the effect via the so-called VCMA coefficient or magnetoelectric coefficient.

2.3.1 Orbital contribution

Starting from the first theoretical prediction by Duan, *et al.*, in 2006 and, until the recent work by Barnes, *et al.*, in 2014, the VCMA effect was explained solely in terms of the changes in the orbitals of the atoms near the interface between the ferromagnetic material and the oxide due to the applied electric field. The connection of orbitals to magnetic anisotropy is due to the spin-orbit coupling (SOC), where such interaction has a Hamiltonian of the form $H_{SOC} = \vartheta(\vec{r})\vec{S}\cdot\vec{L}$, being $\vec{S}$ and $\vec{L}$ the spin and orbital angular momentums, and $\vartheta(\vec{r})$ the spin-interaction parameter, which is proportional to the radial derivative of the atomic potential. The spin-orbit interaction is responsible for introducing a net orbital momentum, which otherwise would not exist in a highly symmetric crystal where the *d* orbital hybridize and result in zero orbital momentum. In the presence of SOC, the magnetic orbital momentum is given by [21]

$$\vec{m}_{orb} = \mu_B \sum_{i,j} \frac{\langle \phi_i | \vec{L} | \phi_j \rangle \langle \phi_i | H_{SOC} | \phi_j \rangle}{E_i - E_j} \tag{2.2}$$

where ϕ_i is the wavefunction corresponding to an occupied orbital, ϕ_j to an unoccupied orbital, E_i is the energy associated to the occupied state (below Fermi energy E_F) and E_j to the unoccupied state (above E_F). The larger contribution to the orbital momentum will come from the coupling between unoccupied and occupied orbitals very close to the E_F (i.e., having a small $E_i - E_j$), and therefore they are very sensitive to any change in the electron population or the

orbital configuration itself. Further, the uniaxial anisotropy energy can be approximated in terms of the orbital momentums using Bruno's formula [21]

$$\Delta E_{ani} \approx \frac{\vartheta}{4\mu_B}\left(m_{orb}^{\perp} - m_{orb}^{\parallel}\right) \tag{2.3}$$

where $m_{orb}^{\perp}$ and $m_{orb}^{\parallel}$ are the orbital magnetic moments in perpendicular and in-plane direction respectively and $\vartheta = \left|\vartheta(\vec{r})\right|$ is the magnitude of the spin-interaction parameter, which quantifies the strength of the SOC Hamiltonian, as mentioned before. Consequently, the mechanism for VCMA could be crudely explained as follows: The electric field (or charge accumulation) near the ferromagnet|oxide interface can modulate the orbitals of the atoms present in there. Such modulation can increase or decrease the orbital magnetic moments in different directions, depending on the interaction of the electric-field-controlled orbitals with the components of the angular momentum operator $\vec{L} = (L_x, L_y, L_z)$. Hence, the orbital magnetic moments $m_{orb}^{\perp}$ and $m_{orb}^{\parallel}$ will become electric-field-dependent as well, where the interaction of some orbitals with components of $\vec{L}$ will promote a perpendicular anisotropy (increasing $m_{orb}^{\perp}$), while others will have a negative contribution to the perpendicular anisotropy (increasing $m_{orb}^{\parallel}$). The net strength and sign of the VCMA effect will be therefore given by the difference between the electric field dependencies of $m_{orb}^{\perp}$ and $m_{orb}^{\parallel}$.

Calculating the contribution to VCMA because of orbitals is a complicated task that requires first-principle calculations in order to obtain the different orbitals in the material and their interactions. Obviously, the calculation becomes very sensitive to the atoms in the material, their bonding properties and band structure. A good example is the work by Ong, *et al.*, [117] in an FePd-based study, identifying the different contributions from orbitals with different

symmetries, in particular, the positive contribution to perpendicular anisotropy coming from $\langle xz|L_z|yz\rangle$ and $\langle x^2-y^2|L_z|xy\rangle$ matrix elements, and the negative contributions from the interactions $\langle z^2|L_x|yz\rangle$, $\langle xy|L_x|xz\rangle$, $\langle x^2-y^2|L_x|yz\rangle$, $\langle z^2|L_y|xz\rangle$, $\langle xy|L_y|yz\rangle$ and $\langle x^2-y^2|L_y|xz\rangle$.

In the first theoretical work by Duan, *et al.*, it was observed via first principle calculations that the charge accumulation near the Fe|$BaTiO_3$ interface was able to promote or repress the hybridization between the transition metal elements with less than half occupied *d* band (Ti) and more than half of the occupied *d* band (Fe), depending on the sign of the polarization in the $BaTiO_3$. The change in the hybridization of the Fe atoms near the interface (i.e., changes in the atomic bonding due to orbital modification) translated into a change of the magnetic anisotropy by the mechanism previously exposed.

A particularly interesting system for this work is the Fe|MgO interface. As previously discussed on section 1.4.3, a very large interfacial perpendicular anisotropy has been observed in such system, where first principles calculations have attributed it to hybridized Fe 3*d* orbitals with O 2*p* orbitals from the MgO [118]. For this system, the accumulation of charges at the interface induces a change in the occupation between orbitals that promote or repress the perpendicular anisotropy. In particular, as illustrated on Fig. 2.4(a), the accumulated charges at the interface due to the applied electric field change the occupancy between $d_{3z^2-r^2}$ orbitals (z^2 symmetry, represses perpendicular anisotropy) to $d_{x^2-y^2}$ orbitals (promotes perpendicular anisotropy), hence resulting in electric field control of the strong interfacial perpendicular anisotropy in the system [42, 119]. It is worth noting that a similar analysis has been carried out for the CoFe|MgO system [120] (the most frequent structure of CoFeB, after B diffuses during annealing), observing very similar results to the case of Fe|MgO.

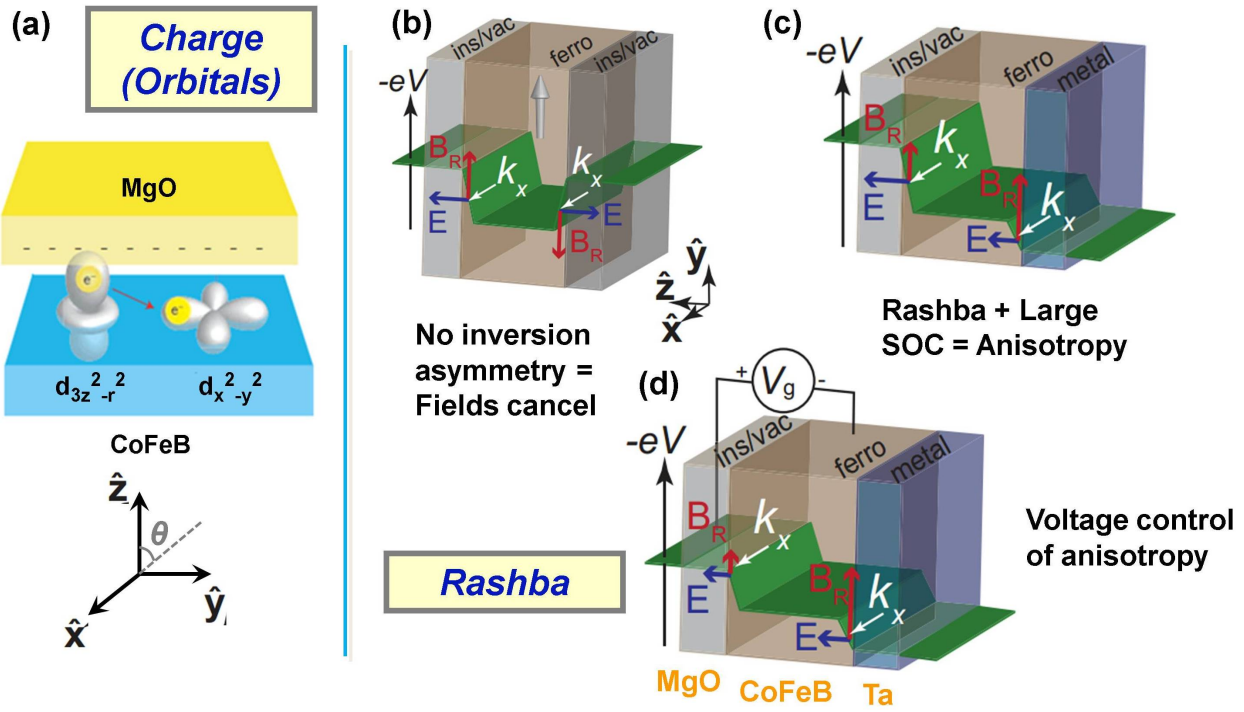

Fig. 2.4 (a) Orbitals: The perpendicular anisotropy at the CoFeB|MgO interface is attributed to contributions from hybridized Fe 3*d* to O 2p orbitals. By applying electric fields in the MgO, charge accumulates near the interface and modifies the occupancy between orbitals that promote prependular anisotropy to others that recess it (Modified from Ref. [42]). Rashba: (b) Due to changes in the work functions at the interfaces between different materials, there will be strong interfacial internal electric fields. Such electric fields translate into effective internal magnetic fields due the Rashba effect, described by the Rashba Hamiltonian in equation (2.4). If the structure does not break inversion symmetry along the z-axis, the fields will cancel each other. (c) When the inversion symmetry is broken, the total Rashba field, in the presence of a large spin-orbit coupling (SOC), translates into an anisotropy for the ferromagnetic material. (d) If the ferromagnet is sandwiched between an insulator and a metal, the application of an electric field will result in a change of the total electric field at the insulator|ferromagnet interface, allowing for electric field control of the anisotropy (Modified from Ref. [43]).

2.3.2 Rashba contribution

A recent work by Barnes, *et al.*, [43] proposes an additional possible mechanism for VCMA based on the contribution to anisotropy by the Rashba splitting of the band structure. The Rashba effect is a direct result of inversion symmetry breaking in the perpendicular (z-) direction. We first consider the case illustrated in Fig. 2.4(b), where a ferromagnetic material is

sandwiched between to identical materials (e.g., insulators). Due to the change of work functions in the ferromagnet|insulator interface, there will be a rapid change of the chemical potential over a very small region, translating into a large internal electric field E_{int} at the interface. In a relativistic frame, any electric field E at the interface will translate into a magnetic field, and if we consider SOC interaction, there will be a coupling to the electron spin via an effective Rashba field B_R. In the case of Fig. 2.4(b), given that we have two equal interfaces (i.e., there is no inversion asymmetry), the effective Rashba fields of the two interfaces will cancel each other and there will be no contribution from Rashba to the anisotropy of the material. However, if we break inversion symmetry by having two different interfaces, e.g., by placing two different materials as in the case of Fig. 2.4(c), the Rashba fields of the two interfaces will not cancel, thus there will exist a net Rashba effective magnetic field that results in splitting of the band structure of the ferromagnet [121]. Further, in the presence of SOC, such band splitting will result in a magnetic anisotropy for the ferromagnetic layer, as indicated in Fig. 2.4(c). Finally, we consider the case of Fig. 2.4(d), where the ferromagnet (e.g., CoFeB) is sandwiched between an oxide (e.g., MgO) and a metal (e.g., Ta). When an electric field is applied to the structure, the field will decay mostly in the oxide. In this situation, the electric field in the ferromagnet|oxide interface will have two components: The internal field because of the change of the work functions E_{int} plus the external (applied) electric field E_{ext}. Consequently, since the anisotropy is related to the total electric field $E = E_{int} + E_{ext}$ by the mechanism previously exposed, the anisotropy of the ferromagnet will be controlled by the applied field E_{ext} [43].

In Barnes model, the following Hamiltonian for the system is considered

$$H = \frac{p^2}{2m} - J_{ex}\vec{S}\cdot\vec{\sigma} + \frac{\alpha_R}{\hbar}(\sigma_x p_y - \sigma_y p_x) \tag{2.4}$$

The second term is related to the exchange interaction, where J_{ex} is the exchange coupling constant, $\vec{S}$ is the spin order parameter and $\vec{\sigma}$ are the Pauli matrices. The third term is related to the Rashba interaction, where $\vec{p}$ is the momentum and $\alpha_R = e\vartheta E$ is the Rashba parameter, where the dependence of the Hamiltonian on the total electric field E becomes explicit. Assuming a quadratic dispersion relation in a Stoner band model, Barnes model results in an angle-dependent energy for a 2D system of the form [43]

$$E_{an} = \frac{m}{2}\left(\frac{e\vartheta}{\hbar}\right)^2 E^2 \left[\frac{2T}{J_{ex}S} - 1\right] \sin^2\theta \tag{2.5}$$

where the dependence on the angle θ, as defined in Fig. 2.4, of the anisotropy energy E_{an} is in the form of an uniaxial anisotropy which will be perpendicular under the condition $T > J_{ex}S/2$ with $T = \hbar^2\left(\left\langle k_x^2\right\rangle_\uparrow - \left\langle k_x^2\right\rangle_\downarrow\right)/2m$ being related to the average Rashba crystal momentum shift $\left\langle k_x^2\right\rangle_\uparrow - \left\langle k_x^2\right\rangle_\downarrow$ due to the bands $\uparrow$ and $\downarrow$ splitting. As a consequence, the existence and strength of the perpendicular magnetic perpendicular anisotropy will be strongly related to the Rashba spitting and also, the anisotropy can be modulated by the electric field term $E^2 = \left(E_{int} + E_{ext}\right)^2$.

Barnes model offers interesting explanations to some experimental features of the VCMA effect. First, it explains the dependence of the perpendicular anisotropy and the VCMA itself on both interfaces of the ferromagnet, not only on the oxide|ferromagnet interface. Typically, heavy metals such as Ta and Hf are used to increase the perpendicular anisotropy of ultrathin magnetic films such as CoFeB [122], whose contribution may be expected in Barnes model due to the increase in the effective Rashba parameter α_R based on the larger spin-orbit coupling of the heavy metals, plus larger internal fields if the chosen heavy metal has the right work functions compared to CoFeB and MgO for example. Also, Barnes model predicts a quadratic dependence

of the anisotropy energy on the total electric field $E^2 = \left(E_{int} + E_{ext}\right)^2$. Most of the VCMA experimental papers, including our own characterization of the VCMA effect in our samples presented in Chapters 3 and 4, report a linear dependence of the VCMA on E_{ext}. However, a recent work by Nozaki, *et al.*, [123] reported a quadratic dependence for the first time by using a MgO(2.5nm)|FeB|MgO(1.5nm) stack. Due to the different thicknesses of the MgO layers, the applied electric field will mostly decay on the thicker MgO, therefore, only the thick MgO|FeB interface should be relevant in principle for the orbital mechanism to the VCMA; yet, the introduction of a second MgO makes the VCMA quadratic. This result can be well explained in Barnes model taking into account that two approximately similar MgO layer sandwich the FeB in the MgO|FeB|MgO stack, hence reducing the symmetry breaking in z-direction and consequently, making the total internal field E_{int} very small. Hence, taking into account equation (2.5), a quadratic dependence of the form $E^2 = \left(E_{int} + E_{ext}\right)^2 \sim E_{ext}^2$ on the external electric field is well expected. In the other cases, when a MgO|ferromagnet|heavy metal stack is considered, the internal field E_{int} will be very large compared due to the large inversion asymmetry along the z-axis and the potential differences in the change of the work functions across the interfaces. Due to the rapid change across the interface of the work functions, typically E_{int} is much larger than the range of experimentally accessible values for E_{ext}, the latter limited by dielectric breakdown of the oxide. If $E_{int} \gg E_{ext}$, then the quadratic dependence of the electric field can be approximated to

$$E^2 = \left(E_{int} + E_{ext}\right)^2 = E_{int}^2 \left(1 + \frac{E_{ext}}{E_{int}}\right)^2 \approx E_{int}^2 (1 + \frac{E_{ext}}{2E_{int}}) = E_{int}^2 + \frac{E_{int}}{2} E_{ext} \tag{2.6}$$

when $E_{ext} / E_{int} \ll 1$. Under such condition, hence, the dependence of the VCMA effect on the external electric field E_{ext} becomes approximately linear (see equation (2.6)), in good agreement with the experimental observations and first principle calculations performed to study the orbital contribution to VCMA. Finally, different signs for the slope of the dependence of the VCMA on E_{ext} are reported depending on the chosen heavy metal [124]. This can also be explained in Barnes model taking into account that the sign of the VCMA will depend on the sign of E_{int} (see equation (2.6)), the latter connected to the work function of the heavy metal.

Nevertheless, it should be noted that Barnes work is based on a simplified model assuming a quadratic dispersion relation for the energy, neglecting the contributions from multiple bands and the role of the crystal potential. Hence, still first principle calculations will be required to calculate the band splitting and the anisotropy due to Rashba. Further, since the band structure itself is sensitive to the electric fields and charges accumulated in the interface, it is very likely that the VCMA is due to a coupled effect between orbitals and Rashba contributions.

2.3.3 Macrospin description

Independent of the detailed physical mechanisms, the VCMA can be parameterized in a more simplified model based on a macrospin (e.g., single-domain) description. As described throughout the chapter, the electric field control of magnetism in the VCMA effect is based on the modulation of an interfacial anisotropy. To the lowest order, the energy associated to a uniaxial anisotropy can be written as $E_{an} = K_{1,eff} \sin^2 \theta$, where θ is the polar angle as defined previously in Fig. 2.4, and from equation (1.9), the effective anisotropy in a thin-film ferromagnet with interfacial perpendicular anisotropy is

$$K_{1,eff} = \frac{M_s H_{k,eff}^{\perp}}{2} \approx \frac{S_i}{t} - 2\pi M_s^2 \tag{2.7}$$

where M_s is the saturation magnetization, $H_{k,eff}^{\perp}$ the effective anisotropy field, S_i the interfacial anisotropy energy and t the thickness of the ferromagnetic layer, as defined previously in section 1.4.3. Obviously, the sign of $K_{1,eff}$ will determine the minimum energy condition for E_{an}, leading to a stable perpendicular configuration if $K_{1,eff} > 0$ (minimum energy at $\theta = 0^{\circ}$ or $\theta = 180^{\circ}$), or otherwise a stable in-plane condition if $K_{1,eff} < 0$ (minimum energy at $\theta = 90^{\circ}$ or $\theta = 270^{\circ}$).

In the presence of the VCMA effect, the effective anisotropy becomes a function of the applied (external) electric field $E_{ext} = V / d$, where V is the applied voltage and d the thickness of the oxide where such field decays. Therefore, by modifying equations (1.9) and (2.7), the voltage-controlled effective magnetic anisotropy can be now written as

$$K_{1,eff}(V) = \frac{M_s H_{k,eff}^{\perp}(V)}{2} = \frac{S_i - \sum_n \xi_n \left(\frac{V}{d}\right)^n}{t} - 2\pi M_s^2 \tag{2.8}$$

where ξ_n are the VCMA (or magnetoelectric) coefficients in the Taylor expansion over the electric field V / d. This is a general description that can be used for any type of functional form for the dependence of the VCMA on the applied field. However, as discussed in section 2.3.2, most of the experiments report on a linear dependence on electric field, therefore equation (2.8) can be simplified to

$$K_{1,eff}(V) = \frac{M_s H_{k,eff}^{\perp}(V)}{2} = \frac{S_i - \xi \frac{V}{d_{\mathrm{MgO}}}}{t_{\mathrm{CoFeB}}} - 2\pi M_s^2 \tag{2.9}$$

where ξ is the linear VCMA (or magnetoelectric) coefficient used to parameterize the strength and the sign of the dependence of the VCMA effect on the applied electric field. The VCMA coefficient (in units of fJ/V-m) is a stack dependent parameter quantifying the change of interfacial anisotropy energy (in units of μJ/m^2 or merg/cm^2) per unit electric field (in units of V/nm). Specifically,

$$\xi\ [\text{fJ/ V-m}] = \frac{\text{Change of Surface Anisotropy } [\mu\text{J/m}^2]}{\text{Electric Field [V/nm]}} \tag{2.10}$$

The focus of this work is on Ta|CoFeB|MgO-based MTJs since using Ta as an underlayer results in one of the largest TMR ratios given that Ta acts as a good sink for boron absorption during annealing and promotes the right crystallization of the CoFeB|MgO stack [52]. Further, Ta also promotes the perpendicular magnetic anisotropy in CoFeB|MgO, translating into an interfacial anisotropy energy on the order $S_i \sim 1$ erg/cm^2 = 1 mJ/m^2 [55, 61]. In fact, out of the metals typically used as an underlayer in CoFeB|MgO MTJ devices (e.g., Pt, Pd, Ru, V), only Hf results in a larger S_i compared to Ta [122].

For the system of interest in this work, i.e., for typical Ta|CoFeB|MgO-based MTJs, the magnitude of the VCMA coefficient is on the order of 20-40 fJ/V-m [55, 109]. Hence, the application of an electric field of 1 V/nm results in a change of 20-40 μJ/m^2 = 0.02-0.04 mJ/m^2 for the interfacial perpendicular anisotropy, or in other words, a change of around 2-4% in the total anisotropy given the values previously cited for S_i. Applying fields much larger than 1 V/nm in an MTJ is limited by the dielectric breakdown of the MgO [125, 126], thus the VCMA effect that can be obtained Ta|CoFeB|MgO-based MTJs is currently not very strong. Moreover, a simple calculation based on the experimental results in our samples yields that the efficiency in

translating the energy of charging the MgO into modulating the perpendicular anisotropy is currently only ~0.25%, showing that there is a large room for improving the VCMA effect.

There are presently multiple efforts in experiments and via first-principles calculations trying to increase the strength of the VCMA coefficient ξ. Fig. 2.5 shows a summary of the coefficients obtained so far in different materials systems [42, 108, 109, 113, 119, 123, 127-134], both in theoretical calculations and experimentally. In the figure, a "Positive VCMA" is defined as when the accumulation of negative charges near the ferromagnet|oxide interface increases the perpendicular anisotropy; meanwhile a "Negative VCMA" requires a depletion of negative charges to increase the perpendicular anisotropy. The quadratic dependence observed in Ref. [123] has been also included by separating the slopes reported for different polarities of the electric field.

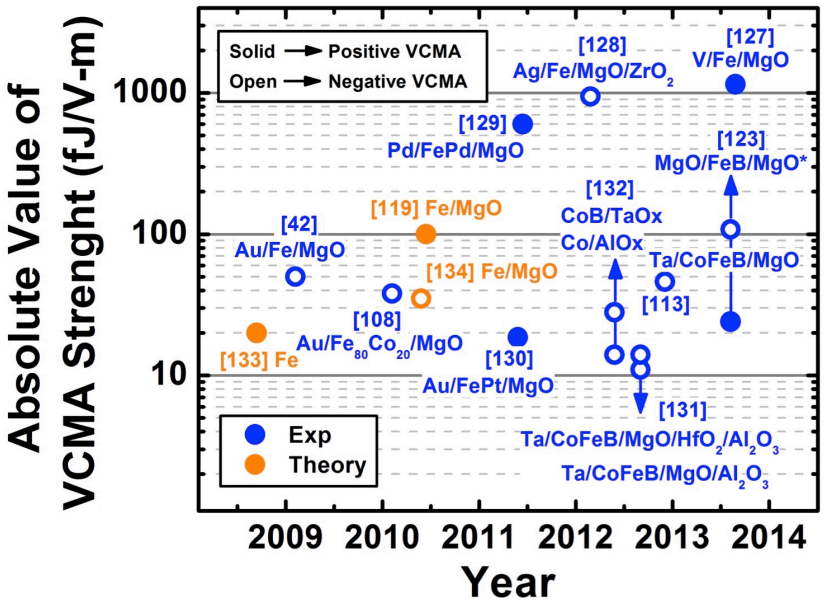

Fig. 2.5 Summary of the absolute value of the VCMA coefficients ξ reported in the literature for different material systems. The work of Ref. [123] (marked with *) has been included by separating the slopes for different polarities of the applied voltage.

It can be clearly observed that there are indeed material systems with ξ at least one order of magnitude larger compared to Ta|CoFeB|MgO. The works in Refs. [127] and [128] report the largest VCMA coefficients so far in the literature, however both material systems show resistive-RAM-like behavior, indicating that the increase of the VCMA may be due to the flow of ions in the VO_x and ZrO_2 oxides respectively. Using oxides where ions move may increase the charge accumulation/depletion, however this would also decrease the endurance of the memory element, eliminating one of the advantages of MRAM (very large endurance). The work by Bonell, *et al.*, [129] reports a VCMA coefficient larger than 600 fJ/V-m in an epitaxial FePd|MgO system, pointing towards a large influence of strain over strength of the VCMA. Nevertheless, finding a materials system that has simultaneously large TMR ratio and large ξ is still a big challenge in the field.

2.4 Scaling of VCMA as a switching mechanism

One of the key questions for any emerging technology is how it scales to small technology nodes, where technologies that offer advantages, or at least keep their performance when the device is scaled down are preferred. In section 1.6, the scalability of STT-MRAM was discussed by analyzing the ratio between the critical switching current over the thermal stability ratio (I_c / Δ) as a figure of merit. In this section, the analogous critical voltage over thermal stability (V_c / Δ) figure of merit is derived and analyzed for the case where the VCMA effect is used to switch MTJ devices [135]. The discussion will focus in perpendicular devices since, as previously discussed in section 1.4, scaling in-plane MTJ devices to very small technology nodes is limited, even when considering increasing the thickness of the free layer to keep the device thermally stable at small nodes. In the latter scenario, thicker free layers would reduce the

effectiveness of the VCMA due to its interfacial nature, making scaled in-plane devices not ideal for VCMA-driven switching.

In section 1.4.3, the thermal stability factor at equilibrium (i.e., without any applied voltage) for a perpendicular MTJ device with interfacial perpendicular anisotropy was derived in the macrospin approximation to be (see equation (1.9))

$$\Delta = \frac{E_b}{kT} = \Delta(V=0) = \frac{\left(S_i - 2\pi\left(N_z - N_{x,y}\right)M_s^2 t\right)A}{kT} \tag{2.11}$$

where the demagnetization factors in the perpendicular (out-of-plane) and in the in-plane direction, N_z and $N_{x,y}$ respectively, have been included to increase the accuracy of the model in nodes where the thickness of the free layer t becomes comparable to the lateral dimensions of the MTJ device. As illustrated in Fig. 2.6, the thermal stability in equation (2.11) is related to the energy barrier between the two perpendicular stable states, where the maximum barrier height is at the in-plane condition.

In the presence of the VCMA effect, the energy barrier becomes dependent on the applied voltage V. In particular, by modifying equation (2.11) to include the VCMA term,

$$\Delta(V) = \frac{\left(S_i - \xi\frac{V}{d} - 2\pi\left(N_z - N_{x,y}\right)M_s^2 t\right)A}{kT} = \Delta(V=0) - \frac{\xi A}{dkT}V \tag{2.12}$$

Therefore, from equation (2.12) it is clear that both the VCMA coefficient ξ, but notably, also the area A control the rate of the energy barrier lowering by the applied voltage. Hence, as the device is scaled down, increasing the VCMA coefficient proportionally to the reduction of the area would be required to keep the same rate of control of the energy barrier by the applied voltage.

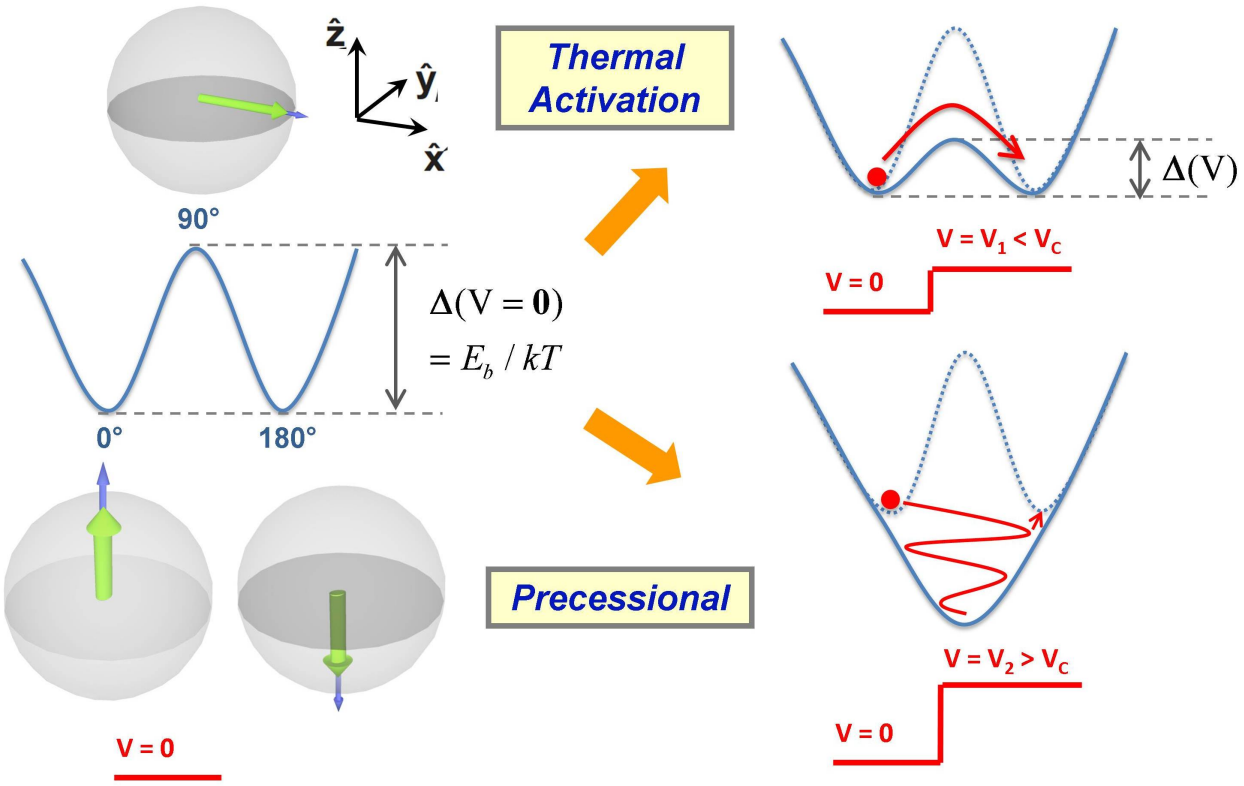

Fig. 2.6 At equilibrium (V=0), the energy barrier separates the two non-volatile perpendicular stable states (0° and 180°), where the energy becomes maximum in the in-plane condition (90° or 270°). In order to switch between the perpendicular states, the VCMA effect is used to lower the energy barrier. If the energy barrier is partially lowered, thermal activation can result in a switching event. On the other hand, if the barrier is fully destroyed, a new minimum will form in the in-plane direction. Yet, by timing the precession to the in-plane condition, a switching event may be obtained. The critical voltage, which separates these two regimes, is defined as the voltage required to lower the energy barrier to zero.

VCMA-driven switching can be obtained in two different regimes, as shown in Fig. 2.6. In the thermally activated regime, the barrier is only partially lowered and a switching event can be obtained in the presence of thermal fluctuations that activate the process. The average time that it takes for the magnetization to switch because of thermal fluctuations is related to the dwell time (as defined in section 1.4.2), which becomes a function of the applied voltage in the presence of the VCMA effect. Specifically, by modifying equation (1.4) taking into account the

voltage-dependent dwell time in the presence of the VCMA effect in equation (2.12), we find that

$$\tau(V) = \tau_0 \exp\left(\Delta(V)\right) = \tau_0 \exp\left[\Delta(V=0)\right] \times \exp\left[-\frac{\xi A}{dkT} V\right] \tag{2.13}$$

The critical switching voltage V_c is defined as the voltage required to reduce the energy barrier between the perpendicular states to $\Delta(V_c) = 0$, or in other words, the voltage required to obtain a switching event on average every $\tau(V_c) = \tau_0$, where τ_0 is the attempt time. Hence, the condition $\Delta(V_c) = 0$ in equation (2.12) results in an expression for the critical voltage of the form

$$V_c = \frac{dkT}{\xi A} \Delta(V=0) \tag{2.14}$$

Any voltage larger than V_c reconfigures the magnetic easy-axis to the in-plane condition, therefore creating an energy minimum along this direction as illustrated in Fig. 2.6. Under such regime, switching can be obtained by proper timing of the magnetic dynamics when the magnetization is precessing to the in-plane direction. Finally, the critical voltage to thermal stability ratio figure of merit is

$$\frac{V_c}{\Delta(V=0)} = \frac{dkT}{\xi A} \tag{2.15}$$

where the figure of merit depends only on the thickness of the oxide d, the area of the device A and the VCMA coefficient ξ. The thickness of the oxide (e.g., MgO) is mostly set in MTJ devices by practical considerations, and small changes in thickness of the tunneling oxide d result in exponential changes of the MTJ resistance, therefore the value of d is designed taking into account the desired MTJ resistance, however its value only changes in a very small range. Further, a constant electric field scaling rule would be given by

$$\frac{V_c / d}{\Delta(V=0)} = \frac{kT}{\xi A} \tag{2.16}$$

Consequently, the scaling of the VCMA effect is marked by a trade-off between the device area A and the VCMA coefficient ξ.

Fig. 2.7 shows a simplified scaling analysis for the required interfacial perpendicular anisotropy energy S_i and VCMA coefficient ξ for technology nodes from 90 nm to a theoretical 5 nm limit. Three values of the thermal stability factor are considered: $\Delta = 40$, 60 and 80. Even though a $\Delta = 40$ may be enough to assure the thermal stability, still when considering the range of temperatures of operation and the statistical array considerations briefly highlighted in section 1.4.1, Δ as large as 80 may be required in a GB array intended for long-term storage after taking into consideration the capabilities of error-correcting codes (ECC) in the memory [78].

The scaling analysis for S_i in Fig. 2.7(a) is based on equation (2.11). The demagnetization factors were calculated using the elliptical/circular cylinder approximation described in the work by Beleggia, *et al.*, [136]. An M_s value of 1000 emu/cm^3 was assumed, but given the small variation in M_s between different typical ferromagnetic materials, especially those that lead to a high TMR currently, this quantity should not have a large impact over the scaling analysis. We assume that the minimum thickness of the free layer is 1 nm for practical considerations, including film continuity and the crystallinity required to obtain a large read-out signal. For the largest technology nodes in consideration (90 nm, 65 nm and 45 nm at $\Delta = 40$), the regular CoFeB|MgO system with $S_i \sim 1$ erg/cm^2 may be used to meet the thermal stability factor requirement. The inset table in Fig. 2.7(a) shows the thicknesses that would be needed in such scenario. After a thickness of 1 nm is reached, an increase of S_i is needed for every node. It is important to note that current available technology has been reported for S_i values in order to

reach the 22 node (marked by green arrow in Fig. 2.7(a)) by using a double MgO sandwich to CoFeB [137] in order to double the interfacial anisotropy; however, further material engineering is required to reach smaller nodes using the interfacial anisotropy approach.

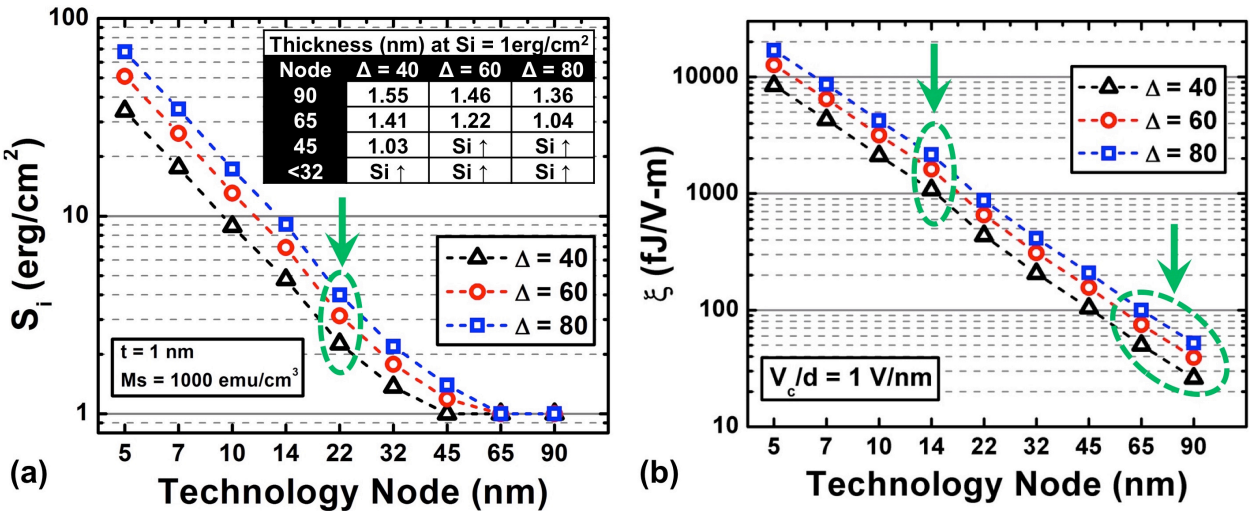

Fig. 2.7 (a) Scaling for the interfacial anisotropy energy S_i required to meet thermal stability factors of $\Delta = 40$, 60 and 80. The scalability requirements for the largest technology nodes can be reached by tuning the free layer thickness. However, as the device is further scaled, new materials with larger S_i values are required. The green arrow indicates that there is currently technology available for the 22 nm node. (b) Scaling of the VCMA coefficient ξ. The current Fe|MgO-based systems can well meet the requirement for 90 and 65 nm nodes, meanwhile the reports on other materials systems (see Fig. 2.5) are good to scale down to the 14 nm node (Data pending to be published).

The scaling analysis for the VCMA coefficient ξ is shown on Fig. 2.7(b). The analysis is based on equation (2.16) and only assumes a constant electric field scaling at 1 V/nm, which would translate into switching voltages close to 1 V across different technology nodes. The previously discussed trade-off between area and VCMA coefficient is clearly observed in Fig. 2.7(b). As shown in Fig. 2.5, the current Fe|MgO-based systems can reach VCMA coefficients below 100 fJ/V-cm, good enough for the 90 and 65 nm nodes (right green arrow on Fig. 2.7(b)).

However, the largest VCMA coefficients reported in the literature (see Fig. 2.5) so far could be the route to scale down to the 14 nm node, as highlighted by the left green arrow on Fig. 2.7(b).

Finally, we conclude this section by adding some important notes on the obtained results: First, it should be noticed that voltages of the opposite polarity (e.g., negative voltages in equation (2.13)) will increase $\tau(V)$, hence further stabilizing the bit. This characteristic of the VCMA effect is fundamentally different from STT. Second, in order to avoid switch-backs in the thermally activated regime, an additional magnetic field or charge current is required as described by Khalili Amiri, *et al.*, [135], and as demonstrated experimentally in Chapter 5 of this work. Experimental demonstrations of precessional switching in nanoscale MTJ devices are included in such chapter. Finally, the description here developed is based on a macrospin approximation; however, the thermal stability and switching voltages may be influenced also by micromagnetic effects (good examples are given in Refs. [81] and [138]), topic outside of the scope of this work.

2.5 Magnetoelectric RAM (MeRAM) in the memory hierarchy

Replacing STT by the VCMA effect as a writing mechanism in MRAM can result in huge advantages in terms of energy efficiency by avoiding the flow of large charge current during the switching process, while keeping other advantages of STT-MRAM in terms of endurance, radiation-hardness, compatibility with CMOS fabrication, etc. One of the main results of this dissertation is the demonstration of VCMA-induced switching of nanoscale MTJ devices, opening the route for a new magnetoelectric RAM architecture, also named MeRAM. In this section, we outline a prospective benchmarking of MeRAM versus competing technologies.

Unlike devices for logic, where CMOS transistors are the dominant technology, the memory business is currently spread between different alternatives depending on the capacity and speed requirements, leading to the memory hierarchy shown in Fig. 2.8. The concept of a universal memory is considered the "holy grail" for academic and industrial researcher in the area; however, none of the available technologies so far can be used across all the applications by tuning the memory bits, opposite to the case of logic devices with CMOS transistors.

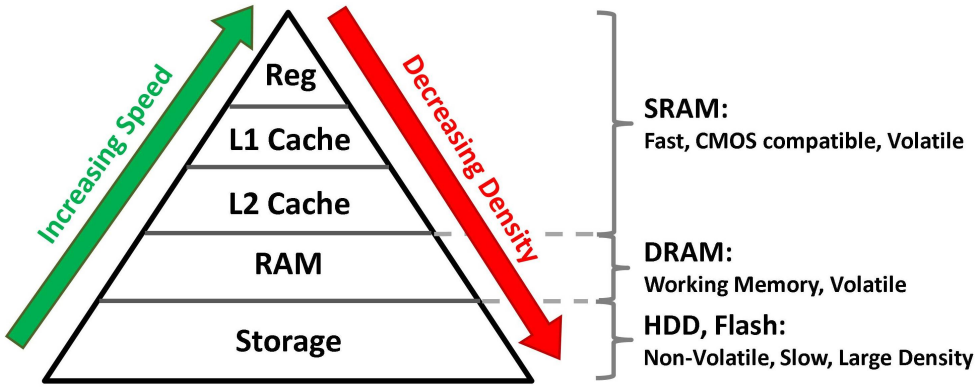

Fig. 2.8 Currently, the absence of a universal memory translates into a memory hierarchy where different technologies are used to achieve specific tasks in computing systems. The volatile SRAM is used next to the processor register and cache, meanwhile DRAM, also volatile, is used as working memory. The slower but dense non-volatile storage media (HDD or Flash) store the information. It is highly desired to find alternative non-volatile technologies that could be replacements for the volatile SRAM and DRAM.

In current electronic systems, during computation, information is often temporally stored in Static Random Access Memory (SRAM), which acts as cache memory placed close to the CMOS logic (often on the same chip), as well as in Dynamic Random Access Memories (DRAM) acting as the principal working memory (with higher density, and hence larger memory chip capacities than SRAM), and is then permanently stored in NAND Flash (e.g. in solid-state drive SSD storage), or hard disk drives (HDDs). Table 2.1 compares the most important performance parameters for SRAM, DRAM and NAND Flash (i.e., dominant existing memory technologies)

versus STT-MRAM and MeRAM. Among the established technologies, SRAM is the fastest (operating in the GHz range), needs fairly little power (~ 100 fJ per switch), and has virtually unlimited endurance. However, SRAM is volatile, has a very low density (i.e., large cell size) and its standby power consumption becomes a problem especially as the transistor dimensions are scaled down, leading to higher leakage currents. At scaled technology nodes, not only leakage power and process variability become a "brick wall", but also it has been argued that the silicon area for a system-on-chip (SoC) end product is dependent on the SRAM bit cell size far more than on the general transistor density, taking up to 68% of the chip area on average by 2017 [139, 140]. Thus, there is currently a need for alternatives to SRAM that can be integrated next to the logic circuits.

DRAM has a much higher density compared to SRAM, but is also volatile and needs a periodic refresh current, which results in significant power consumption overhead. DRAM scaling has also major challenges due to the increase in RC interconnect delay and parasitics, and the need for extremely high aspect ratio capacitors to avoid reduction of the cell capacitance, the latter impacting retention times and sensing margin for the cell. In the last years, embedded DRAM (eDRAM) has emerged as an attractive alternative that can be integrated next to the CMOS logic. However, eDRAM uses fast logic transistors which have higher leakage than those used in conventional DRAM and hence, its refresh requirement is also higher than that of DRAM (~tens of μs vs ~tens of ms, respectively) [141]**.**

NAND flash has the highest density compared to SRAM and DRAM, and is non-volatile. However, it is extremely slow and offers very limited endurance, restricting its application space to storage with infrequent access only. It also has the largest energy consumption per bit, and unlike the other technologies, large voltages are needed for its operation. Finally, the other

conventional non-volatile technology is HDDs. Currently, HDDs remain as the technology with the lowest cost per bit, and it is one of the preferred technologies for large capacity storage (together with magnetic tapes). However, the write and read processes rely on mechanically-driven heads, making HDDs extremely slow and unusable as a random access memory or in applications where short reading and writing times are needed.

Technology	SRAM	DRAM	NAND Flash	STT-MRAM	MeRAM
Energy/bit (fJ)	100	1,000	10^6	100	≤ 1
Write Speed (ns)	1	20	10^6	1 – 10	1 – 10
Read Speed (ns)	1	30	50	1 – 10	1 – 10
Density (area in F^2)	> 30	6 – 10	4	8 – 30	4 – 8
Endurance (Cycles)	Very High	Very High	Low	Very High	Very High
Nonvolatile	No	No	Yes	Yes	Yes
Standby power	Leakage Current	Refresh Current	None	None	None
Cost overhead vs. CMOS	Large area (6T)	Separate process	Separate process	Back-end (BEOL) process	Back-end (BEOL) process
Nonvolatile Logic Capability	No	No	No	Very limited due to power	Yes

Table 2.1 Comparison of existing (non-magnetic) and emerging spintronic memory technologies, highlighting STT-MRAM (using current-induced switching) and MeRAM (using electric-field-controlled switching) [7].

In order to address the needs of the conventional memory hierarchy, multiple emerging technologies are being explored [141, 142], MRAM being one of the strongest candidates. As

previously discussed in Chapter 1, MRAM is non-volatile (zero stand-by power), has very high endurance, is radiation hard, allows for fast read and write times (~ nanoseconds) and it can be easily integrated in the back-end of the line (BEOL) of CMOS fabrication. Further, the usage of the STT effect gave rise to the STT-MRAM technology, which permits fully electrical read and write of the information in the MTJ memory elements. As shown in Table 2.1, the use of spin-polarized currents allows for switching energies and speeds close to SRAM, while the density can be better than SRAM, making STT-MRAM a suitable candidate for a number of embedded applications.

However, STT-MRAM also faces fundamental challenges as previously discussed in Chapter 1. Particularly, the switching current over thermal stability ratio ($I_{c0}/\Delta = 4e\alpha kT/\hbar\eta$, derived in section 1.6.2) in STT-MRAM remains constant under scaling; therefore, the switching current is expected to remain approximately constant across technology nodes. This presents a fundamental problem for the scaling of current-controlled STT-RAM, as the transistors needed to drive this constant switching current will not significantly shrink with successive technology nodes, hence hitting a current-drive-limited barrier on transistor size (hence cell area). Fig. 2.9(a) shows the estimated access transistor width sizes for different technology nodes, where the projected CMOS operating voltage and current drive capability were obtained from Refs. [79, 80]. While lower switching current densities can delay the onset of the scaling dilemma for STT-MRAM, even optimistic switching current densities as low as 0.5 MA/cm^2 represent a sizeable penalty in terms of area at scaled technology nodes.

A clear alternative to address this issue is replacing the current-controlled STT by the electric-field-driven VCMA effect. In MeRAM, the switching voltages are associated with very small leakage currents through the device, which allow for the use of minimum-sized transistors

at each technology node, hence imparting a growing density advantage with progressive scaling to smaller bit dimensions (see Fig. 2.9(a)). The latter assumes that a constant switching voltage can be sustained as the device is scaled, which is possible by following the scaling requirements highlighted in section 2.4. The usage of minimum size access transistors effectively translates into cell sizes as small as 6-8F^2 with planar minimum size transistor and 4F^2 by using vertical transistors or diode as access devices, as demonstrated in later in Chapter 5.

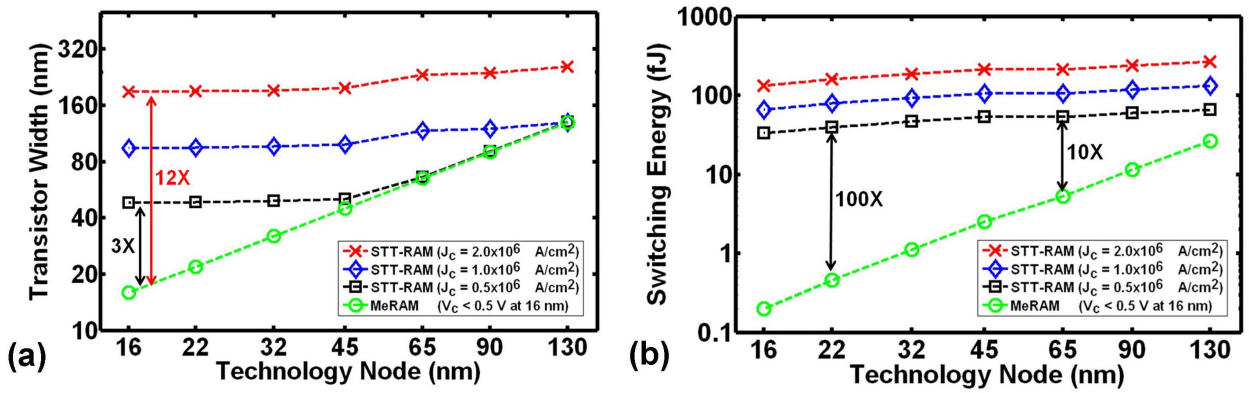

Fig. 2.9 (a) Comparison of transistor width scaling for 1-transistor/1-MTJ STT-MRAM and MeRAM cells across technology nodes down to 16 nm, for three different values of STT-MRAM switching current densities. While voltage-controlled MeRAM allows for using minimum transistor widths at each technology node, thereby maximizing density, STT-MRAM bit stability dictates a constant switching current even at scaled bit dimensions, leading to a saturation behavior in the transistor width. (b) Comparison of switching energy (per bit) for STT-MRAM and MeRAM. While MeRAM allows for reduced switching energies as the bit dimensions are reduced, STT-MRAM constant switching current leads to a saturation behavior in the energy efficiency. The slight reduction of STT-MRAM write energies is due to the reduced operating voltages at smaller nodes, which dictate a lower write power dissipation. However, this comes at the cost of drastically reducing the *RA* product of MTJ cells, which may itself pose a limitation on scaling. The gap in energy efficiency increases with reduced bit dimensions [143].

A similar scaling advantage of MeRAM versus STT-MRAM is possible in terms of energy efficiency. While MeRAM already provides an advantage over STT-MRAM in terms of switching energy per bit, this advantage grows quickly as bit dimensions are scaled down. This is

due to the fact that, assuming a constant write time t_w across technology nodes, STT-MRAM bits retain an approximately constant write energy $E_w = RI_c^2 t_w$, provided that the MTJ's resistance-area product (*RA*) can be reduced sufficiently (i.e., MgO barrier can be made thin enough) to prevent the write voltage RI_c from increasing when the area is scaled down. However, this may eventually lead to reliability issues due to the increasingly thin MgO barriers needed for this scaling scheme. In the case of MeRAM, on the other hand, thicker MgO barriers can be used, partially relieving reliability and breakdown issues. Further, the write energy $E_w = CV_c^2 + \left(V_c^2 / R\right)t_w$ (where C is the capacitance of the MTJ) reduces with each technology node, as the resistance increases and C decreases due to the smaller bit area A. This energy scaling advantage is illustrated in Fig. 2.9(b), which compares the projected write energy per bit for MeRAM and STT-MRAM (assuming three different values of STT-MRAM switching current densities), for a write time of 1 ns. It shows that, while even at present technology nodes MeRAM would represent a significant improvement of energy efficiency, the efficiency gap would grow further at scaled technology nodes. These projections indicate that MeRAM would be able to address memory applications where energy efficiency and/or density are major concerns (e.g. embedded SRAM Cache, and DRAM, respectively), where STT-MRAM would face a limitation due to scaling.

Finally, dynamic switching energies of STT-MRAM are still around two orders of magnitude higher compared to CMOS (~ 0.1-1 fJ/switch), limiting the possibility of integration of STT devices at the gate level with CMOS for non-volatile logic applications [12], where frequent access of the memory device is needed. Therefore, VCMA-driven devices and MeRAM, with potential energy efficiencies very close to CMOS, provide a route to build non-volatile logic circuits at the gate level with instant-on capabilities.

2.6 Compact modeling of the VCMA effect

In order to study the performance of VCMA-driven MTJ devices on actual circuit implementations, models that can be integrated with conventional circuit design platforms are required. Albeit micromagnetic simulations are able to capture additional physical phenomena that cannot be described in macrospin models [144], the complexity and large computational times required for micromagnetic simulations force the use of more simple macrospin descriptions in the models implemented for circuit design.

The evolution of the magnetization vector $\vec{m} = \vec{M} / M_s = (m_x, m_y, m_z)$ is described by the Landau–Lifshitz–Gilbert (LLG) equation with the STT term, in SI units (see Fig. 2.4 for the definition of the coordinate axis) (see equations (2) and (4) in Ref. [144])

$$\frac{1}{\gamma'}\frac{d\vec{m}}{dt} = -\vec{m}\times\vec{H}_{eff}' - \alpha\vec{m}\times\left(\vec{m}\times\vec{H}_{eff}'\right) + I_c\frac{\hbar P}{2\mu_0 e M_s A t}\vec{m}\times\left(\vec{m}\times\vec{p}\right) \tag{2.17}$$

where $\gamma' = \gamma/(1+\alpha^2)$ is the reduced gyromagnetic ratio, α is the damping factor, P is the STT polarization, $\vec{p}$ is the polarization vector and $\vec{H}_{eff}'$ is the effective magnetic field. The first, second and third term in equation (2.17) are the precessional, damping and STT terms respectively. A previous work by Dorrance, *et al.*, [145] implemented the solution of this equation in a Verilog-A environment, and the model was used to simulate the behavior of in-plane STT-driven MTJ devices. For this dissertation, the cited model was extended to include the possibility of field-like torque in STT [146, 147], as well as the presence of interfacial perpendicular anisotropy, VCMA effect and thermal fluctuations to capture thermally-induced (e.g., stochastic) processes. The resulting model is available in Verilog-A [148, 149] and MATLAB environments.

In the revised model, the following extension of the LLG equation is considered

$$\frac{1}{\gamma'}\frac{d\vec{m}}{dt} = -\vec{m}\times\left(\vec{H}_{eff}(V)+\vec{H}_{th}\right)-\alpha\vec{m}\times\left(\vec{m}\times\vec{H}_{eff}(V)\right)$$
$$+I_c\frac{\hbar P}{2\mu_0 eM_s At}\left[\vec{m}\times\left(\vec{m}\times\vec{p}\right)+\left(\beta_1+\beta_2 I_c\right)\vec{m}\times\vec{p}\right] \tag{2.18}$$

The thermal noise is introduced by adding a thermal field $\vec{H}_{th}$ into the precessional term, following the Langevin approach as described by Sun, *et al.*, in Ref. [150]. Specifically, the thermal field is given by (the derivation can be found in Refs. [151] and [152])

$$\vec{H}_{th} = \vec{\sigma}\sqrt{\frac{2kT\alpha}{\mu_0 M_s\gamma' V\Delta t}} \tag{2.19}$$

where V is the volume of the macrospin element, Δt is the characteristic time (set mostly by the time step to solve the LLG equation) and $\vec{\sigma} = (\sigma_x,\sigma_y,\sigma_z)$ are three uncorrelated random Gaussian variables with mean zero and variance 1. The field-like torque is implemented by the $\left(\beta_1+\beta_2 I_c\right)\vec{m}\times\vec{p}$ term, acting as a field in the $\vec{p}$ direction. The constants β_1 and β_2 are the linear and quadratic field-like torque constants, respectively, which are a function of the material stack [153].

The interfacial anisotropy and VCMA effect are implement via the effective field $\vec{H}_{eff}(V)$, which becomes a function of the applied voltage V due to VCMA. The effective field can be decomposed in several components, specifically

$$\vec{H}_{eff}(V) = \vec{H}_{ext}+\vec{H}_{demag}+\vec{H}_{ani}-\vec{H}_{VCMA}(V) \tag{2.20}$$

where $\vec{H}_{ext}$ is the external (applied) magnetic field and $\vec{H}_{demag} = -M_s\overleftrightarrow{N}\cdot\vec{m}$ is the effective demagnetization field with $\overleftrightarrow{N}$ being the geometrical demagnetization tensor (see the discussion on demagnetization field in section 1.4.1). The effective field due to anisotropy can be related to the anisotropy energy E_{ani} by

$$\vec{H}_{ani} = -\frac{1}{\mu_0 M_s}\frac{\partial E_{ani}}{\partial \vec{m}} \tag{2.21}$$

The anisotropy energy is given by $E_{ani} = (S_i / t)\sin^2\theta = (S_i / t)(1-\cos^2\theta) = (S_i / t)(1-m_z^2)$, where θ is the polar angle as defined in Fig. 2.4. Therefore, taking into account that the anisotropy energy only has an m_z dependence, the effective anisotropy field is

$$\vec{H}_{ani} = -\frac{1}{\mu_0 M_s}\frac{\partial E_{ani}}{\partial m_z}\hat{z} = \frac{2S_i}{\mu_0 M_s t} m_z \hat{z} \tag{2.22}$$

Similarly, the energy due to VCMA is $E_{VCMA}(V) = (\xi V / dt)\sin^2\theta = (\xi V / dt)(1-m_z^2)$, and therefore the voltage-controlled effective field due to VCMA would be given by

$$\vec{H}_{VCMA}(V) = -\frac{1}{\mu_0 M_s}\frac{\partial E_{VCMA}(V)}{\partial m_z}\hat{z} = V\frac{2\xi}{\mu_0 M_s dt} m_z \hat{z} \tag{2.23}$$

These field are implemented as contributions to the total effective field and allow to simulate in-plane and perpendicular junctions in the presence of the VCMA effect.

The resulting model can be further extended taking into account detailed experimental characterization of VCMA-driven MTJ dynamics in order to build a representative model that captures the required physics to obtain accurate circuital and system simulations. In this work, two of such detailed characterizations are performed: Chapter 3 reports on the temperature dependence of the interfacial anisotropy S_i and the VCMA coefficient ξ, while Chapter 4 demonstrates that higher order contributions to the anisotropy, on the order of $\sin^4\theta = (1-m_z^2)^2$ should be taken into account. In such scenario, following a very similar procedure, it can be easily shown that the second order effective anisotropy and VCMA fields would be given by

$$\vec{H}_{ani,2} = \frac{4S_{i,2}}{\mu_0 M_s t}(1-m_z^2) m_z \hat{z} \quad \text{and} \quad \vec{H}_{VCMA,2}(V) = V\frac{4\xi_2}{\mu_0 M_s dt}(1-m_z^2) m_z \hat{z} \tag{2.24}$$

where $S_{i,2}$ and ξ_2 are the higher-order interfacial anisotropy energy and VCMA coefficient, respectively. The value of these parameters will be estimated later in Chapter 4.

CHAPTER 3: Temperature dependence of the VCMA effect

3.1 Motivation

The magnetic anisotropy in ferromagnetic materials has been shown to have a strong dependence on temperature in previous theoretical and experimental works [154]. In particular, Callen and Callen's theory [155] predicts that uniaxial anisotropies, such as the perpendicular magnetic anisotropy (PMA) in the MgO|CoFeB interface discussed in Chapters 1 and 2, decrease with temperature as $M_s^3(T)$, while cubic (hydrostatic) anisotropies decrease up to $M_s^{10}(T)$, where $M_s(T)$ is the temperature-dependent saturation magnetization. On the other hand, the temperature dependence of the VCMA effect has not been studied yet either theoretically or experimentally up to this work. Therefore, quantifying the temperature dependence of both PMA and VCMA is an important requirement for the design of emerging nanoscale memory and logic devices that exploit such effects. Beyond practical considerations, the study of the temperature dependence of the PMA and VCMA effects is also of interest as it may contribute to a better understanding of the underlying physics behind both of these phenomena.

In this chapter, we study experimentally the temperature dependence of the interfacial PMA and the VCMA in nanoscale MTJ devices based on MgO|CoFeB|Ta material stacks. In section 3.2, we demonstrate that the temperature dependence of PMA and VCMA both follow power laws of $M_s(T)$, but with different exponents for the two quantities, where the strength of the VCMA effect is shown to decrease at a faster rate as a function of temperature compared to PMA. Additionally, the VCMA effect is observed to remain linear (i.e., the PMA varies linearly with the applied electric field) across the considered temperature range for the experiments (100 K to 400 K). The different power law exponents for the two quantities under study may indicate

that only some of the mechanisms involved in the PMA of these structures are sensitive to electric fields, hence also contributing to the VCMA effect, as will be discussed in the analysis of the experimental results in section 3.3.

3.2 Experimental methods and results

3.2.1 Methods

For this study, a multilayer stack with the composition of substrate | bottom electrode | PtMn (20) | $Co_{70}Fe_{30}$ (2.3) | Ru (0.85) | $Co_{60}Fe_{20}B_{20}$ (3) [fixed layer] | MgO (1.3) | $Co_{20}Fe_{60}B_{20}$ (1.5) [free layer] | Ta (5) | top electrode (thickness in nm) was deposited in a Singulus TIMARIS physical vapor deposition (PVD) system, and subsequently annealed at 300 °C for two hours in an in-plane magnetic field of 1 T. The stack was then patterned into 125 nm × 50 nm elliptical nanopillars for electrical measurements (see Fig. 3.1) using electron-beam lithography and ion milling techniques. The MgO tunneling barrier was designed to be thick enough (resistance-area (RA) product ~750 Ω-μm^2) to make current-induced spin-torque effects negligible. Also, the thicknesses in the $Co_{70}Fe_{30}$|Ru|$Co_{60}Fe_{20}B_{20}$ synthetic antiferromagnet (SAF) were tuned to cancel the offset field from the SAF into the free layer, while the PtMn provides an exchange bias strong enough to make the fixed layer insensitive to in-plane (H_x) magnetic fields in the range of study (± 2 kOe). Finally, the thickness of the $Co_{20}Fe_{60}B_{20}$ free layer was chosen such that the stable magnetization state of the free layer is in the perpendicular (z) direction.

Fig. 3.2(a) shows resistance (R) versus in-plane magnetic field (H_x) curves measured at three different temperatures. The hard-axis-like curves confirm that the free layer has a stable perpendicular magnetization, while the small size of the nanopillars ensures a largely single-

domain rotation of the magnetization with in-plane fields. As previously reported for MTJ devices [26], the resistance in the parallel direction (R_P) has a weak temperature dependence since the process is related to direct tunneling, meanwhile the resistance in the anti-parallel direction (R_{AP}) increases as temperature decreases due to the reduction of spin-flip scattering that reduces the effective polarization (hence, the TMR ratio). Finally, it is clear that larger fields are required to saturate the magnetization as the temperature decreases, a clear indication of an increase of the perpendicular anisotropy.

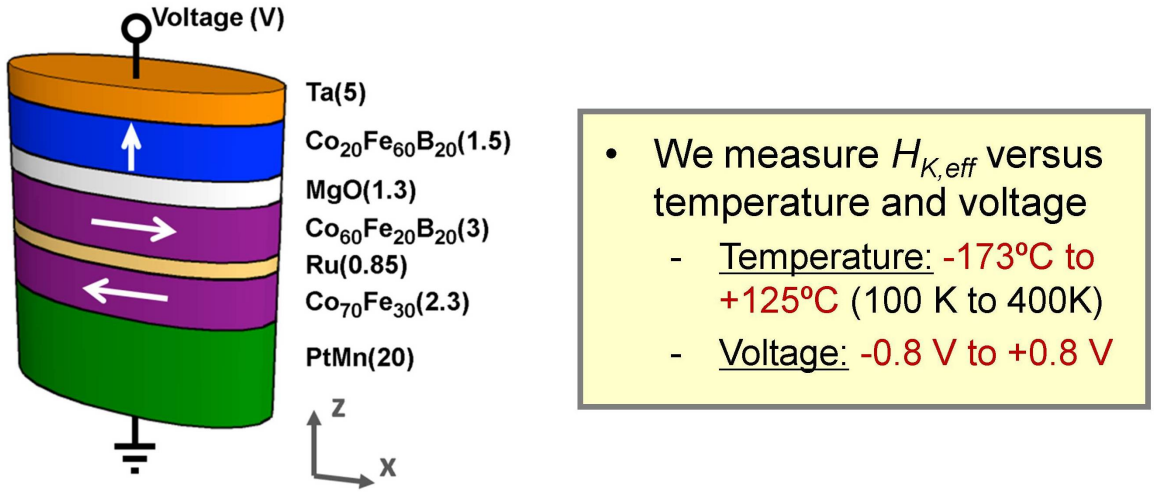

Fig. 3.1 The devices used in this work were 125 nm × 50 nm elliptical magnetic tunnel junctions, where the Fe-rich CoFeB free layer has a perpendicular easy-axis. The MgO thickness was designed to be thick enough to make current-induced torques negligible, while the synthetic antiferromagnet was designed to cancel stray fields into the free layer. In order to measure the temperature dependence of the interfacial anisotropy and the VCMA coefficient, the effective anisotropy field $H_{k,eff}$ is measured versus temperature (100 K to 400 K) and voltage (−0.8 V to +0.8 V).

In order to quantify the dependence of the effective anisotropy field $H_{k,eff}(T,V)$ (i.e., the field required to saturate the perpendicular free layer into the in-plane direction) on temperature T and, due to the VCMA effect, on voltage V applied to the MTJ, the measured resistance values are first translated into conductance $G = 1/R$ plots. Considering the linear relationship

between MTJ conductance and the component of the free layer magnetization along the direction of the fixed layer in MJTs [109, 156] (i.e., $m_x = M_x / M_s$ in our case), the conductance curves are then translated into m_x-H_x curves. Fig. 3.2(b) shows the resulting m_x-H_x curves for 3 different temperatures, when only a very small voltage of 10 mV is applied to the MTJ in order to measure the resistance of the device. The state $m_x = +1$ ($m_x = -1$) is proportional to the conductance in the parallel state G_P (conductance in the anti-parallel state G_{AP}), corresponding to the free layer aligning parallel (anti-parallel) to the fixed layer. It can be clearly observed that the effective anisotropy field is a strong function of temperature, i.e., $H_{k,eff}(T, V = 0)$ decreases with increasing temperatures. The effect of the VCMA effect can be also observed in the m_x-H_x curves of Fig. 3.2(d), showing curves for three different voltages at a fixed temperature. These curves are used to estimate $H_{k,eff}(T, V)$ at different temperatures T. In both cases, $H_{k,eff}$ can be calculated from the highlighted area in Fig. 3.2(b) and (d), specifically [109]

$$H_{k,eff}(T,V) = 2\int_0^1 H_x(m_x)\,dm_x \tag{3.1}$$

For this study, $H_{k,eff}(T, V)$ was measured for temperatures from 100 to 400 K in steps of 20 K, and for each temperature, the voltage dependence was measured for voltages between −0.8 and +0.8 V in steps of 0.2 V.

In order to validate the approach to extract $H_{k,eff}$ starting from the R-H_x curves, micromagnetic simulations where utilized to compare the rotation of the magnetization in simulations versus the extracted m_x-H_x curves from experimental data. As observed in Fig. 3.2(c), a good match is obtained, with an error smaller than 1% in the estimation of interfacial anisotropy between simulations and experiments (the extraction of the interfacial anisotropy from experiments is described in section 3.2.3). For the micromagnetic simulations, the values of

M_s at different temperatures were extracted from the data presented in section 3.2.2, while the exchange stiffness A was used as a fitting parameter. It is worth noting that no second order anisotropy was required in principle to find a good fit to the data on the devices used in this chapter. In Chapter 4, a more sensitive characterization method for the anisotropies (i.e., ferromagnetic resonance) will be used to accurately characterize the second order anisotropy and study conditions where such higher order term needs to be considered.

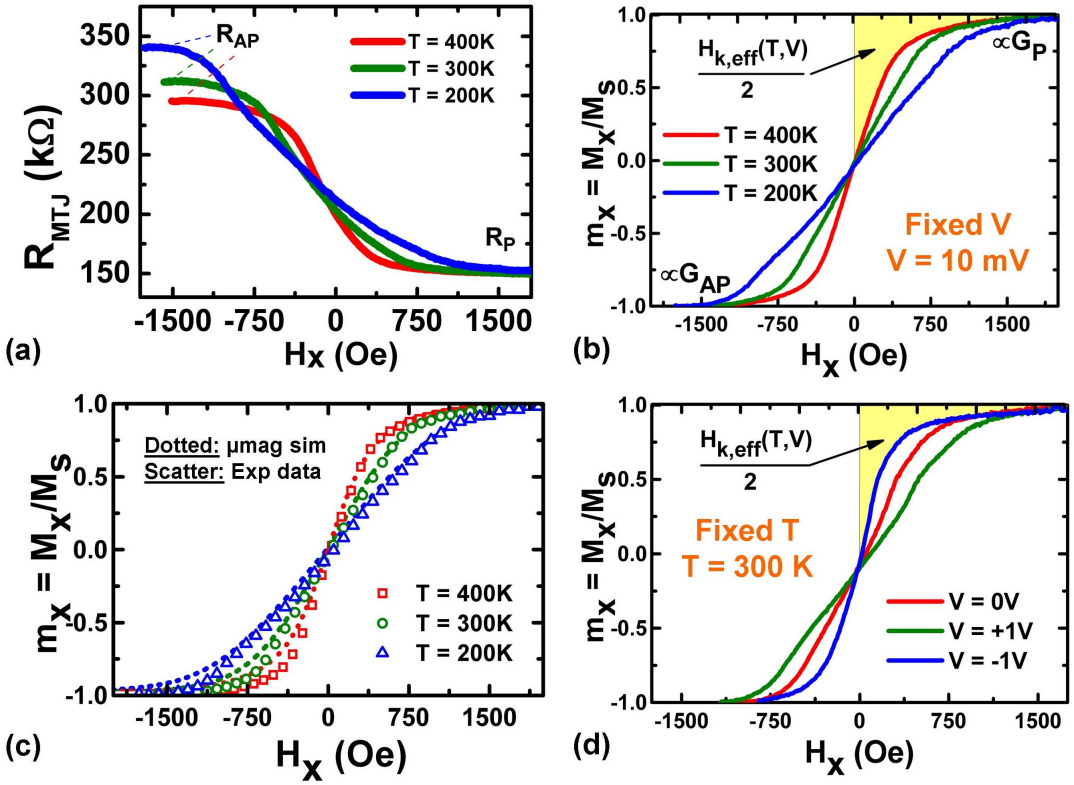

Fig. 3.2 (a) Resistance (R) versus in-plane magnetic field (H_x) at differente temperatures. As expected, the resistance in the parallel state (R_P) weakly depends on temperature, opposite to the resistance in the anti-parallel state (R_{AP}). (b) The R-H_x are translated into magnetization in the x-direction (m_x) versus H_x curves. The effective anisotropy field is extracted from the highligthed area, which is a clear function of the temperature. (c) Micromagnetic simulations (dotted) are found to be in good agreement with the m_x-H_x curves extracted from experiemental data (scatter plot). (d) In order to quantify the VCMA effect, and its temperature dependence, $H_{k,eff}$ is extracted as a function of both temperature and bias voltage, by utilizing equation (3.1).

3.2.2 Temperature dependence of the magnetization saturation

The dependence of the saturation magnetization on temperature $M_s(T)$ was independently measured in a 5 mm × 5 mm sample with a composition of substrate | MgO (2) | $Co_{20}Fe_{60}B_{20}$ (1.5) | Ta (5) | cap, which corresponds to the structure of the free layer in the nanopillar devices. The sample was annealed in the same conditions as the stacks used to fabricate the MTJs. Fig. 3.3(a) shows measurements of the magnetic moment M as a function of out-of-plane magnetic field (H_z) for four different temperatures using a superconducting quantum interference device (SQUID) magnetometer, confirming that the $Co_{20}Fe_{60}B_{20}$ layer has a perpendicular easy-axis over a wide range of temperatures for a thickness of $t_{\mathrm{CoFeB}} = 1.5$ nm. A strong dependence on temperature of the coercivity (dependent also on the perpendicular anisotropy) is observed, where the coercivity decreases from ~250 Oe to ~15 Oe when increasing the temperature from 10 to 300 K. At the same time, a weaker dependence of the saturation magnetization M_s on temperature T is measured. Fig. 3.3(b) shows the extracted data for M_s versus T in the range from 10 K to 400 K. The data is found to fit well to Bloch's law [157]

$$M_s(T) = M_s(0)\left(1 - \left(\frac{T}{T^*}\right)^{3/2}\right) \tag{3.2}$$

due to the large Curie temperature T_C of CoFe(B) compared to the range of temperatures under consideration. From the fit, we estimate that $T^* = 1120$ K, while a value of $M_s(0) = 1457$ emu/cm^3 is obtained for the spontaneous magnetization at absolute zero.

3.2.3 Temperature dependence of the interfacial anisotropy

We first quantify the dependence of the interfacial PMA energy S_i on temperature at equilibrium, i.e., only applying a very small voltage (10 mV) to read out the MTJ resistance. The

inset in Fig. 3.4 shows the extracted values for the effective anisotropy field at equilibrium $H_{k,eff}(T,V=0)$, where we observed a decrease in $H_{k,eff}$ from ~1610 Oe to ~720 Oe when increasing the temperature from 100 to 400 K. S_i can be directly related to the effective perpendicular anisotropy K_{eff}, which is proportional to $H_{k,eff}$. Specifically, from equations (2.7) and (2.11)

$$K_{eff}(T,V)=\frac{M_s(T)H_{k,eff}(T,V)}{2}=\frac{S_i(T,V)}{t_{\mathrm{CoFeB}}}-2\pi(N_z-N_x)M_s^2(T) \tag{3.3}$$

where the first term on the right accounts for the PMA, while the second term corresponds to the demagnetization energy. The geometrical demagnetization factors in the z and x directions can be estimated to be $N_z=0.9343$ and $N_x=0.0150$, respectively, by using the elliptical cylinder approximation [136].

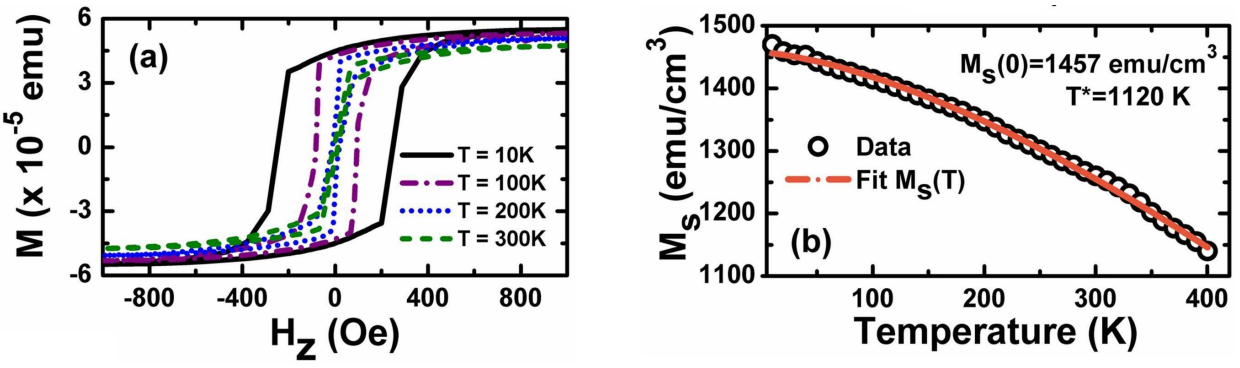

Fig. 3.3 (a) SQUID measurements of the magnetization M as a function of the perpendicular magnetic field H_z. The magnetization is observed to have a perpendicular easy-axis for the whole temperature range under study in the experiments. While a weak dependence of the saturation magnetization M_s on temperature T is measured, the strong dependence of the coercivity on temperature is the evidence for the strong dependence of the PMA on temperature. (b) The extracted dependence of M_s as a function of temperature is found to fit well to Bloch's law with fitting parameters $T^*=1120\,\mathrm{K}$ and $M_s(0)=1457$ emu/cm^3.

Using the extracted values for the $H_{k,eff}$, as well as the measured dependence of M_s on temperature T, equation (3.3) is utilized to extract the values for $S_i(T, V=0)$, which are shown in Fig. 3.4. We obtain a value of 1.45 erg/cm^2 = 1.45 mJ/m^2 for the PMA at room temperature ($T = 300$ K), in good agreement with previous reports for the MgO|$Co_{20}Fe_{60}B_{20}$|Ta system [61, 75]. The dependence of S_i on temperature is found to fit well to a power law of $M_s(T)$, i.e.

$$S_i(T) = S_i(0)\left(\frac{M_s(T)}{M_s(0)}\right)^{\gamma} \qquad \gamma = 2.18 \pm 0.04 \tag{3.4}$$

where the PMA at zero temperature is $S_i(0) = 2.02$ erg/cm^2. It is worth noting that a power law for $S_i(T)$ with an exponent $\gamma = 2.3 \pm 0.22$ was also found in the 5 mm × 5 mm sample used to extract $M_s(T)$, consistent within experimental error with the result obtained from the MTJ stack.

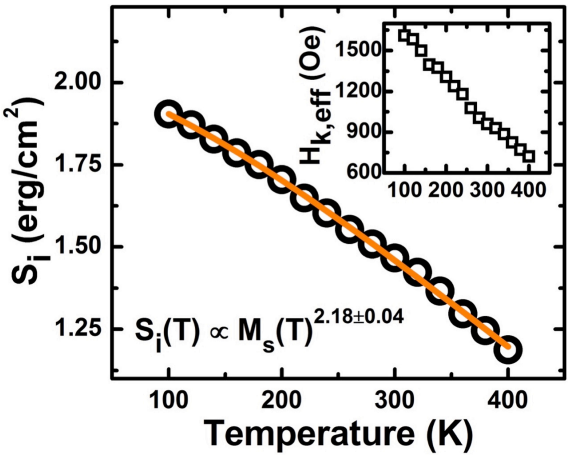

Fig. 3.4 Dependence of the effective anisotropy field $H_{k,eff}$ and the interfacial anisotropy energy S_i on temperature. The inset shows the extracted dependence of the effective anisotropy field $H_{k,eff}$ (i.e., the field required to saturate the perpendicular free layer into the in-plane direction) as a function of temperature at zero bias voltage. Using the extracted values for $H_{k,eff}$, the interface anisotropy is calculated using equation (3.3). The temperature dependence is found to fit well to a power law of $M_s(T)$ with an abnormal power law exponent $\gamma = 2.18 \pm 0.04$. The power law exponent combines contributions from the MgO|CoFeB and CoFeB|Ta interfaces.

3.2.4 Temperature dependence of the VCMA coefficient

Next we quantify the temperature dependence of the VCMA effect, in particular, by looking at the temperature dependence of the VCMA coefficient ξ, which describes the change of interfacial anisotropy energy per unit electric field, i.e., $\xi = \Delta S_i / (\Delta V / d_{\mathrm{MgO}})$ as defined previously in Chapter 2 (see equations (2.9) and (2.10)), where d_{MgO} is the thickness of the MgO insulating layer. Fig. 3.5(a) shows the change of the effective anisotropy field $\Delta H_{k,eff}$ as a function of the voltage V for four different temperatures between 100 K and 380 K, where $\Delta H_{k,eff} = H_{k,eff}(V) - H_{k,eff}(V=0)$. Similar to previous studies at room temperature for the MgO|CoFeB|Ta system [109, 124], our results show a linear dependence of $\Delta H_{k,eff}$ with voltage, where a positive voltage (more precisely, the depletion of electrons from the CoFeB|MgO interface) increases the effective perpendicular anisotropy. More importantly, we observe that the linearity of the VCMA effect is maintained over the wide temperature range under study; however, the relative change of the effective field per unit voltage $\Delta H_{k,eff}(T) / \Delta V$ (i.e., the slope of the $\Delta H_{k,eff}$ versus V curves, in units of Oe/V) is observed to decrease as the temperature increases. The inset in Fig. 3.5(b) shows the extracted values for $\Delta H_{k,eff} / \Delta V$ as a function of temperature during the experiment. Consequently, the temperature-dependent VCMA coefficient is calculated as $\xi(T) = M_s(T)\left(\Delta H_{k,eff}(T) / \Delta V\right) d_{\mathrm{MgO}} t_{\mathrm{CoFeB}} / 2$, where the computed values are plotted in Fig. 3.5(b). The VCMA coefficient at room temperature ($T = 300$ K) is found to be 3.1 × 10^{-9} erg/V-cm = 31 fJ/V-m, in good agreement to our previous work [109], and ξ is observed to decrease from ~46 to ~25 fJ/V-m when the temperature is increased from 100 to 400 K. Further, the temperature dependence of the VCMA coefficient is also found to fit well to a power law of $M_s(T)$, but notably with a different exponent compared to $S_i(T)$, i.e.,

$$\xi(T) = \xi(0)\left(\frac{M_s(T)}{M_s(0)}\right)^{\gamma'} \qquad \gamma' = 2.83 \pm 0.2 \tag{3.5}$$

with $\xi(0) = 48.9$ fJ/V-m as the VCMA coefficient at zero temperature.

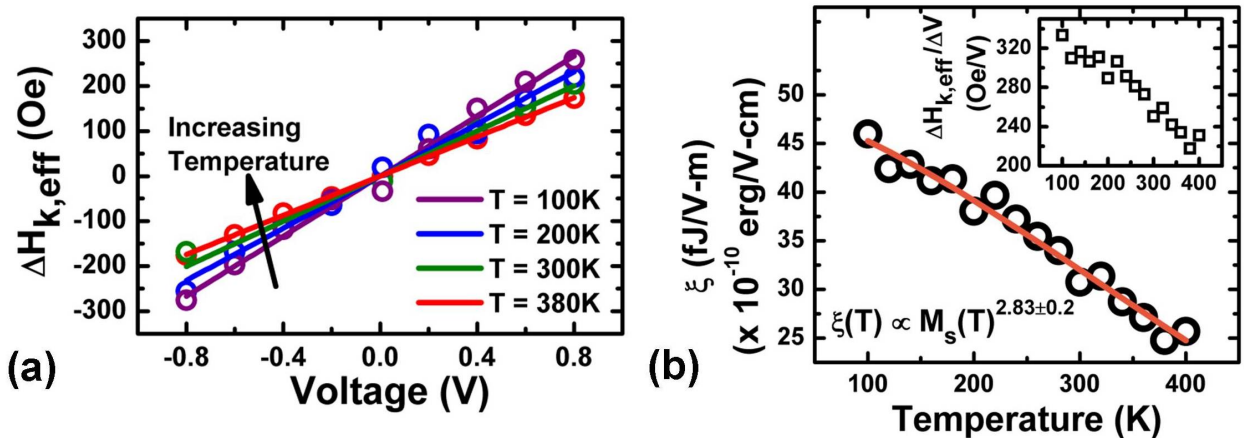

Fig. 3.5 Change of the effective anisotropy field $\Delta H_{k,eff} = H_{k,eff}(V) - H_{k,eff}(V=0)$ as a function of voltage for different temperatures. The VCMA effect is observed to remain linear over the temperature range of study, but the change of the anisotropy field per unit voltage $\Delta H_{k,eff} / \Delta V$ (the fitted slopes, in Oe/V) is reduced when temperature increases. (b) The inset shows the extracted values of $\Delta H_{k,eff} / \Delta V$ as a function of temperature. By using these values, the VCMA coefficient ξ (i.e., the change of interface anisotropy per unit electric field) is calculated and also found to fit well to a power law of $M_s(T)$, but with an exponent $\gamma' = 2.83 \pm 0.2$ that is closer to the Callen-Callen law [155].

3.3 Analysis of the experimental results

Our results indicate that, while both $S_i(T)$ and $\xi(T)$ follow power laws of $M_s(T)$, they are described by different exponents, where the exponent for the VCMA coefficient $\xi(T)$ (i.e., $\gamma' = 2.83 \pm 0.2$) is found to be close to the Callen-Callen $M_s^3(T)$ law [155] at small reduced temperatures T / T_C (a condition met by the temperature range considered in this study), while an abnormal exponent $\gamma = 2.18 \pm 0.04$ describes the temperature dependence of the interfacial

perpendicular anisotropy $S_i(T)$. Although Callen-Callen's law has been found to be accurate in describing the temperature dependence of uniaxial anisotropies in simple ferromagnetic systems (for example, uncapped ultrathin Fe grown on a GaAs substrate, where a $M_s(T)^{2.9\pm0.2}$ dependence of the uniaxial anisotropy was measured experimentally [158]), deviations from such a power law have been previously reported for more complicated systems. In particular, this has been reported in the case of alloys, where the material is constructed by more than a single sublattice and/or where the exchange interaction is anisotropic [159, 160], as well as in cases where non-magnetic materials with large spin-orbit coupling are present which strongly contribute to the anisotropy, but do not have a pronounced effect over the other magnetization properties (e.g., the Curie temperature or the saturation magnetization) [161]. Both of these scenarios violate two basic assumptions of Callen-Callen's theory: First, single-ions with localized magnetic moments are considered as the origin of the magnetization in the material; and second, the anisotropy is affected by temperature by the same mechanisms as the magnetization (i.e., average deviations in the magnetic moments due to temperature fluctuations giving rise to a decrease in M_s). Hence, recent theoretical works have predicted a leading $M_s^2(T)$ dependence for the uniaxial anisotropy when considering two-ion localized or itinerant contributions, e.g., when magnetism is coming from electrons localized or "shared" in between two different type of ions in the lattice, different from the single-ion assumption in the Callen-Callen theory. The $M_s^2(T)$ dependence has also been predicted in the presence of high spin-orbit coupling materials that contribute to the PMA [159, 160, 162, 163]. The latter two scenarios give rise to contributions to the temperature dependence of the PMA that are mutually exclusive to those coming from the Callen-Callen-like behavior. A clear example of the interplay between different contributions has been observed in experiments performed on FePt [164, 165], where

the anisotropy shows a $M_s(T)^{2.1}$ dependence and such a power law exponent has been also reproduced via ab-initio calculations, indicating only a 10% contribution from the Callen-Callen-like behavior [166].

For the system in the current study, the measured PMA of the CoFeB free layer is an overall quantity that includes contributions from both the MgO|CoFeB and CoFeB|Ta interfaces, i.e., $S_i = S_{i,\mathrm{MgO|CoFeB}} + S_{i,\mathrm{CoFeB|Ta}}$. However, in principle only the MgO|CoFeB interface should be sensitive to the applied electric field, and therefore the VCMA coefficient is solely related to this interface, as illustrated in Fig. 3.6.

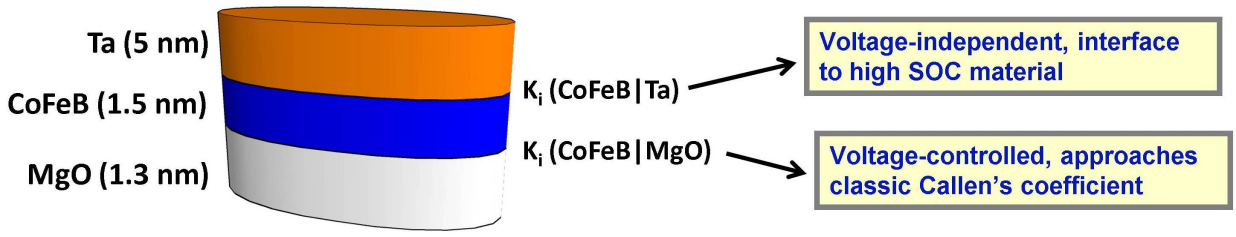

Fig. 3.6 Contribution to the interfacial anisotropy and VCMA from different interfaces. The measured perpendicular anisotropy in our devices is an overall quantity that includes contributions from the CoFeB|Ta and the CoFeB|MgO interfaces. However, in principle only the later should be sensitive to the applied electric fields, hence the temperature dependence of the VCMA should correspond mostly to the physics of such interface.

In the orbital picture discussed in section 2.3.1, the perpendicular anisotropy contribution from the MgO|CoFeB interface is attributed to the hybridization of Fe *d*-orbitals with O *p*-orbitals, whereas the VCMA effect is due to the modification of the occupancy between such hybridized orbitals. The electrons in the O-based hybridized orbitals tend to be localized due to the electronegativity and characteristics of the hybridized orbitals, hence resembling the assumptions of the Callen-Callen law. The latter might explain why the VCMA coefficient

power law exponent is dominated by a $M_s^3(T)$ contribution, as expected from the cited law. On the other hand, the non-integer power law exponent of $S_i(T)$ obtained in this study has a leading $M_s^2(T)$ contribution, which may be related to the influence of the high spin-orbit coupling (SOC) Tantalum via the Ta|CoFeB interface, and a smaller $M_s^3(T)$ contribution, which could be accounted for by the MgO|CoFeB interface. This would be in good agreement with the Rashba-based explanation for PMA and VCMA (see section 2.3.2), where the largest perpendicular anisotropy contribution is expected from the interface with the largest effective SOC (i.e., the Ta|CoFeB interface). As mentioned previously, a $M_s^2(T)$ temperature dependence is predicted in the presence of high SOC materials, and so it is reasonable to expect that the power law coefficient for S_i is dominated by what would be expected from the Ta|CoFeB interface. Further, in the Rashba picture, only the MgO|CoFeB interface is voltage-controlled; hence, the measured power law for the VCMA coefficient may be well attributed to such interface.

In terms of experiments, a previous work by Worledge, *et al.,* [77] demonstrated that the CoFeB|Ta interface plays a key role in the strong PMA of the MgO|CoFeB|Ta stack, albeit the exact role of Ta (and in general, of the high spin-orbit coupling metal interfacing with a ferromagnetic material showing a large PMA [129]) is more complicated, involving also its role both as a sink of boron atoms during post-deposition annealing, as well as promotion of (001) crystalline orientation in the resulting CoFe(B) layer. In addition, a recent work by Liu, *et al.,* [122] proposed that the Ta increases the effective spin-orbit coupling of the CoFe(B), and at the same time, the small electronegativity of Ta promotes the hybridization of Fe-O bonds, both of these effects resulting in a larger PMA. Nevertheless, a more detailed understanding of the exact contribution of each mechanism to explain the different power law exponents obtained in this work will require ab-initio calculations. Even in the Rashba picture, the complicated temperature

dependence of the parameters of the model presented in section 2.3.2 requires evaluation via first principle calculations.

Finally, in terms of device applications where the VCMA effect is used to switch MTJ devices, in section 2.4 it was derived that the critical switching voltage is given by $V_c = dkT\Delta(V=0)/\xi A$. Taking into account that the thermal stability factor is approximately proportional to the interfacial anisotropy energy, i.e., $\Delta(V=0) \propto S_i$ (see equation (2.11)), the critical voltage becomes proportional to the figure of merit between the interfacial anisotropy and the VCMA coefficient, in other words, $V_c \propto S_i(T)/\xi(T)$. Hence, to decrease the switching voltage, it is desired to have a small figure of merit $S_i(T)/\xi(T)$ while assuring non-volatility of the memory bit.

In the present study, we found that these two quantities are not proportional, but rather $\xi(T)$ decreases faster as a function of temperature compared to $S_i(T)$. Therefore, as the temperature increases, the figure of merit $S_i(T)/\xi(T)$ increases, hence, larger voltages will be needed to achieve the electric-field-driven switching for a constant value of the interfacial anisotropy (i.e. for a constant retention time when used as memory). In particular, we estimate that an increase of 10% in the switching voltage will be required to compensate for the increase in the $S_i(T)/\xi(T)$ figure of merit when increasing the temperature in between the typical limits of operation for a memory device (240 to 400K).

To summarize, the temperature dependence of the interfacial PMA and its sensitivity to electric fields in the MgO layer were measured over a wide range of temperatures for nanoscale MgO|CoFeB|Ta MTJ devices. It was demonstrated that the temperature dependencies of these quantities follow power laws of the saturation magnetization, but with different power law exponents. Our results support previous reports indicating that the high SOC metal seed/cap next

to the ferromagnetic layer plays a significant role in the strong PMA observed in systems such as the one studied in this work. Further, the different power law exponents for $S_i(T)$ and $\xi(T)$ may indicate that only certain contributions to the PMA are sensitive to electric fields via the VCMA effect, an effect which may have important implications for device applications.

CHAPTER 4: Higher order contributions to VCMA

4.1 Introduction and motivation

So far, we have mostly described the anisotropy energy and its modulation by voltages via the VCMA effect by only taking into account a $\sin^2\theta$ dependence of the energy, i.e., $E_{an} = K_{1,eff}\sin^2\theta$, where θ is the polar angle (as defined in the previous chapter and later in Fig. 4.4) and $K_{1,eff}$ is the effective anisotropy constant, which lumps together the demagnetization energy, the interfacial anisotropy contribution and the VCMA effect. This functional form describes a uniaxial anisotropy, where the sign of $K_{1,eff}$ determines the preferred axis for the magnetization, specifically an in-plane configuration if $K_{1,eff} < 0$ (minimum energy at $\theta = 90^\circ$ or $\theta = 270^\circ$), or a perpendicular axis if $K_{1,eff} > 0$ (minimum energy at $\theta = 0^\circ$ or $\theta = 180^\circ$).

However, the $\sin^2\theta$ dependency is just the lowest order contribution to the angular dependence of the anisotropy. In reality, the angular dependence of the anisotropy energy is far more complicated, and includes multiple higher order terms allowed by the specific symmetries of the system. For example, in a bulk system with magnetocrystalline anisotropy that has cubic symmetry, it can be mathematically demonstrated that the allowed terms for the anisotropy energy, up to second order, are [167]

$$E_{an,cub} = K_{1,cub}\sin^2\theta + \left[\sin^2\phi\cos^2\phi\left(K_{1,cub} + K_{2,cub}\right) - K_{1,cub}\right]\sin^4\theta - K_{2,cub}\sin^2\phi\cos^2\phi\sin^6\theta \quad (4.1)$$

where ϕ is the azimuthal angle, as defined later in Fig. 4.4, and $K_{1,cub}$ and $K_{2,cub}$ are the first and second order anisotropy constants, respectively. It can be clearly observed that, by including the second order in the expansion, the uniaxial part of the anisotropy (i.e., in the perpendicular

direction) is now given by $K_{1,cub}\sin^2\theta - K_{1,cub}\sin^4\theta$, whereas the new dependency on the azimuthal angle results in a non-uniaxial contribution, which can lead to a four-fold in-plane anisotropy proportional to $\sin^2\phi\cos^2\phi$. In other words, higher order contributions to anisotropy may lead to simultaneous perpendicular and in-plane anisotropies, and in the case of cubic systems, the in-plane component can be as large as the perpendicular one due to the $\left(K_{1,cub} + K_{2,cub}\right)$ prefactor in equation (4.1).

Similarly, for hexagonal systems, the anisotropy energy is given by [167]

$$E_{an,hex} = K_{1,hex}\sin^2\theta + K_{2,hex}\sin^4\theta + K_{3,hex}\sin^6\theta + K_{4,hex}\sin^6\theta\cos 6\phi \tag{4.2}$$

where the anisotropy remains uniaxial up to the $\sin^4\theta$ term and the $\sin^6\theta\cos 6\phi$ term can lead to an anisotropy with 6-fold symmetry in the in-plane hexagonal basal plane. It is worth noting that the most common thin-film ferromagnetic materials such as Fe, Co, Ni are isotropic in the plane of the film, hence typically the anisotropies are usually uniaxial and the experimental results can be well described by only considering up to the $\sin^4\theta$ term in equation (4.2) [21]. In consequence, it can be frequently found in the literature that the anisotropy energy is written as a function of the canonical energy constants $K^*_{1,hex}$ and $K^*_{2,hex}$, specifically, considering the energy up to the $\sin^4\theta$ term [168, 169]

$$E^*_{an,hex} = \left(K^*_{1,hex} + 2K^*_{2,hex}\right)\sin^2\theta - K^*_{2,hex}\sin^4\theta \tag{4.3}$$

Finally, for a tetragonal system, the anisotropy energy is given by [167]

$$E_{an,tetr} = K_{1,tetr}\sin^2\theta + K_{2,tetr}\sin^4\theta + K_{3,tetr}\sin^4\theta\cos 4\phi \tag{4.4}$$

where the $\cos 4\phi$ term denotes the 4-fold symmetry and appears in the $\sin^4\theta$ term of the expansion, where the last term in equation (4.4) is also typically not needed to explain the experimental data in regular thin-film ferromagnets [21].

In summary, it can be clearly observed that for the three most typical crystal structures in ferromagnetic materials, the anisotropy energy has a uniaxial dependence of the form

$$E_{an,u} = K_1 \sin^2\theta + K_2 \sin^4\theta \tag{4.5}$$

plus higher order terms which are uniaxial and non-uniaxial depending on the exact symmetries of the structure. As mentioned before, experimentally, it is typically found that to accurately describe uniaxial anisotropy energies of bulk ferromagnets, both K_1 and K_2 need to be considered, but no further terms are usually required for simple ferromagnets [167, 170]. Also, the constants K_1 and K_2 are usually treated as parameters to be experimentally extracted since they may lump different contributions to the anisotropy; for example, a typical cubic bcc system such as CoFe(B) may include small contributions from tetragonal structure (due to lattice distortion induced by the difference in lattice constants in CoFeB|MgO) or from Co clusters/islands with hexagonal symmetry. Further, important sources of effective higher-order anisotropies are the presence of non-collinear structures, such as the grains in polycrystalline films (e.g., CoFe(B) after annealing), or due to laterally inhomogeneous or rough films, resulting from steps, interdiffusion, island-type film growth, and other imperfections [171, 172]. All these practical considerations explain the need for considering higher order contributions when describing the anisotropy in real ferromagnetic systems.

Opposite to bulk anisotropies, which have been extensively studied in the literature, there are far less studies on the detailed description of the contribution of higher order terms into the interfacial perpendicular anisotropy in ultrathin films, and the topic is currently poorly understood both theoretically and in experiments [168]. Moreover, there currently few papers reporting on the higher order contribution to the interfacial perpendicular anisotropy in the

CoFeB|MgO interface [109, 173-175], the focus of this work, while this chapter is the first study of the higher order contribution to the VCMA effect in such system.

Due to the broken symmetry at the interface that causes the anisotropy (e.g., CoFeB|MgO), only lower order contributions are expected as compared to the symmetry analysis previously outlined for bulk anisotropies in infinite crystals [176]. Also, the interfacial anisotropy in CoFeB|MgO is a consequence of spin-orbit coupling of hybridized *d* orbitals, where such orbitals are described by spherical harmonics with $\ell = 2$, e.g., orbitals that have at most $\sin^2\theta$ or $\cos^2\theta$ angular dependencies. Finally, first-principles calculations on the perpendicular anisotropy in an unrelaxed Fe|MgO system by Yang, *et al.*, [118] show that the anisotropy energy only has $\sin^2\theta$ dependency, i.e., no second order anisotropy is observed in their calculations. Therefore, no higher order contributions are in principle theoretically expected for the perpendicular anisotropy in an ideal CoFeB|MgO structure. However, recent experiments hint that the second order anisotropy is indeed present in the system and plays a role in the magnetization dynamics, where the source of the higher order anisotropy remains to be determined, but it could be in principle related to roughness at the interface, or non-homogeneities of the orbital configuration that contribute to perpendicular anisotropy.

In particular, the experimental work by Zhu, *et al.*, [109] on a CoFeB|MgO-based MTJ demonstrates an abnormal dependence of the ferromagnetic resonance (FMR) on the applied field, which can be only reproduced by assuming a second order anisotropy around ten times smaller compared to the first order contribution. Further, a detailed study by Iihama, *et al.*, [173] on the angular dependence of the FMR also agrees on a ten times smaller second order anisotropy, and demonstrates the need to include such contribution to accurately characterize the experimental data. Furthermore, the presence of higher-order anisotropy contributions in

CoFeB|MgO has not only been hinted by sensitive FMR experiments, but also Kanai, *et al.*, [177] attribute the elongated astroid curves in their measurement on nanoscale perpendicular MTJ devices to the presence of the second order anisotropy.

In this chapter, we study the higher order anisotropy contributions to the perpendicular anisotropy in our nanoscale MTJ devices, but mainly measure for the first time the existence of a higher order contribution to the VCMA effect, which modulates the $\sin^4\theta$ anisotropy energy by the applied voltage. Due to the different angular dependence of the first and second order anisotropies, it is expected that each contribution will play a different role during the switching process of the MTJ device, or any other dynamic phenomena. Thus, as described in section 2.6, it is highly desired to capture the physics of the anisotropies in detail, including separating the voltage dependency of different contributions in order to construct, for example, accurate models to describe VCMA-driven MTJ dynamics during the design of a possible MeRAM memory bit.

4.2 VCMA-driven ferromagnetic resonance (FMR)

Ferromagnetic resonance (FMR) studies are typically used to accurately characterize the magnetic properties of magnetic films, including the extraction important parameter such as damping and inhomogeneous broadening due to impurities, g-factor, anisotropy constants and contributions, strength of STT, field-like torque or spin-Hall angle in spin-torque-FMR, and the magnitude of the VCMA effect in VCMA-driven FMR [21, 37, 110, 167, 169, 178, 179].

In the FMR technique, a microwave signal with frequencies close to the ferromagnetic resonance (typically on the GHz range for common ferromagnetic materials) is coupled to the material. By simultaneously tuning the frequency of the microwave signal and/or the applied external magnetic fields, the resonance frequency and the linewidth of the resonant peak are

studied as a function of the angle and strength of the applied magnetic field, hence allowing extracting the parameters previously mentioned.

In order to quantify the higher order contributions to the interfacial anisotropy energy and the VCMA effect in our nanoscale MTJ devices, the VCMA-driven FMR technique is used [110]. The circuit illustrated in Fig. 4.1 is utilized for this purpose. If we assume that the magnetization of the free layer has an angled configuration with respect to the fixed layer, i.e., the free layer magnetization is canted, the application of a voltage will increase or decrease the anisotropy due to the VCMA effect, leading to a change of the angle of the magnetization, hence a change of the resistance of the device due to the TMR effect. If the applied voltage is a small AC signal $V_{AC}(f)$, the magnetization will oscillate at the same frequency of the applied voltage in the linear regime, resulting in a MTJ resistance $R_{AC}(f)$ that also oscillates at the frequency of the applied voltage. The amplitude of such oscillation is expected to increase near resonance conditions for the free layer, which can be reached by either tuning the frequency of the microwave signal or the applied magnetic field.

If we take into account that there are simultaneously an AC current $I_{AC}(f)$ (due to the externally applied AC voltage) and an AC resistance $R_{AC}(f)$ (due to the oscillation of the magnetization, coupled to the input via VCMA) in the MTJ device, the product of the two oscillating signals at frequency f ($I_{AC}(f)\cdot R_{AC}(f)$) results in a DC voltage plus an AC voltage at $2f$. Hence, the MTJ acts as a rectifier for the input AC voltage, where the amplitude of the generated DC voltage is a function of the amplitude of $R_{AC}(f)$.

Additionally, in our circuit we modulate the input AC signal from the RF generator with a kHz square wave, which is locked to a lock-in amplifier in order to read-out the amplitude of the resulting modulated DC voltage (V_{mix} in Fig. 4.1, typically on the μV range). The modulation

serves a second purpose in our circuit: It decouples the generated rectified voltage from an additional DC voltage V_{DC} applied via a DC current source in order to avoid shunting of the lock-in amplifier (see Fig. 4.1). V_{DC} is used to modulate the anisotropy in our device via the VCMA effect; specifically, while the small RF voltage is used to drive the system into resonance using VCMA as a coupling mechanism, the modulation of the anisotropy of the free layer via VCMA is due to the additional external DC voltage V_{DC} applied to the device. In order to keep V_{DC} constant as the external magnetic field is swept, a Labview program is used to track the DC resistance of the device and tune the DC current source to keep the V_{DC} constant.

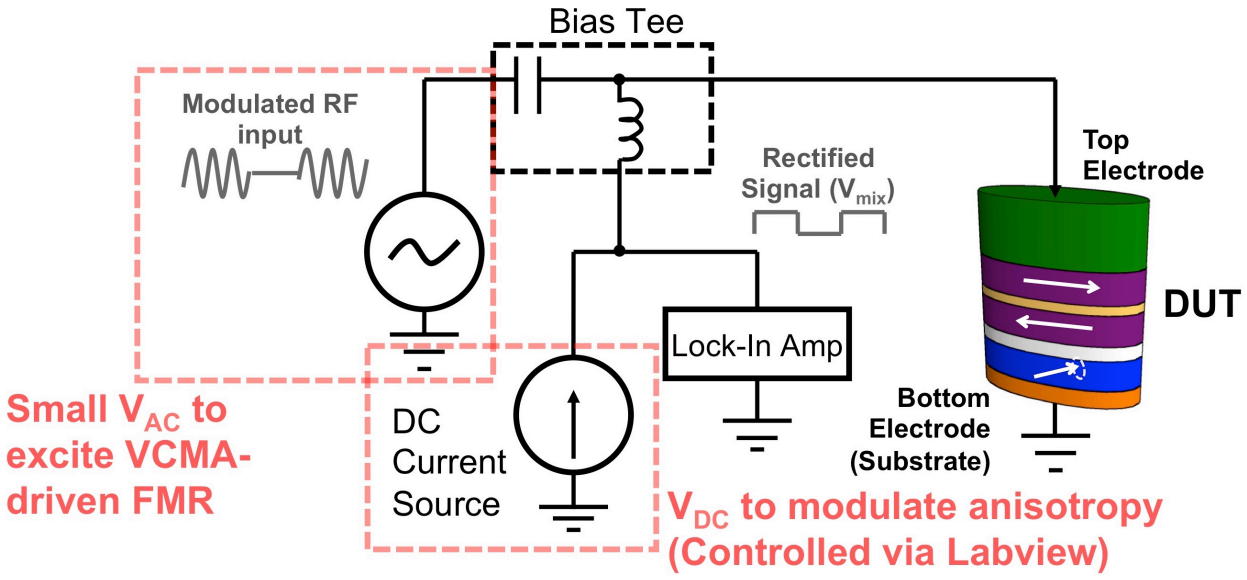

Fig. 4.1 Circuit diagram of the experimental set-up to measure VCMA-driven FMR dynamics in the device under test (DUT), specifically a nanoscale MTJ device. A small AC voltage V_{AC} is used to drive the DUT into ferromagnetic resonance, where the amplitude is small enough to keep the oscillation in the linear regime. The input is modulated by a slower (~ kHz) square wave in order to record the rectified voltage (V_{mix}) using a lock-in amplifier. Additionally, a DC voltage V_{DC} is used to modulate the anisotropy of the free layer of the MTJ device. This is performed by using a DC current source, avoiding shunting the lock-in amplifier, where the current source is controlled via Labview in order to keep the DC voltage at the device constant, independent of its resistance.

A typical example of the measured rectified signal V_{mix} as a function of the frequency of the input RF signal, for fixed values of the external magnetic field and V_{DC}, is shown on Fig. 4.2(a). It can be clearly observed that the measured signal has two contributions, i.e., a resonant feature plus a monotonic background. The background can be attributed to the frequency response of the parasitics in the circuit. In particular, Fig. 4.2(b) shows a circuit diagram of such parasitics, where R_{in} and L_{in} are the resistance and inductance of the transmission line connecting the RF probe to the device, and C_p and R_p are the shunt capacitance and resistance of the pads used to electrically contact the MTJ. As demonstrated in Fig. 4.2(a), the circuit model for the parasitics fits accurately into the background of the measured signal, allowing filtering it from the resonance feature.

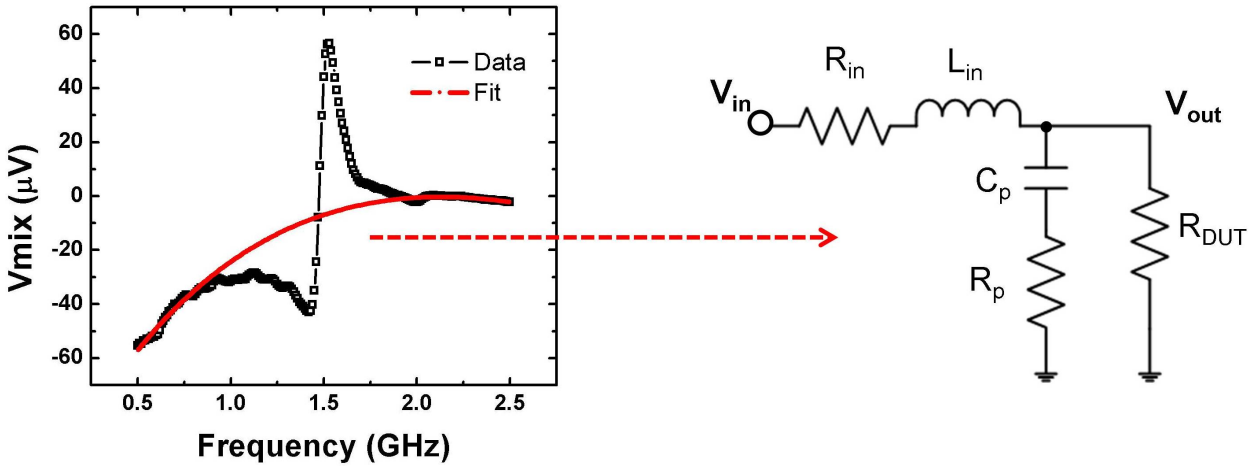

Fig. 4.2 The plot shows a typical measurement of the rectified voltage V_{mix} as a function of frequency for fixed values of the external magnetic field and DC voltage. The proposed parasitic circuit is used to filter the background. In the circuit, we consider the contributions from the transmission line to connect the device to the probing set-up (R_{in} and L_{in}) and the shunting resistance and capacitance (R_p and C_p) of the pads, both in parallel to the resistance of the DUT (R_{DUT}). The fit (in red) demonstrates that proposed circuit accurately describes the background, allowing filtering it from the resonance signal.

Fig. 4.3(a) shows the resulting signal after background subtraction, where the resonance feature can be clearly observed. As discussed by Zhu, *et al.*, [109] the FMR signal as a function of frequency corresponds to the summation of symmetric and antisymmetric Lorentzian contributions, specifically

$$V_{mix}(f) = \frac{V_s}{1+(f-f_0)^2/\sigma^2} + \frac{V_a(f-f_0)/\sigma}{1+(f-f_0)^2/\sigma^2} \tag{4.6}$$

where f_0 is the FMR resonance frequency, σ characterizes the linewidth of the resonance, meanwhile the ratio V_a / V_s denotes the proportion between the antisymmetric and symmetric contributions to the resonance signal, respectively. Equation (4.6) is used to fit the measured data, allowing to accurately extract the resonance frequency from the measured data, as illustrated in Fig. 4.3(a). The dependence of the resonance frequency on both the external magnetic field and the applied DC voltage will be later used to extract the higher order contributions to anisotropy and VCMA in our devices. The dependence of the rectified voltage on both frequency and the applied external magnetic field is illustrated in the contour plot of Fig. 4.3(b), which will be discussed later in section 4.4.

4.3 Device structure and equilibrium canted magnetization

The device structure utilized for this study is illustrated in Fig. 4.4. Continuous multilayer films with a composition of substrate | bottom electrode | Ta (5) | $Co_{20}Fe_{60}B_{20}$ [free layer] (t = 1.0 to 1.4 wedge) | MgO (1.3) | $Co_{60}Fe_{20}B_{20}$ [in-plane fixed layer] (2.7) / Ru (0.85) / $Co_{70}Fe_{30}$ (2.3) / PtMn (20) | top electrode (thickness in nm) were deposited in a Singulus TIMARIS physical vapor deposition (PVD) system, and subsequently annealed at 300 °C for 2.0 hours in an in-plane magnetic field of 1 T. The films were then patterned into elliptical nanopillars for electrical

measurements using electron-beam lithography and ion milling techniques. Similar to the devices in the previous chapter, the MgO tunneling barrier was designed to be thick enough (resistance-area (RA) product ~800 Ω-μm^2) to reduce current-induced spin-torque effects.

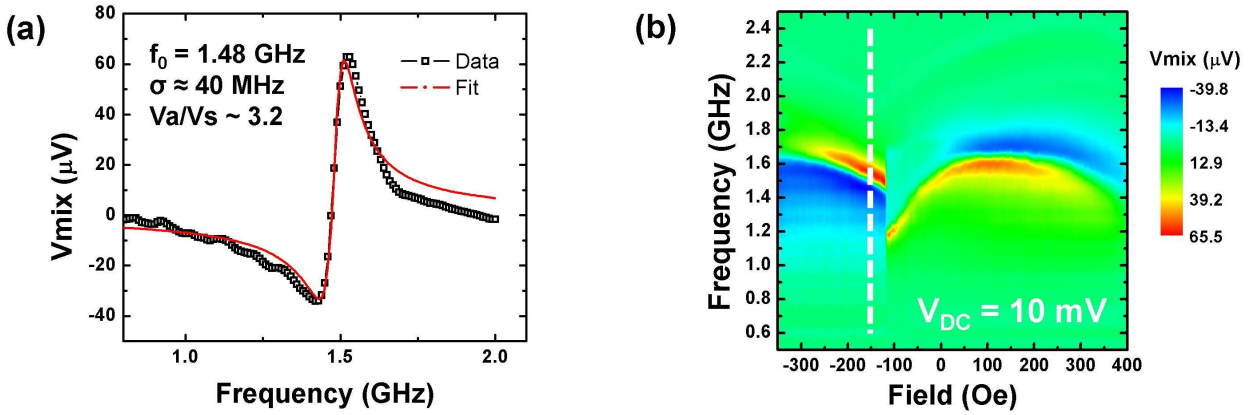

Fig. 4.3 (a) The resulting rectified signal V_{mix} after background subtraction can be well fitted into a summation from symmetric and antisymmetric lorentzian functions. In this example, the fit (in red) corresponds to a resonance frequency f_0 = 1.48 GHz, the linewidth σ is approximately 40 MHz, and the antisymmetric contributions is around 3 times larger compared to the symmetric component. (b) The signal V_{mix} is measured as a function of frequency and applied field, resulting in contour plots as the one in the figure for a fixed DC voltage of 10 mV. The dashed line corresponds to the cut shown in part (a).

In the samples for this study, the free layer was deposited as a wedge across the wafer, varying the thickness from 1.0 to 1.4 nm, where such thickness is used as a tuning parameter. As discussed in previous chapters, the first order anisotropy energy in the presence of an interfacial perpendicular anisotropy controlled via the VCMA effect can be written as (see equation (2.12))

$$K_{1,eff}(V) = \frac{S_{i,1}}{t_{\mathrm{CoFeB}}} - \xi_1 \frac{V}{d_{\mathrm{MgO}} t_{\mathrm{CoFeB}}} - 2\pi(N_z - N_x)M_s^2 \tag{4.7}$$

where N_z and N_x are the demagnetization factor in the z- and x-direction, respectively. Due to the small VCMA effect in Ta|CoFeB|MgO-based structures (see the discussion in Chapter 2), it is typically required to tune the thickness of the free layer near the cancellation point between the

interfacial anisotropy and the demagnetization energy (first and third terms in equation (4.7) respectively) in order to increase the relative tunability of the VCMA effect over the total energy of the system.

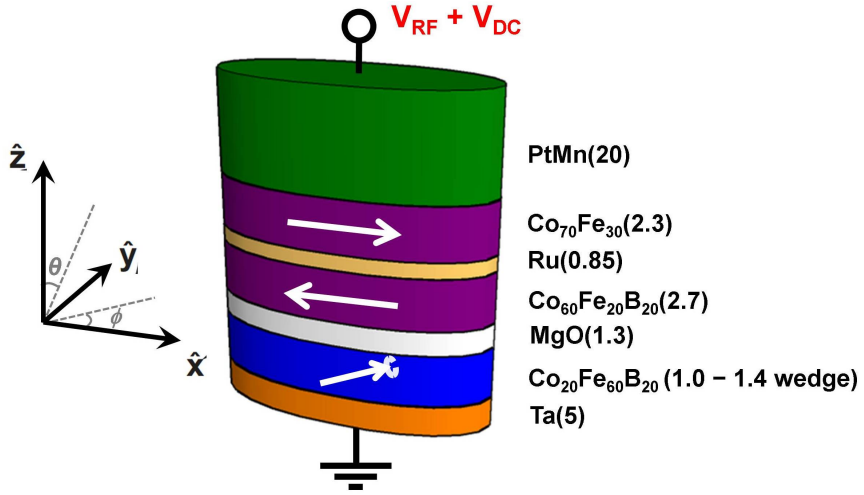

Fig. 4.4 Device structure for this study (thicknesses in nm). The films were sputter-deposited and patterned into nanoscale MTJ devices. The MgO thickness was designed to reduce any spin-torque effects, while the synthetic antiferromagnet lowers the stray field from the fixed layer acting in the free layer. The Fe-rich free layer was deposited as a wedge across the wafer in order to use the thickness of the free layer as a tuning parameter.

Specifically, the relative tunability

$$\frac{\Delta K_{1,eff}(V)}{K_{1,eff}(V=0)} = \frac{\xi V / d_{\mathrm{MgO}} t_{\mathrm{CoFeB}}}{S_{i,1} / t_{\mathrm{CoFeB}} - 2\pi(N_z - N_x) M_s^2} \tag{4.8}$$

is increased when the thickness of the free layer is chosen near the transition thickness, i.e., near the thickness where $S_{i,1} / t_{\mathrm{CoFeB}} - 2\pi(N_z - N_x) M_s^2 = 0$. If we consider now the total anisotropy energy E_{an}, including the second order contribution from equation (4.5)

$$E_{an} = K_{1,eff} \sin^2\theta + K_2 \sin^4\theta \tag{4.9}$$

we observe that having a small $K_{1,eff}$, due to the cancellation of interfacial anisotropy and demagnetization energy, the role of K_2 over the total energy of the system is increased, even if

the value of the second order anisotropy constant is one order of magnitude smaller than $S_{i,1}/t_{\mathrm{CoFeB}}$ (see section 4.1).

The increased role of K_2 near the transition thickness is demonstrated on the experimental measurements in Fig. 4.5, showing R-H_x loops on a set of three different 150 × 70 nm^2 nanoscale MTJ devices with three different thickness for the free layer. For the largest thickness (t = 1.33 nm), the interfacial contribution decreases and a large negative $K_{1,eff}$ results in an in-plane free layer, with an easy-axis R-H_x curve as demonstrated in Fig. 4.5. On the other hand, for the thinnest free layer (t = 1 nm), the energy is dominated by the interfacial perpendicular anisotropy (i.e., $K_{1,eff}$ becomes large and positive) and the magnetization becomes out-of-plane, in good agreement to the hard-axis R-H_x curve measured for such device.

If only the $\sin^2\theta$ term in equation (4.9) is considered, there is an abrupt transition between the in-plane and out-of-plane stable states. However, for the thickness value near transition (t = 1.13 nm), we observe experimentally an intermediate state for the magnetization, where the R-H_x shows both coercivity (like an easy-axis curve) but also smooth change of the resistance (i.e., smooth rotation of the magnetization, like a hard-axis curve). We attribute this intermediate state, whose R-H_x loop behaves like a combination of easy- and hard-axis, to canting of the free layer magnetization, which is a possible minimum energy state of equation (4.9) under the conditions $K_2 > 0$ and $-2K_2 < K_{1,eff} < 0$ (It can be easily demonstrated that the condition $\theta = 90^\circ, 270^\circ$ correspond to a maximum energy state under such conditions). It is clear that the smaller K_2, the smaller the range of thicknesses that can meet the conditions that lead to canting as an equilibrium state. Consequently, the observation of canted states may be limited by practical considerations for tuning the thickness of the free layer in samples with small K_2.

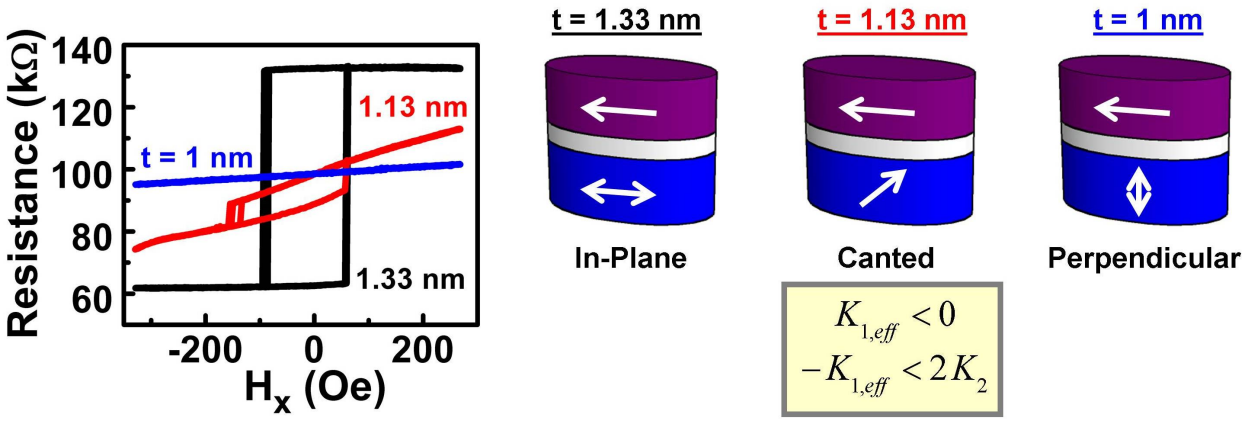

Fig. 4.5 Experimental resistance (R) vs in-plane magnetic field (H_x) curves measured over three 150 × 70 nm^2 elliptical nanoscale MTJ devices with different values for the thickness (t) of the free layer. For the thickest sample, the magnetization is in-plane, as demonstrated by the measured easy-axis curve. On the other hand, the thinnest sample shows a hard-axis R-H_x curve, indicating a perpendicular stable state for the magnetization. For a thickness value near transition, we observe an intermediate state, which can be attributed to canting of the magnetization under the conditions illustrated for $K_{1,eff}$ and K_2.

It is worth mentioning that the observation of canted states was systematic in all the samples close to the transition thickness for this study, and similar results were obtained in MTJ from 210 × 70 nm^2 down to 130 × 50 nm^2, our smallest patterned size. The experiment was repeated on a second batch with a similar stack structure, obtaining reproducible results. Also, it should be noted that due to the small energies near cancellation of $K_{1,eff}$, micromagnetic states could become energetically possible. However, due to the small size of the device, single-domain states are preferred over micromagnetic states such as domain walls. In order to verify this, micromagnetic simulations including K_2 were used to obtain the minimum energy equilibrium states, like the one shown in Fig. 4.6. It can be clearly observed that the magnetization is indeed mostly canted; however, a small C-shaped texture is observed, which may be explained due to pinning of the spins near the edges along the easy-axis of the pillar to minimize the magnetostatic energy. Finally, in order to directly verify the magnetization state of the MTJ,

XMCD or PEEM studies would be needed, but both of these techniques could not be used in our samples due to the thick layers on top of the free layer of our devices.

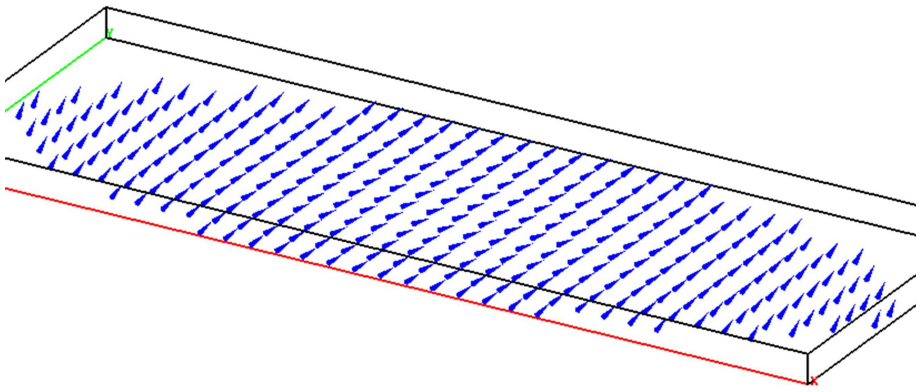

Fig. 4.6 Micromagnetic simulation of the equilibrium state of a nanoscale MTJ device with the parameters extracted experimentally, including the second order anisotropy energy K_2. It can be clearly observed that canting of the magnetization is indeed an equilibrium state for the magnetization in these conditions. However, a small texture is observed, mostly due to the pinning of the edges in the perpendicular direction due to magnetostatic energy.

The enhanced tunability via VCMA effect of samples near transition thickness is demonstrated in the R-H loops for in-plane and perpendicular magnetic fields illustrated on Fig. 4.7 for a 170 × 60 nm^2 device. Note that there is coercivity in both the in-plane and perpendicular directions, signature of a canted magnetization. Further, both coercivities can be tuned on ~150 Oe on average by changing the voltage from ~ −1 V to ~ +1V. Interestingly, both coercivities close with positive voltages, an interesting observation that will be later reproduced in section 4.6 by the extracted contributions from second order anisotropy and VCMA in our samples.

4.4 Dependence of the FMR frequency on applied voltage and field

In order to extract the higher order contribution to the interfacial anisotropy energy and the VCMA effect, the samples with canted magnetization states described in the previous section

are used due to the enhanced role of K_2 in the energetics of the system. Also, the presence of a canted magnetization at equilibrium allows performing VCMA-driven FMR experiments with in-plane magnetic fields, instead of using angled fields to induce such canting for the magnetization. Note that canting is required to create a change in the magnetization angle (hence, of the resistance of the MTJ) as a function of the applied AC voltage that drives the magnetization into resonance due to the VCMA effect (see the discussion in section 4.2).

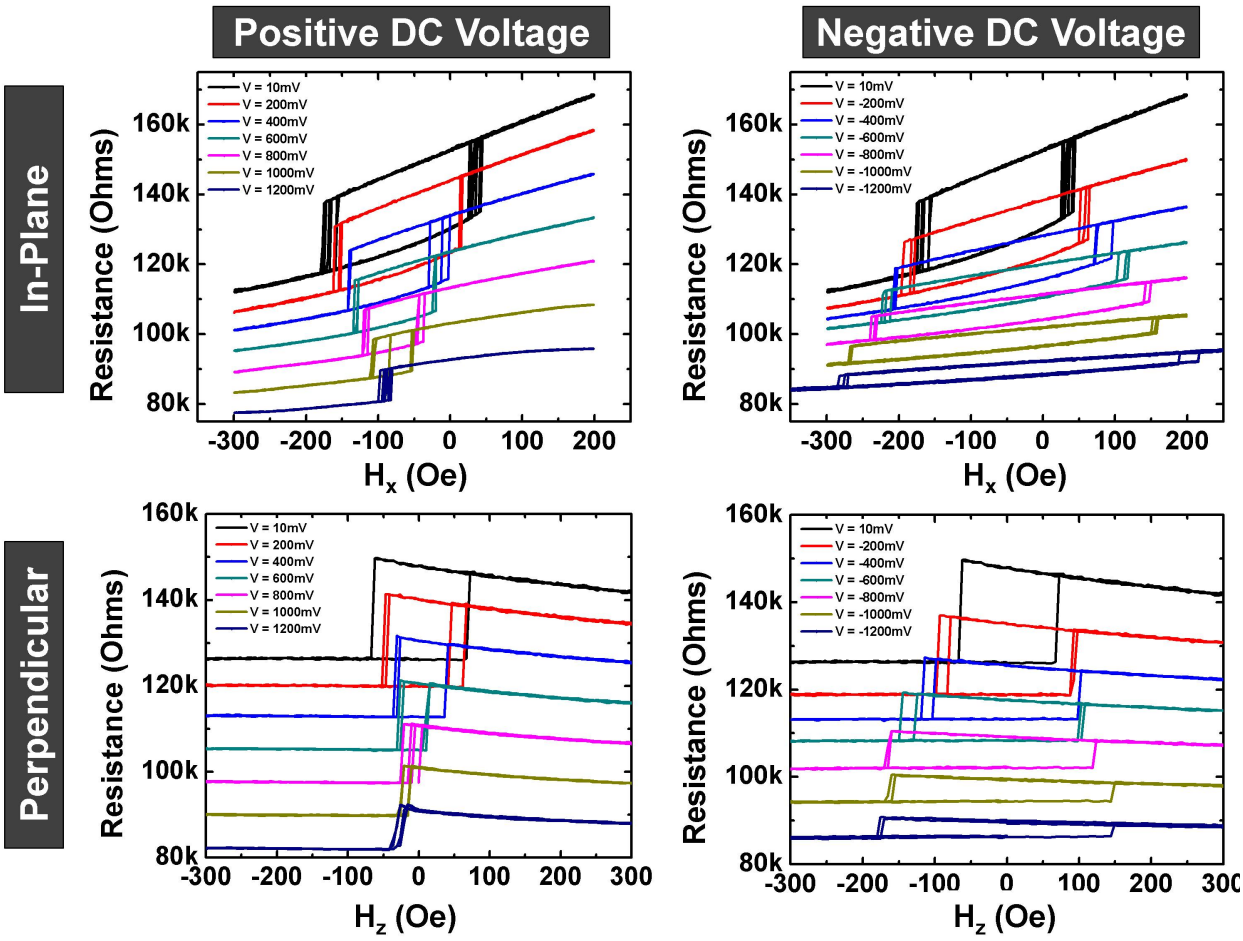

Fig. 4.7 Resistance versus in-plane (H_x) and perpendicular (H_z) applied magnetic field as a function of DC voltages from −1.2 V to +1.2 V. We observe coercivity in the in-plane and perpendicular directions, a signature of a canted magnetization state at equilibrium. Further, the coercivity in both directions decreases with the application of positive voltages, meanwhile it increases with the opposite DC polarity. The decrease of the resistance values with increasing applied voltage is due to the dependence of the MTJ resistance and the TMR effect on bias voltage [26].

We measure the VCMA-driven FMR signal (V_{mix}) from a 170 × 60 nm^2 device with thickness t = 1.13 nm as a function of the frequency of the RF input, the applied in-plane magnetic field and the DC voltage V_{DC} that modulates the anisotropy. Fig. 4.3(b) showed previously the typical contour plot obtained in the measurements, for example, for a fixed value of the DC voltage. Interestingly, we observe that the resonance moves from mostly antisymmetric near the peak FMR frequency to mainly symmetric at large magnetic fields, demonstrating that the contributions from symmetric and antisymmetric Lorentzians strongly depend on the angle of the magnetization. Further, by fitting the resonant curves obtained for different in-plane magnetic fields and DC voltages to equation (4.6), it possible to extract the dependence of the FMR frequency on these two variables. Fig. 4.8(a) shows the dependence of the FMR frequency (extracted from fitting the experimental data as in Fig. 4.3(a)) on the in-plane magnetic field for a fixed value of the DC voltage (V_{DC} = 10 mV). When sweeping the magnetic field in two different directions, hysteresis on the FMR frequency is observed, in good agreement to the R-H loops on Fig. 4.7, meanwhile the frequencies are approximately equal outside of the hysteretic range. Notice that there is a small asymmetry in the maximum resonance frequencies for the two sweeping directions. This may be attributed to a possible breaking of the symmetry between the canted states due to a non-uniform stay field from the fixed layer, or due to a possible small misalignment of the field that sets the direction of the fixed layer during the annealing process. In fact, the small asymmetry in the frequency response can be correlated to the asymmetry in the perpendicular R-H loops in Fig. 4.7. Also, the curves for the different sweeping directions cross at a field different than zero, indicating that the synthetic antiferromagnet (SAF) in Fig. 4.4 does not fully cancel the stray field from the fixed layer acting on the free layer. Lastly, Fig. 4.8(b) shows the extracted FMR frequency for two different RF

input powers of −20 and −15 dBm. By changing the input power, we did not observe additional peaks and the resonant frequency remained identical, indicating that the input power used for the experiments keeps the FMR oscillation in the linear regime.

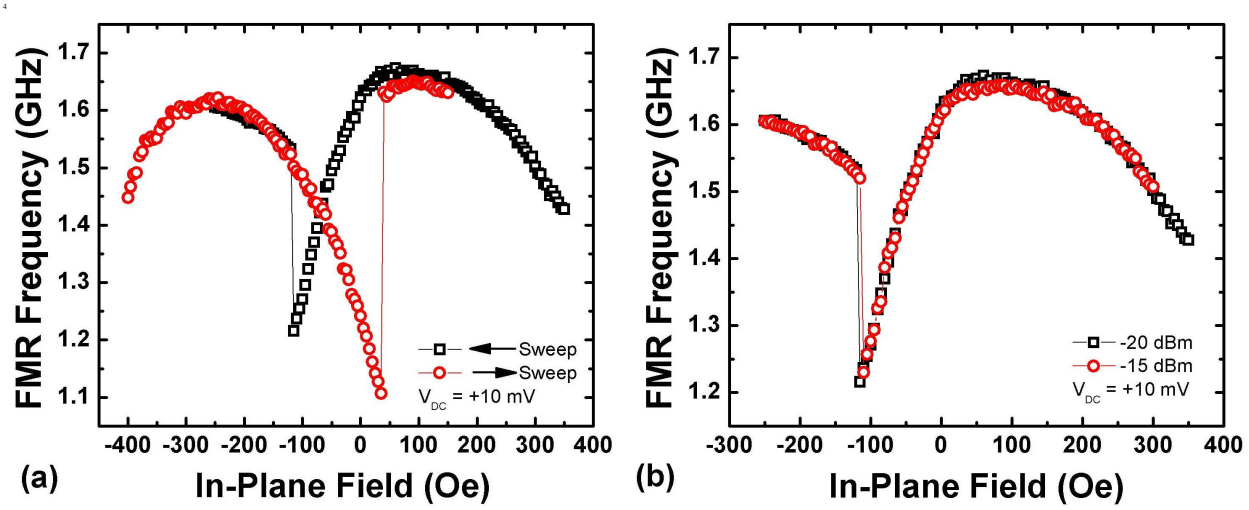

Fig. 4.8 (a) Extracted FMR frequency for two different sweeping directions of the in-plane magnetic field. The hysteresis in the FMR frequency is in good correspondence to the hysteresis observed in the R-H loops. Note that the curves cross at a value of the field different than zero, indicating the presence a stay field from the fixed layer into the free layer. The small asymmetry in the curves may be explained due to non-idealities of the samples. (b) Dependence of the FMR frequency on in-plane magnetic field for two different input RF power when sweeping the field from right (large positive fields) to left (large negative). The data illustrates that the power level utilized keeps the magnetization oscillation in the linear regime for the FMR since neither shifting of the resonance frequency by changing the input RF power nor additional resonance peaks are measured. Keeping the resonance in the linear regime is of importance in order to utilize the simplified mathematical description based on the linearization of the LLG equation, as described later in section 4.5.

Fig. 4.9(a) summarizes the obtained FMR experimental data by showing, after data processing, the dependence of the FMR frequency on the external applied in-plane magnetic field (in the *x*-direction) and on the applied DC voltage V_{DC} ranging from −0.5 V to +0.5 V. A non-monotonic dependence of the resonance frequency on field is observed for all the values of the V_{DC}, which cannot be explained by using the classical Kittel formulation [178] with only a

first order anisotropy constant. In fact, this behavior is expected since the effective magnetic field due to K_2 maximizes at an intermediate angled magnetization (see equation (2.24)). Also, the FMR frequency is observed to change from ~ 1 GHz to ~ 2 GHz when changing the DC voltage that modulates the anisotropy from +0.5 V to −0.5 V. The measured red shift of the resonance frequency with positive DC voltages is in good agreement to previous reports on the modulation of the FMR frequency via the VCMA effect [108, 110].

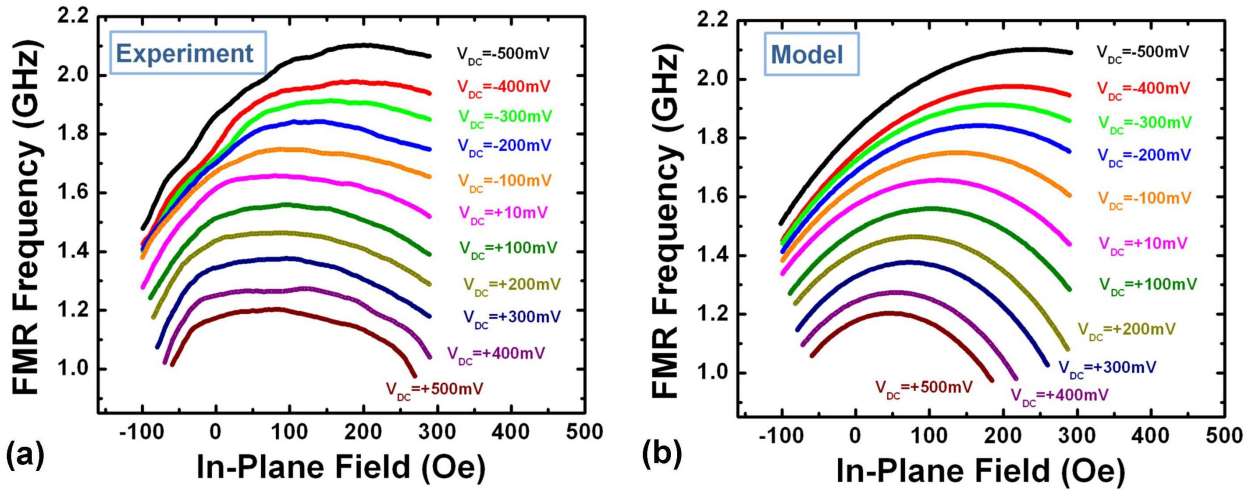

Fig. 4.9 (a) Extracted dependence of the FMR frequency on the applied in-plane magnetic field and on the DC voltage (V_{DC}). The non-monotonic dependence of the FMR frequency on field is a signature of the role of the second order anisotropy. The red shift with positive voltages is found to be in agreement to previous reports on the literature. (b) The theoretical model presented in section 4.5 is utilized to fit the obtained experimental data. The model qualitatively reproduces the experimental data by using the extracted parameters for the second order interfacial anisotropy and VCMA effect.

As mentioned previously, the non-monotonic dependence of the FMR frequency on in-plane field is a signature of the second order anisotropy. Therefore, a theoretical model that includes K_2 is needed in order to extract the second order contribution to anisotropy and VCMA from the experimental data in Fig. 4.9.

4.5 Macrospin model for FMR frequency with higher order contribution

In order to extract the anisotropy energy constants K_1 and K_2, and their respective sensitivities to the applied voltage via the VCMA effect, in this section we construct a macrospin model that relates the FMR frequency to the applied in-plane magnetic field which can be fitted to experimental data to calculate $K_1(V)$ and $K_2(V)$. As mentioned before, the voltage-dependent anisotropy energy, including the higher order contribution, is given by (see equation (4.9))

$$E_{an}(V) = K_{1,eff}(V)\sin^2\theta + K_2(V)\sin^4\theta \tag{4.10}$$

The energy can be also written as a function of the components of the magnetization vector $\vec{m} = \overrightarrow{M} / M_s = \left(m_x, m_y, m_z\right)$. Following the produce in section 2.6, in the coordinate system defined in Fig. 4.4, we have that $\sin^2\theta = 1-\cos^2\theta = 1-m_z^2$ and $\sin^4\theta = \left(1-m_z^2\right)^2$. Hence,

$$E_{an}(V) = K_{1,eff}(V)\left(1-m_z^2\right) + K_2(V)\left(1-m_z^2\right)^2 \tag{4.11}$$

In the presence of an external in-plane magnetic field in the x-direction H_x, the equilibrium condition for the magnetization will be given by the minimization of the total free energy F of the system, including contributions from demagnetization, anisotropy and Zeeman energies. Specifically,

$$F(V) = 2\pi M_s^2\left(N_x m_x^2 + N_y m_y^2 + N_z m_z^2\right) + K_1(V)\left(1-m_z^2\right) + K_2(V)\left(1-m_z^2\right)^2 - \overrightarrow{H}\cdot\overrightarrow{M} \tag{4.12}$$

where N_x, N_y, N_z are the geometrical demagnetization factors, $\overrightarrow{H} = H_x\hat{x}$ is the applied in-plane magnetic field, $K_1(V) = S_{i,1}(V)/t_{\mathrm{CoFeB}}$ is the first order anisotropy (different from $K_{1,eff}(V)$, which includes demagnetization), and $K_2(V) = S_{i,2}(V)/t_{\mathrm{CoFeB}}$ is the second order anisotropy. By dropping constant energy factors, we find that the free energy is

$$F = \frac{M_s^2}{2}\left[4\pi N_x m_x^2 + 4\pi N_y m_y^2 + \left(4\pi N_z - \widetilde{K}_1(V)\right)m_z^2 + \widetilde{K}_2(V)(1-m_z^2)^2\right] - H_x M_s m_x \quad (4.13)$$

where $\widetilde{K}_1(V) = 2K_1(V)/M_s^2$ and $\widetilde{K}_2(V) = 2K_2(V)/M_s^2$ are the reduced anisotropy constants. Hence, the equilibrium condition of the magnetization of the free layer $\vec{m}_{eq} = \left(m_{x,eq}, m_{y,eq}, m_{z,eq}\right)$ is obtained by minimizing equation (4.13), considering that, due to the shape anisotropy of our elliptical nanopillar samples, it can be assumed that $m_{y,eq} \approx 0$ (i.e., the equilibrium magnetization stays in the plane between the easy-axis of the pillar and the preferred perpendicular (z-) direction for the interfacial anisotropy), and therefore, $m_{z,eq}^2 \approx 1 - m_{x,eq}^2$.

Once the equilibrium condition for the magnetization is obtained, one can estimate the FMR frequency by linearizing LLG equation, introduced previously in section 2.6

$$\frac{d\vec{m}}{dt} = -\gamma'\left(\vec{m} \times \vec{H}_{eff}(V)\right) \quad (4.14)$$

and assuming a sinusoidal response of the magnetization to an AC input (the procedure is outlined in Ref. [167]). Note that only the precessional term is considered in this case since we are only interested in extracting the FMR frequency, meanwhile $\vec{H}_{eff}(V)$ lumps together all the contributions from the external magnetic field and the effective anisotropies, VCMA and demagnetization fields (see equation (2.20)). In order to facilitate the mathematical derivation of the FMR frequency, the coordinate system is rotated to the primed coordinate axes illustrated on Fig. 4.10(a), where the equilibrium condition for the magnetization lies along z' axis. In the primed coordinate system, the FMR frequency can be expressed as a function of the changes of the effective field $\vec{H}_{eff}(V)$ due to oscillation (precession) of the magnetization in the x'-y' plane, in particular

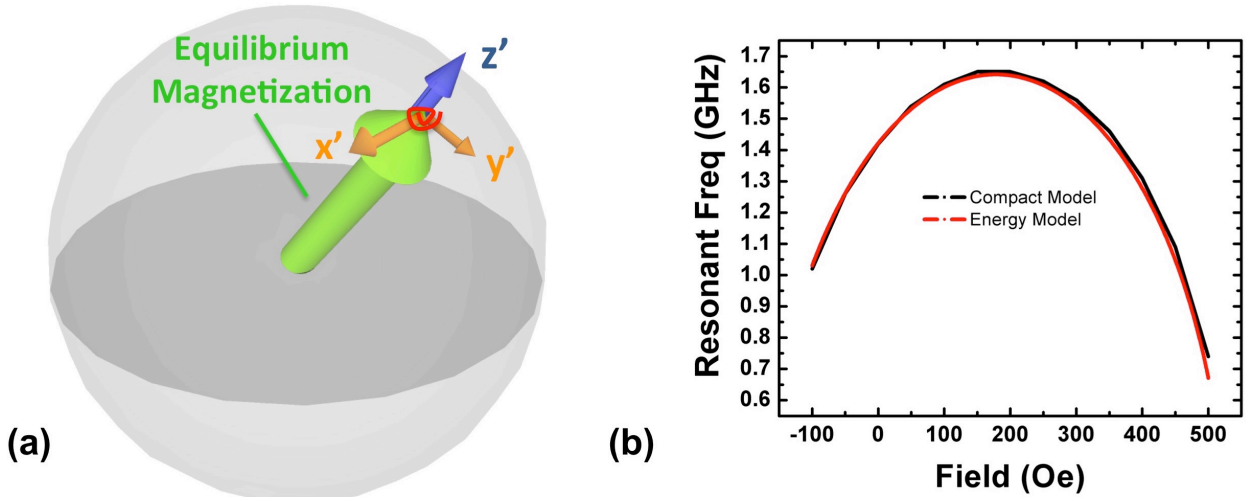

Fig. 4.10 (a) The equilibrium state in our devices is a canted magnetization, where the magnetization aligns with the total effective magnetic field. In order to construct a model for the dependence of the FMR frequency on the applied in-plane magnetic field and simplify the mathematics of the derivation, we consider a primed coordinate axis, where z' axis is chosen to lie along the equilibrium magnetization and the magnetization oscillation (precession) is in mostly in the x'-y' plane. (b) Validation of the proposed analytical model against a full numerical solution of the LLG equation, showing an excellent match in between both approaches.

$$f_{res} = \frac{\gamma}{2\pi}\sqrt{\left(H_{eff}^{z'}(V) - \frac{\delta H_{eff}(V)}{\delta x'}\right)\left(H_{eff}^{z'}(V) - \frac{\delta H_{eff}(V)}{\delta y'}\right)} \tag{4.15}$$

By calculating the total effective field $H_{eff}(V)$ in the primed coordinates from the free energy in equation (4.13) and using equation (4.15), a function that relates the FMR frequency f_{res} to the reduced first and second order anisotropy constants $\widetilde{K}_1(V)$ and $\widetilde{K}_2(V)$ is obtained. Particularly,

$$f_{res} = \frac{\gamma M_s}{2\pi}\sqrt{\left(\widetilde{N}_x + 6\widetilde{K}_2(V)m_{x,eq}^2\right)\left(\widetilde{N}_y + 2\widetilde{K}_2(V)m_{x,eq}^2\right)\left(1 - m_{x,eq}^2\right)} \tag{4.16}$$

where $\widetilde{N}_{x,y} = 4\pi N_{x,y} - 4\pi N_z + \widetilde{K}_1(V)$. It can be clearly observed that the resonance frequency depends on the equilibrium magnetization $m_{x,eq}$, hence on the applied magnetic field. Therefore,

in order to fit the FMR data in Fig. 4.9(a) to this model, we need to simultaneously take into account equation (4.16) and the minimization of equation (4.13). Note that $\widetilde{K}_1(V)$ and $\widetilde{K}_2(V)$ are the only unknowns in these equations, hence they are used as the two fitting parameters to numerically fit the model here described against the experimental data.

In order to validate the model, the dependence of the FMR frequency on in-plane magnetic field is calculated using the model here described, and the results are directly compared to the extracted values obtained from solving numerically the full LLG equation in the compact model described in section 2.6 with the same parameters for both cases. Fig. 4.10(b) demonstrates that our analytical model matches very well against the result from the full solution of the LLG equation.

4.6 Results and validation

4.6.1 Higher order contributions to the interfacial anisotropy and the VCMA effect

We use the model described in the last section to fit the extracted dependence of the FMR frequency on the applied in-plane magnetic field and the DC voltage V_{DC}, as shown in the experimental data on Fig. 4.9(a). The obtained results from the fitted dependence of the FMR frequency on the applied field for different DC voltages are shown on Fig. 4.9(b). It can be clearly noticed that the model matches very well qualitatively to the experimental data, reproducing the most important features such as the non-monotonic dependence of the FMR on field, as well as the FMR frequency modulation due to the VCMA effect. Also, the fitted model is observed to become quantitively worst at higher magnetic fields. This may be attributed to the strong micromagnetic pinning near the edges (see Fig. 4.6), which is not captured in our

macrospin model, resulting in the need for larger magnetic fields to saturate the magnetization (hence, a slower decay of the FMR frequency with field in the experimental data).

Fig. 4.11(a) shows the extracted values for the first order anisotropy

$$K_1(V_{DC}) = \frac{S_{i,1}(V_{DC})}{t_{\mathrm{CoFeB}}} = \frac{S_{i,1}(V=0) - \xi_1 \frac{V_{DC}}{d_{\mathrm{MgO}}}}{t_{\mathrm{CoFeB}}} \tag{4.17}$$

and the second order anisotropy

$$K_2(V_{DC}) = \frac{S_{i,2}(V_{DC})}{t_{\mathrm{CoFeB}}} = \frac{S_{i,2}(V=V_{DC}) - \xi_2 \frac{V_{DC}}{d_{\mathrm{MgO}}}}{t_{\mathrm{CoFeB}}} \tag{4.18}$$

from the fitted model over the experimental data. We obtain that the ratio between the first and second order interfacial perpendicular anisotropies at zero voltage is $S_{i,1}(V=0)/S_{i,2}(V=0) \sim 12$, in good agreement with previous experiments that characterized the second order anisotropy without the influence of the VCMA effect [109, 173].

Albeit the second order anisotropy $S_{i,2}(V=0)$ is indeed small, our results indicate that its sensitivity on the applied voltage via the VCMA effect ξ_2 is of comparable magnitude to the VCMA for the first order anisotropy ξ_1. In fact, the opposite slopes obtained for ξ_1 and ξ_2 indicate that the sensitivities of the first and second order interfacial anisotropy to the applied voltage tend to reduce the overall VCMA effect. It is worth noting that this is the first report that measures second order VCMA coefficient, therefore, future measurements on other material systems and further theoretical work may allow to understand the detail mechanisms behind K_2 and ξ_2, allowing to look for materials/conditions where the two VCMA coefficient add up, leading to a larger overall VCMA effect.

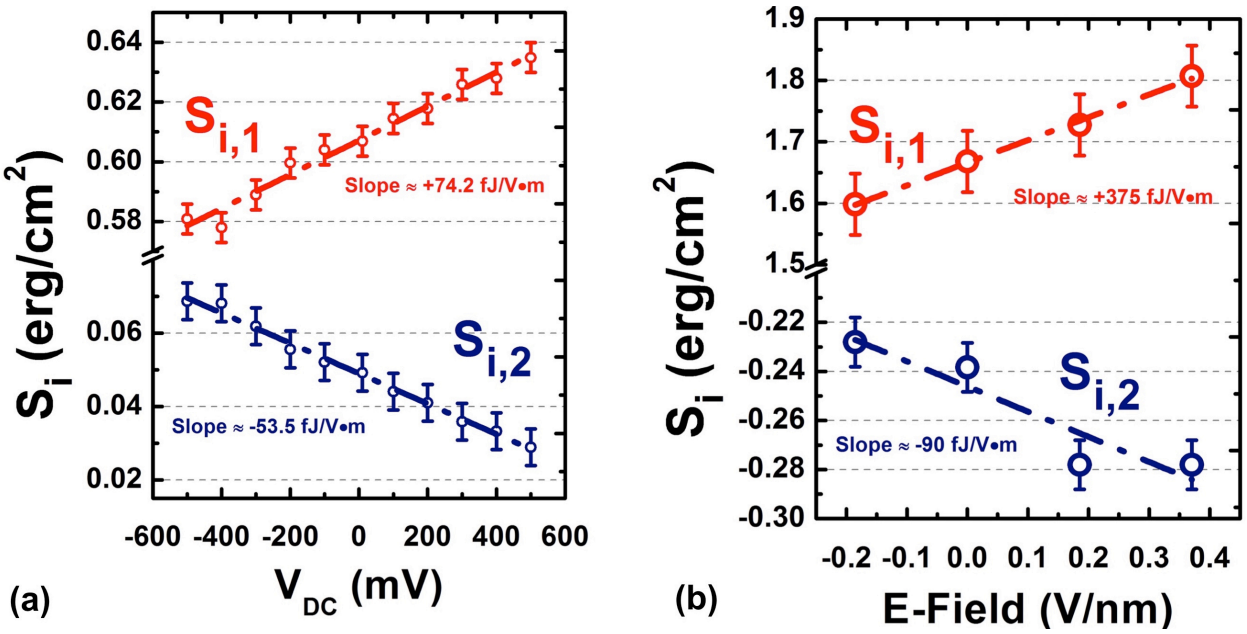

Fig. 4.11 (a) Extracted dependence of the first and second order interfacial anisotropy energy on the applied DC voltage. Albeit the second order anisotropy at zero voltage is at least one order of magnitude smaller, its sensitivity to the voltage is observed to be of the same order and of opposite polarity compared to the first order VCMA. (b) Preliminary first-principles calculations, courtesy of Dr. Vu Ong and Prof. Nicholas Kioussis at CSUN. Even though there is an obvious difference in the values of the interfacial anisotropy values and of the VCMA coefficients, the tendency for the sensitivities to the voltage (electric field) seems to be consistent with the experimental data (Data pending to be published).

4.6.2 Validation against first principles and experimental data

The obtained results are validated by using two different methods: First, we use the extracted values for $K_1(V)$ and $K_2(V)$ in our compact model described in section 2.6 to calculate the coercivities in the in-plane and the out-of-plane (OOP, perpendicular) directions, then we compare the results obtained from the compact model versus the measurements illustrated in Fig. 4.7. Fig. 4.12 shows the comparison of the dependence of the coercivities on the applied voltage in experiments and in simulations using the parameters extracted from the model, where we observe a good agreement in the tendencies for the two quantities. It is worth noting that only by having an explicit dependence of the second order anisotropy on the applied

voltage, as derived in this chapter, it is possible to explain that both the in-plane and the perpendicular coercivities decrease for positive voltages.

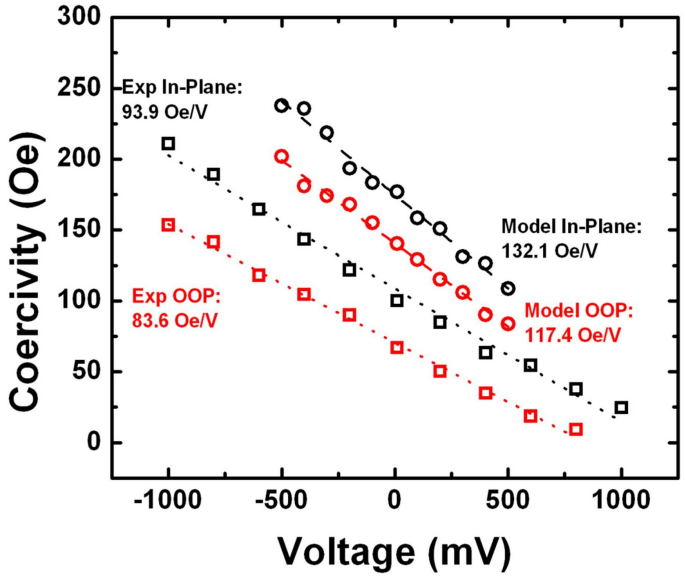

Fig. 4.12 Comparison of the dependence of the coercivity in the in-plane and out-of-plane (OOP) directions for experimentally measured data versus simulated values using our compact model with the parameters extracted for $K_1(V)$ and $K_2(V)$. It can be clearly observed that the parameters in the model are produce coercivities in simulations that well reproduce the experimental data. Notice that the dependence of the coercivity on $K_1(V)$ and $K_2(V)$ is modeled in the free energy equation (4.12) (Data pending to be published).

As an alternative validation, first principle calculations for a FeCo|MgO system were carried out by Dr. Vu Ong and Prof. Nicholas Kioussis at CSUN. The results are illustrated in Fig. 4.11(b). Albeit the first principle calculations reach different quantitative values for both, the anisotropies at zero voltage and their sensitivities to voltage, the same dependence for K_1 and K_2 is observed in the experimentally extracted data versus the first principle calculations. As discussed in section 4.1, a previous first-principles work by Yang, *et al.*, [118] reported a negligible K_2 in an unrelaxed Fe|MgO system. Therefore, the observation of a K_2 contribution

in the first principles calculations of Fig. 4.12(b) may be related to the CoFe alloy, or to lattice distortion when the system is relaxed. Nevertheless, the precise physics to explain the experimental reports here reported is still an open research question.

In summary, in this chapter we have studied for the first time the sensitivity of the second order anisotropy via the VCMA effect. We find that the second order interfacial anisotropy at zero voltage is approximately ten times smaller than the first order contribution, in good agreement with previous reports. Hence, the second order will only become important when the first order anisotropy is close to being cancelled, as discussed in detail on section 4.3. However, we also find that the second order VCMA coefficient ξ_2 cannot be neglected when describing MTJ dynamics properly, since it has a comparable magnitude to the first order contribution. It should be noted that the second order VCMA coefficient has a different angular dependence compared to the first order term ($\sin^4\theta$ versus $\sin^2\theta$), hence lumping first and second order contributions would not allow for an accurate description of the dynamics in the system. In consequence, whereas previous works have lumped all the different contributions to VCMA into a first order term with a $\sin^2\theta$ dependence, this work provides a critical result towards improving the description of the VCMA effect by separating the contributions to the $\sin^2\theta$ and $\sin^4\theta$ angular dependencies.

CHAPTER 5: VCMA-driven switching of nanoscale MTJ devices

5.1 Introduction

In the previous chapters, the VCMA effect has been systematically studied, including a review of the contributing mechanisms and scalability, and a detailed characterization of effect, including temperature dependence and higher order contributions. However, one of the main results of this dissertation is the demonstration that the VCMA effect can be utilized as a switching mechanism for nanoscale MTJ devices, serving as a proof of concept for a future MeRAM architecture with the potential advantages outlined in Chapter 2.

Exploiting the VCMA effect to write the information into nanoscale MTJ devices is challenging due to two reasons: First, as discussed previously on Chapter 2, the strength of the effect in high TMR structures (e.g., Ta|CoFe|MgO stacks) is currently small, allowing only to modulate the interfacial perpendicular anisotropy in around 2-4% per every 1 V/nm of applied electric field (corresponding to magnetoelectric coefficients of 20-40 fJ/V-m, as discussed previously on section 2.3.3). Therefore, even when operating at electric fields close to the typical MgO breakdown field measured in our devices (~ 2 V/nm for nanosecond voltage pulses), the maximum modulation of the anisotropy in Ta|CoFe|MgO stacks is ~4-8%. In consequence, the parameters of the device such as the thickness of the CoFeB and the MgO layers, and the device structure in general, must be very carefully tuned to allow for VCMA-driven switching. Clearly, increasing the strength of the VCMA coefficient will enhance the operation window in the parameter space, resulting in a more robust operation for the device.

Further, there is a second challenge, which is more related to the fundamental physics of the VCMA effect, and in general, to schemes based on the modulation of uniaxial anisotropies.

Consider the situation illustrated on Fig. 5.1, where we start with the magnetization in one of two stable perpendicular states (P or AP) without any applied voltage. An energy barrier that can be controlled by the applied voltage via the VCMA effect separates the two states. Note that having the equilibrium (i.e., memory) states with a separation of 180° is highly desired in MTJs since it maximizes the output TMR signal.

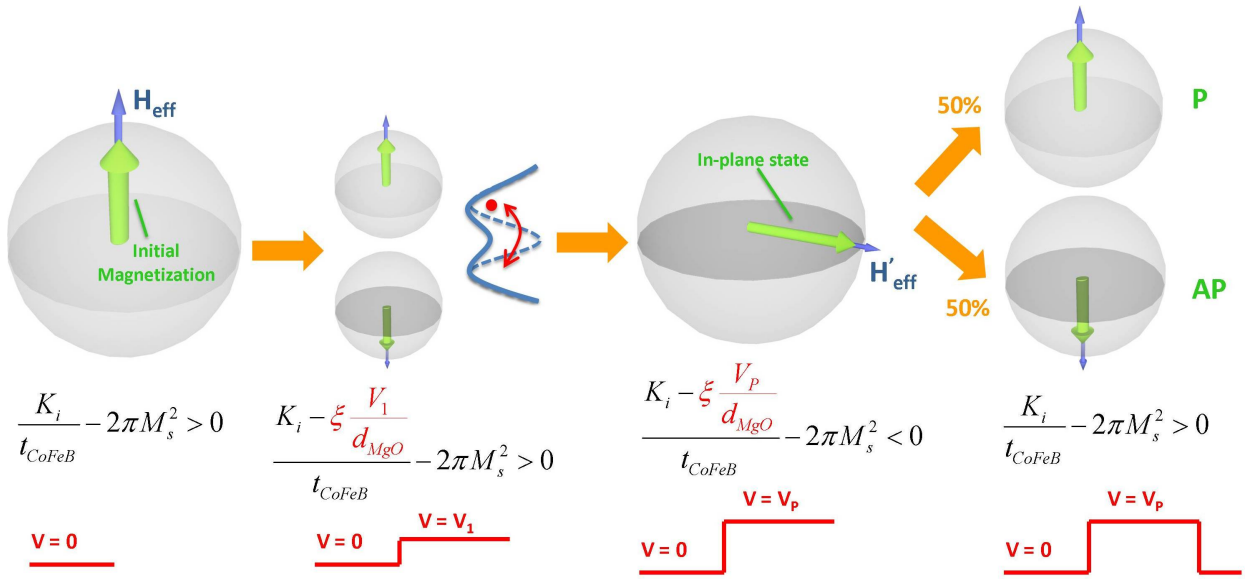

Fig. 5.1 One of the challenges for VCMA-driven switching is that VCMA can only perform 90° rotation of the magnetization. If we consider the energy barrier between the two perpendicular states, a voltage V_1 that lowers the barrier result in a thermally unstable free layer, with a random end state. If the voltage is further increased to V_P, the magnetization goes to the in-plane direction and the final perpendicular state after the voltage is removed will have a 50-50% distribution in the presence of thermal fluctuation.

By applying a voltage V_1 that lowers the energy barrier without destroying it, the magnetization can escape the energy well in the presence of thermal fluctuations. However, this process is stochastic, and can give rise to switchback events. In other words, the free layer becomes thermally unstable and the final state after removing the voltage will be random. If the voltage if further increased to V_P such that the energy barrier is destroyed, the magnetization is rotated by 90° to the new minimum energy state in the in-plane direction. Yet, once the voltage

is removed, the magnetization will go to either P or AP 50% of the times due to statistical thermal fluctuations. Consequently, the VCMA effect alone cannot be used to perform controlled switching (i.e., with very high switching probability) from P to AP and vice versa. Note that this is fundamentally different from STT, where controlled switching in different directions can be obtained by just changing the direction of the applied current. The fact the VCMA effect does not have a preference in between the equilibrium states poses a challenge where additional device engineering is required to obtain controllable switching.

In this chapter, we demonstrate experimentally four different switching approaches where VCMA-driven controllable switching is obtained in nanoscale MTJ devices by using either bias magnetic fields, STT currents to aid the switching, precise timing of the VCMA-induced magnetization dynamics, or a combination switching at two different time scales (i.e., combined thermally activated and precessional switching)

5.2 Methods

The devices utilized in this chapter are elliptical or circular nanoscale MTJ devices, fabricated in collaboration with HGST inc. The MTJ stacks are designed and subsequently sputter-deposited in a TIMARIS physical vapor deposition (PVD) system by Singulus Technologies AG. The MTJs are first patterned into nanopillars via ion milling. Consequently, a bottom electrode is defined, followed by encapsulation of the MTJ with an oxide layer, then by patterning electrodes to make electrical contact to the bottom electrode and to the MTJ device (2-terminal configuration). The electrodes are defined in a co-planar waveguide GSG configuration in order to use RF probes for probe station testing. The pad layout is designed to have a bandwidth up to 40 GHz, taking into account shunt capacitances in the pad layout and the

resistance of the MTJ device. Fig. 5.2(a) shows cross section TEM figures of a fabricated MTJ device, meanwhile Fig. 5.2(b) presents a microscope pictures of the RF electrode pad layout used to make electrical contact to the devices.

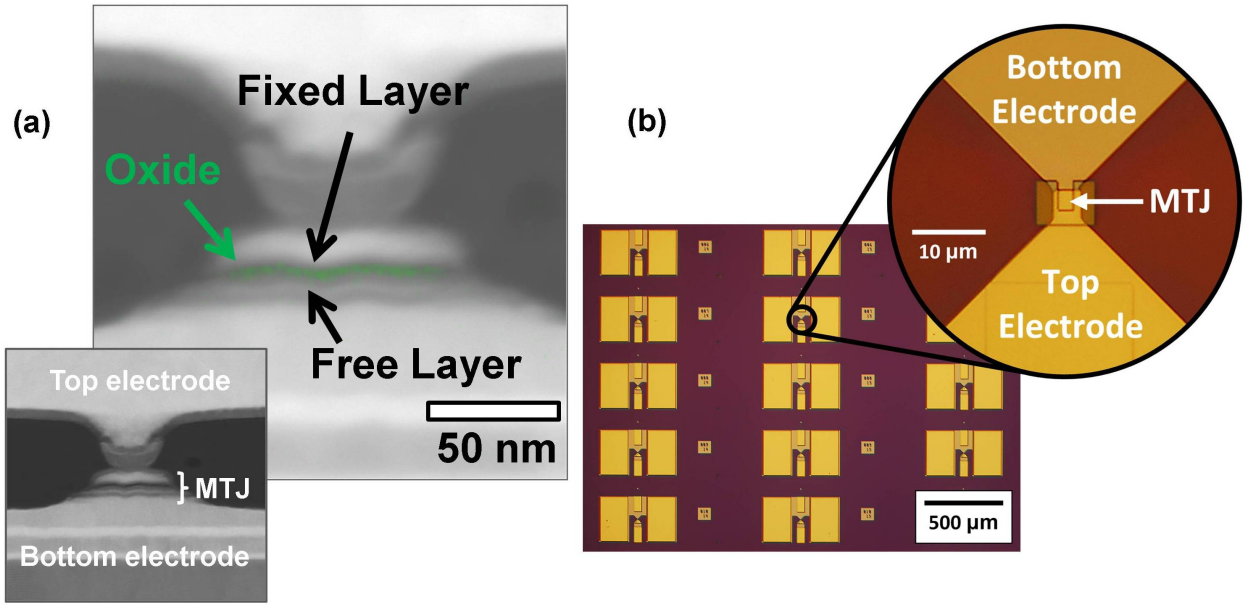

Fig. 5.2 (a) Cross sectional TEM pictures of a fabricated MTJ device. Energy-dispersive X-ray spectroscopy (EDS) is utilized to identify the Mg (in green) in the MgO oxide (b) Microscope pictures of the RF pad layout to probe the MTJ devices.

In order to perform switching studies over the devices, the generic circuit in Fig. 5.3(a) was utilized. A bias-tee is used to combine the RF writing pulses with a DC sourcemeter that measures the resistance state of the device. Due to the large resistance of our MTJ devices (~ 10-200 kΩ), there is a very large impedance mismatch at the device for the RF pulses; therefore, an attenuator is used in front of the RF pulse generator with the objective to filter the reflected pulses from the MTJ, avoiding them from being sent back to the MTJ after being bounced back from the pulse generator. As a part of the dissertation work, a dedicated DC/RF probe station with the possibility of applying bias magnetic fields up to 2.1 kOe at any angle in the H_x-H_z

plane was constructed. The photographs in Fig. 5.3(b) show the resulting set-up for the probe station, including a close-up on a device being tested using DC probes.

In the next sections, we describe experimental demonstrations of four different switching schemes utilizing the nanoscale MTJ samples here described.

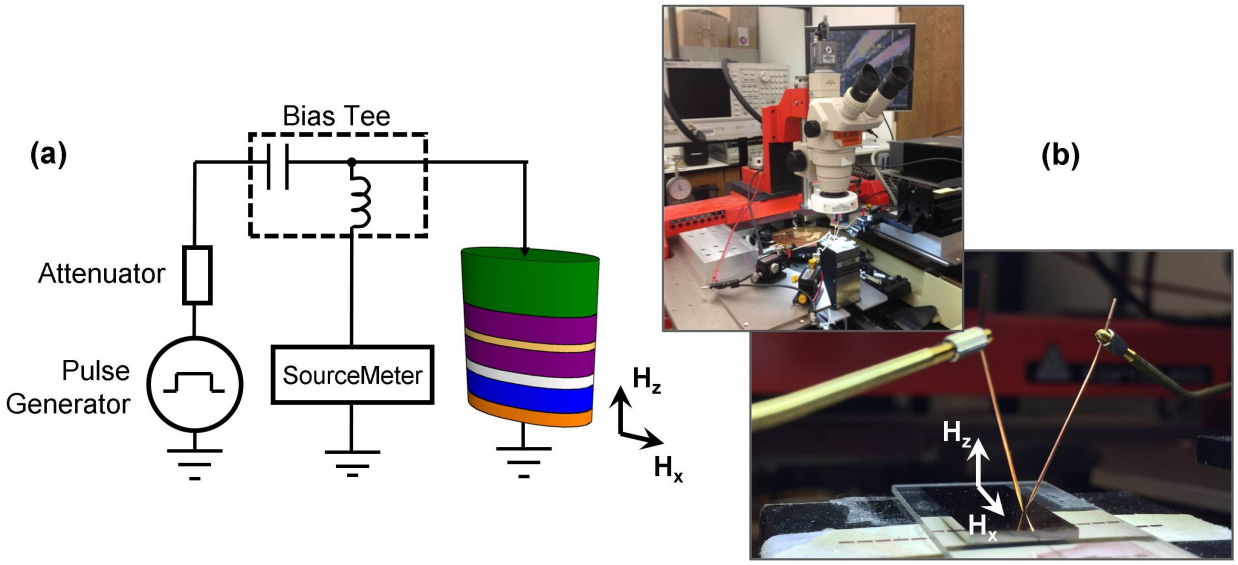

Fig. 5.3 (a) Circuit for studying VCMA-driven switching of nanoscale MTJs. The pulse generator creates the writing pulses, while the sourcemeter tracks the resistance state of the MTJ. An attenuator is introduced to mitigate the large impedance mismatch of the MTJ. (b) Probe-station set-up for this project, with the capability of DC and RF studies with any bias magnetic field up to 2.1 kOe in the H_x-H_z plane.

5.3 Field-assisted switching

As one of the main results of this dissertation, our experiments were one of the pioneers in the demonstration of VCMA-driven switching of nanoscale MTJ devices [112, 113] along with the reports by Wang, *et al.*, [114] and Shiota, *et al.*, [115]. For the cited first demonstration, an additional bias magnetic field was used to assist the switching by breaking the symmetry between the P and AP states.

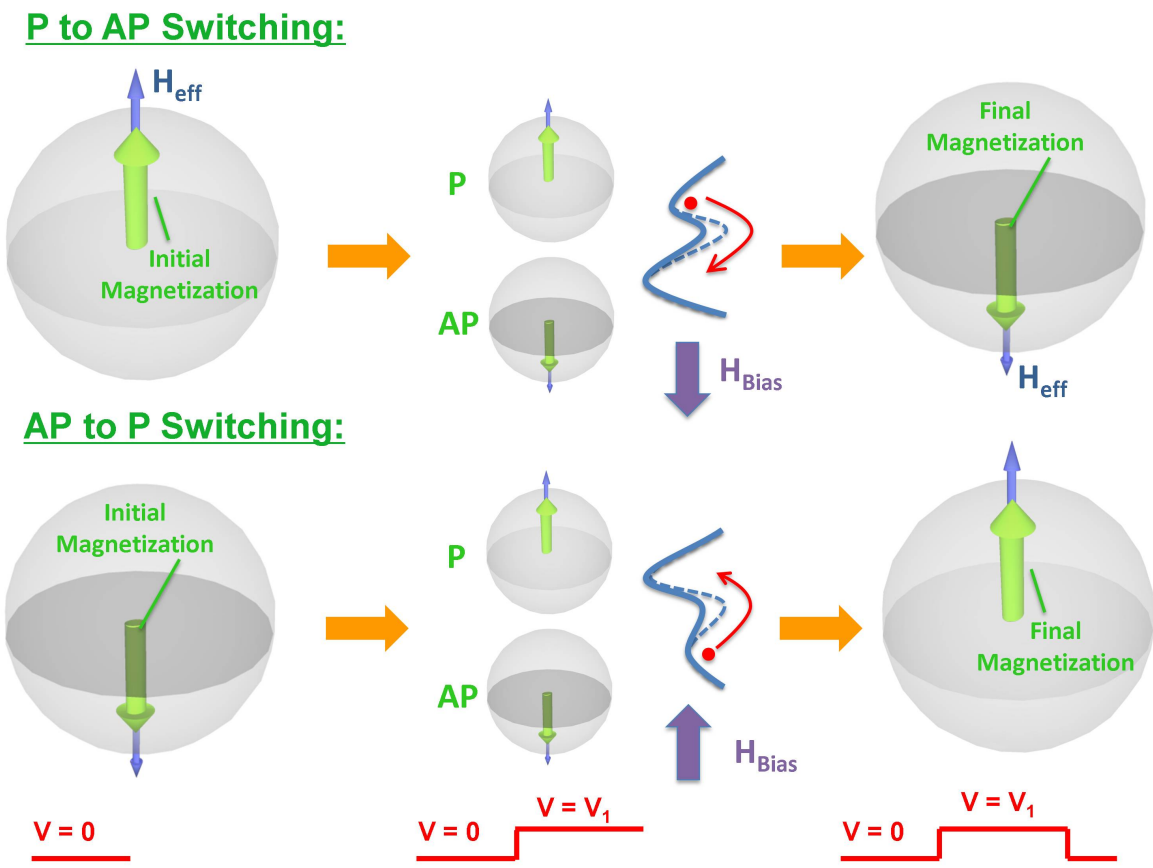

Fig. 5.4 Switching mechanism for field-assisted, VCMA-driven switching of the magnetization. The application of a voltage V_1 lowers the original energy barrier (dashed), allowing for thermal fluctuations to switch the magnetization into the minimum energy state. Note that the direction of H_{Bias} controls the switching direction.

The switching mechanism for field-assisted VCMA-driven switching is illustrated in Fig. 5.4. In addition to the voltage pulse that lowers the energy barrier between the two stable states, an additional bias magnetic field H_{Bias} is added in order to favor the desired final state for the magnetization. Once the barrier is lowered because of the VCMA effect, the direction of H_{Bias} determines the switching direction by creating a minimum energy state where the magnetization state can fall via thermal activation. Note that the large energy barrier seen by the magnetization once it falls into the minimum energy well prevents switchbacks, resulting in controlled switching.

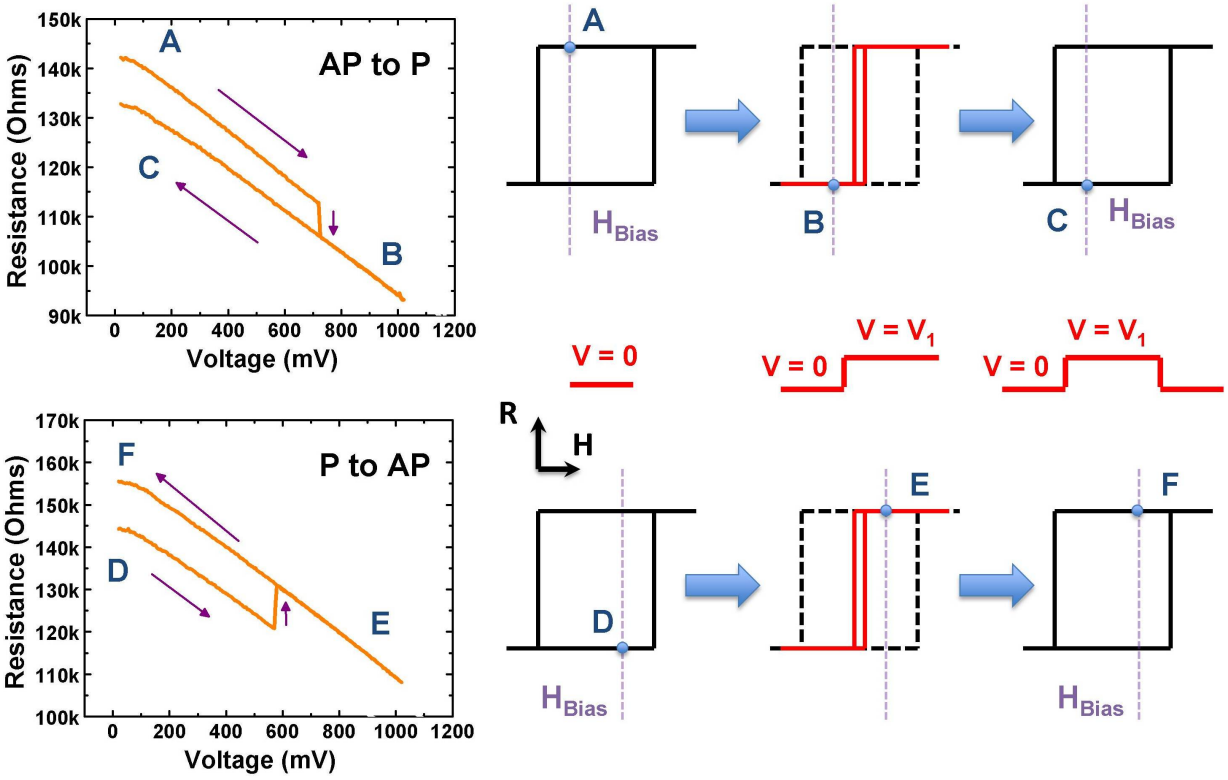

Fig. 5.5 (Left) Resistance versus voltage curves for two different polarities of $H_{Bias.}$ The continuous decrease of the resistance with voltage is due to the bias dependence of the TMR effect [26]. Here, a positive voltage is such that it accumulates electrons near the CoFeB|MgO interface, therefore reducing the perpendicular anisotropy. The quasi-static curves demonstrate that switching in opposite directions can be obtained by changing the sign of $H_{Bias.}$ (Right) The switching process is completed when the coercivity is reduced and forces the magnetization to go the only available state (B, E) depending on H_{Bias}.

The principle of field-assisted switching in our devices was demonstrated experimentally from the quasi-static regime down to using nanosecond voltage pulses. Fig. 5.5 demonstrates VCMA-driven quasi-static switching for two different polarities of the bias field H_{Bias} for an MTJ device with a TMR ratio ~ 7%. The MTJ stack is the same utilized in Chapter 4, whereas a positive voltage is defined such that it accumulates electrons in the CoFeB|MgO interface, hence decreasing the perpendicular anisotropy (see section 2.3.3 for a detailed description). For AP to P switching, the magnetization is assumed to start in point A. As the positive voltage is increased,

the anisotropy decreases and leads to a reduction of the coercivity. At the switching voltage, there is only one available state at H_{Bias}, forcing the magnetization to switch to point B. Once the voltage is released, the magnetization has switched to point C. Similarly, switching for P to AP is performed by changing the polarity of H_{Bias}, following the D to E to F process in Fig. 5.5. The curves showing the dependence of the MTJ resistance on the applied voltage in Fig. 5.5 demonstrate that switching can be obtained with voltages on the order of ~0.6-0.7 V, meanwhile the switching direction depends on the polarity of $H_{Bias.}$ Note that, by exploiting the VCMA effect, values of H_{Bias} much smaller than the coercivity are required to induce the magnetization reversal.

Further, the field-assisted switching can also be achieved by using nanosecond voltage pulses. Fig. 5.6(a) shows the dependence of the mean switching voltage V_c (defined as the voltage for 50% switching probability) as a function of the duration of the voltage pulse for a bias field H_{Bias} = ± 80 Oe. Switching is achieved with pulses down to 10 nanoseconds using voltages on the order of ~ 1-1.5 V. Notice that the required switching voltage decreases as the pulse duration is increased, indicating a thermally-activated process where longer times require a smaller lowering of the energy barrier to allow for thermal fluctuations to trigger the process. In fact, for a thermally activated process, the switching probability is given by [180]

$$P_{sw}\left(V,t,H_{Bias}\right)=1-\exp\left(-t/\tau\left(V,H_{Bias}\right)\right) \tag{5.1}$$

where t is the pulse duration and $\tau\left(V,H_{Bias}\right)$ is the dwell time, as defined on Chapters 1 and 2. In the presence of a bias magnetic field H_{Bias}, the energy barrier E_b is modified as $E_b\left(H_{Bias}\right)=E_b\left(H_{Bias}=0\right)\left(1-H_{Bias}/H_{k,eff}\left(V\right)\right)^n$, where n depends on the trajectory of the magnetization switching through the barrier and on the symmetries of the system. Refs. [180, 181] provide detailed studies on this topic and demonstrate that n typically has values between

3/2 and 2. The total effective magnetic field $H_{k,eff}(V)$ is a function of the applied voltage and obeys the relation derived previously in equation (2.12)

$$\frac{M_s H_{k,eff}(V) A t}{2kT} = \Delta(V=0) - \frac{\xi A}{dkT} V \tag{5.2}$$

In the context of field-assisted switching, usually $H_{Bias} \ll H_{k,eff}(V)$, hence the dependence of the energy barrier on H_{Bias} is $E_b(H_{Bias}) = \left(1 - H_{Bias} / H_{k,eff}(V)\right)^n \approx 1 - nH_{Bias} / H_{k,eff}(V)$. Consequently, equation (2.13) for the dwell time can be modified to include the influence of H_{Bias}, specifically

$$\tau(V, H_{Bias}) = \tau_0 \exp\left[\left(\Delta(V=0) - \frac{\xi A}{dkT} V\right)\left(1 - \frac{nH_{Bias}}{H_{k,eff}(V)}\right)\right] \tag{5.3}$$

which, taking into account equation (5.2), can be rewritten as

$$\tau(V, H_{Bias}) = \tau_0 \exp\left[\Delta(V=0) - \frac{\xi A}{dkT} V - \frac{M_s n H_{Bias} A t}{2kT}\right] \tag{5.4}$$

The mean switching voltage V_c is defined at 50% of the switching probability, i.e., based on equation (5.1), $P_{sw}(V_c, t, H_{Bias}) = 1 - \exp\left(-t / \tau(V_c, H_{Bias})\right) = 0.5$. Hence, by using the result obtained for the dwell time in equation (5.4), we require that

$$\exp\left(-\frac{t}{\tau(V_c, H_{Bias})}\right) = \exp\left(-\frac{t}{\tau_0} \exp\left[\frac{\xi A}{dkT} V_c + \frac{M_s n H_{Bias} A t}{2kT} - \Delta(V=0)\right]\right) = 0.5 \tag{5.5}$$

from where we can derive an expression for the mean switching voltage V_c as a function of the pulse duration t, particularly,

$$V_c = V_{c0}\left[1 - \frac{1}{\Delta^*(V=0)} \ln\left(\frac{t}{\ln(2)\tau_0}\right)\right] \tag{5.6}$$

with $V_{c0} = dkT\Delta^*(V=0)/\xi A$ as the switching voltage at a time $t = \ln(2)\tau_0$, and we redefine the thermal stability taking into account the bias field as $\Delta^*(V=0) = \Delta(V=0) - M_s n H_{Bias} At / 2kT$. As observed in Fig. 5.6(a), the macrospin model developed to capture the physics of the thermally activated switching is found to fit well with the experimental data.

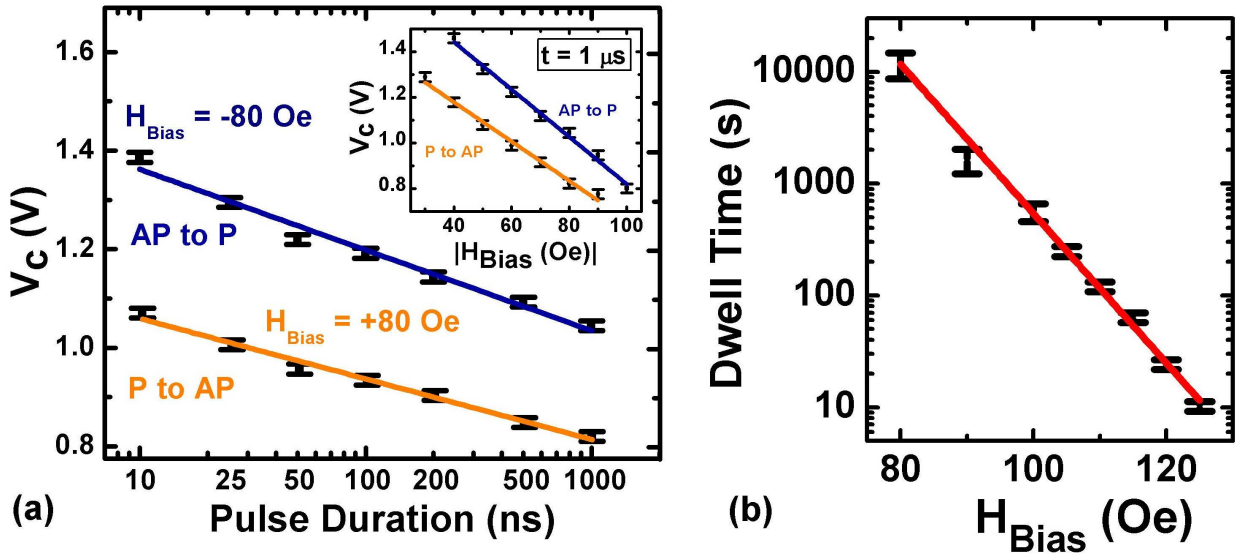

Fig. 5.6 (a) Depencence of the mean switching voltage on pulse duration for two different bias fields. The data is found to fit well into a thermal activation model developed in this section. The inset shows the expected trade-off between switching voltage and bias field, where the dependence is also found to be in good agreement with our analytical model. (b) Measurements of the dwell time as a function of the bias field. By extrapolating to the zero bias condition, it is estimated that the thermal stability for this device is ~ 42 at equilibruim. Notice that the dwell time was measured with a very small bias voltage of 10 mV applied to the device since any larger voltage will result in a decrease of the dwell times because of the VCMA effect.

Similarly, a trade-off between the bias field used and the mean switching voltage is observed in our experiments (see the inset of Fig. 5.6(a)). Such trade-off is expected since smaller bias fields will require to lower energy barriers (hence, larger voltages) to complete the

process. From equation (5.5), we can derive an expression for the mean switching voltage as a function of the bias field, specifically

$$V_c = \frac{dkT}{\xi A}\left(\Delta(V=0) - \frac{M_s n H_{Bias} A t}{2kT} - \ln\left(\frac{t}{\ln(2)\tau_0}\right)\right) \tag{5.7}$$

The inset of Fig. 5.6(a) shows that the experimental data is again found to fit well with the predicted linear dependence of V_c on H_{Bias}.

Finally, as discussed in Chapters 1 and 2, the figure of merit for VCMA-driven switching is the switching voltage over the thermal stability, so we estimate what is the thermal stability for the devices used in our demonstration. To do so, we measure the dwell time as a function of the bias field, as shown on Fig. 5.6(b). From equation (5.4), a linear relation between $\log\left(\tau\left(V=0, H_{Bias}\right)\right)$ and H_{Bias} is theoretically expected, which is in good agreement with the experimental observation. By extrapolating to $H_{Bias}=0$, we can estimate the dwell time at equilibrium, i.e., without any bias field or voltage applied to the device. For our experiment, we estimate that the dwell time at equilibrium is $\sim 1.7 \times 10^9$ seconds (> 50 years), corresponding to $\Delta(V=0) \approx 42$, sufficient stability for non-volatile memory operation.

It is worth mentioning that the switching energy $E_w = CV_c^2 + \left(V_c^2/R\right)t_w$ for this first demonstration, using write pulses of 10 ns, is estimated to be on the order of 60 fJ, already lower than the switching energies of STT-MRAM. The switching energy could be further decreased below 10 fJ by increasing the resistance of the device, reducing undesired leakage currents. However, this approach would be limited by the impedance matching to the access transistor and by the possible limitations when reading-out a very large MTJ resistance. Also, the switching energy calculation does not include the energy required to generate the bias magnetic fields to assist the switching.

Albeit the field-assisted switching serves as a proof of concept of the possibility of using VCMA to switch MTJ devices, and also as a testing vehicle for the analytical models for VCMA-driven switching, it is far from being practical, essentially due to the need of additional circuitry and wiring to generate the bias fields to assist the reversal process. VCMA could be in principle used in Oersted-field-switched (toggle) MRAM to eliminate the need to create bias magnetic fields along the hard-axis (see section 1.5), while also reducing the amount of current required to induce switching in the memory devices. However, this would still not solve the main issue of Oersted-field-switched (toggle) MRAM related to the negative scalability of the technology, where the switching current scales with the inverse of the volume.

In conclusion, requiring different bias fields to achieve VCMA-driven switching is highly undesired and mechanisms without the need of any bias magnetic field, or at least a constant field that can be introduced in the design of the stack, are needed. In the next sections, we present three mechanisms that serve as potential solutions to this issue.

5.4 STT-assisted switching

The first approach for MeRAM that utilizes a constant bias magnetic field, which can be engineered into the material stack, is STT-assisted switching [114, 182]. The use of STT to assist the VCMA-driven switching process allows to write the MTJ in both directions using voltages of the same polarity, but with different magnitudes. The latter is fundamentally different from pure-STT switching and results in possible architectural advantages against STT-MRAM that will be discussed later in this section.

Fig. 5.7 shows schematically how voltage pulses of the same polarity, but different amplitudes, can be used to switch an MeRAM device in opposite directions for a fixed value of

the bias magnetic field H_{Bias} acting over the free layer [113, 182]. In our experiments, the bias field is a combination of the stray field from the unbalanced synthetic antiferromagnet (SAF) in the fixed layer (see Fig. 4.4), as well as an externally applied magnetic field (which is fixed throughout the experiment and can be removed in an optimized device by a proper design of the SAF in the fixed layer to provide the required H_{Bias} on the free layer). This field favors one of the states in the free layer, i.e., AP state in Fig. 5.7, but is small enough not to compromise the bistability of the P state. The P to AP switching process is very similar to the field-assisted scheme discussed in the previous section: The application of a voltage V_1 lowers the equilibrium energy barrier (dashed), allowing for thermal fluctuations to switch the MTJ to the lower energy AP state, as illustrated in Fig. 5.7. However, for the opposite switching direction (i.e., AP to P for this discussion), instead of changing H_{Bias}, the STT effect is utilized to complete the process. By optimizing the resistance of the device and properly designing the direction of the fixed layer with respect to the current flow, a voltage $V_2 > V_1$ will result in a spin-polarized current with contributions from spin-torque and field-like torque that favors the P direction. As discussed in section 2.6, field-like torque acts as current-dependent effective field, creating an energy minimum for the P state. On the other hand, spin-torque cannot be described as an effective bias field, but it will also contribute to AP to P switching by creating anti-damping conditions in the AP state (i.e., increasing the effective temperature of the AP energy well [180]), hence also favoring the P state. Therefore, the application of a voltage V_2 will result in AP to P switching, as shown on Fig. 5.7.

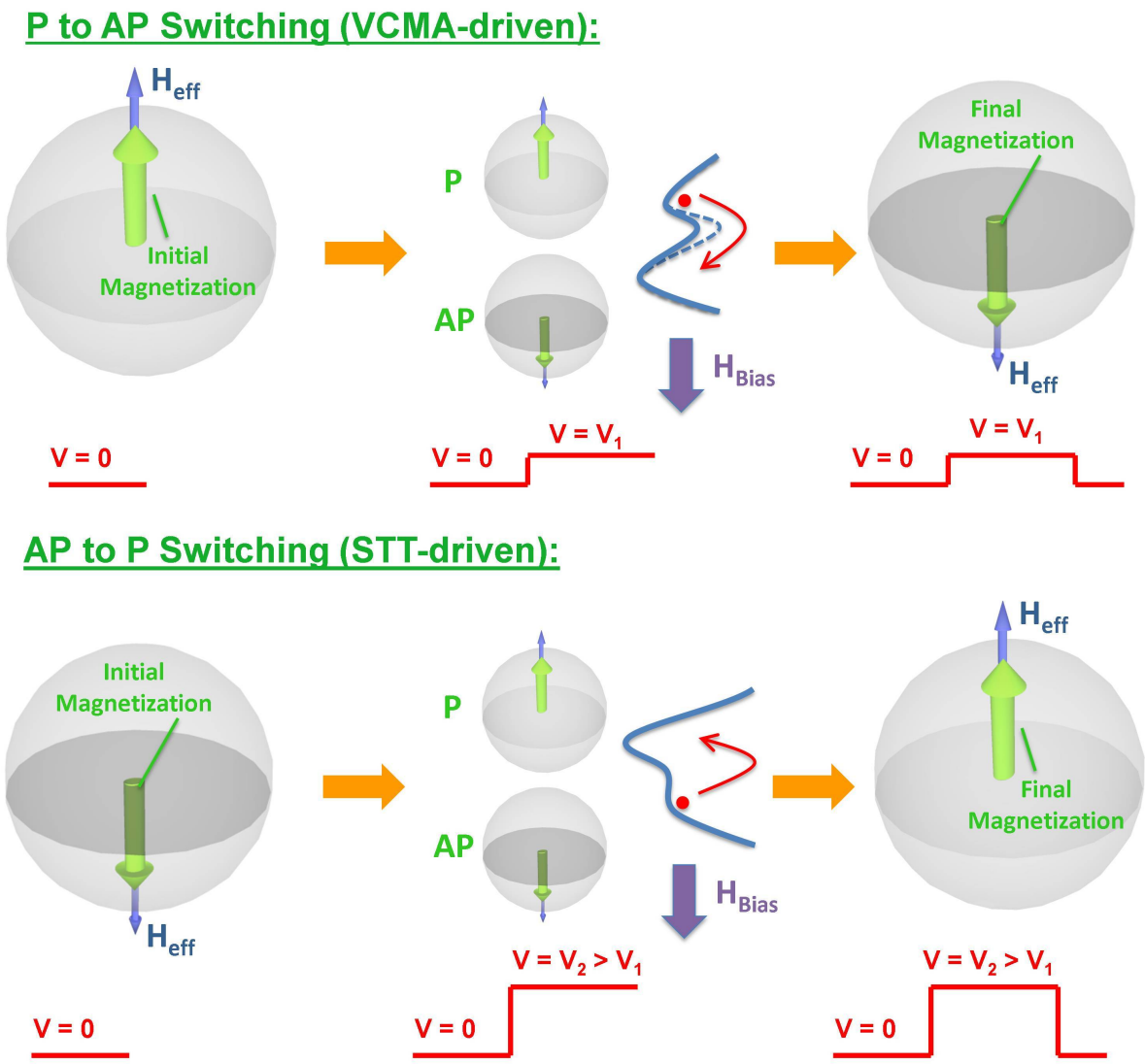

Fig. 5.7 Switching mechanism for STT-assisted switching. Here, the voltage polarity is such that a positive voltage reduces the perpendicular anisotropy, while STT favors the P state for the same polarity. The P to AP process is analogous to field-assisted switching, with the bias field creating a global minimum that favors the AP state. For AP to P switching, a spin-polarized current overcomes the bias field and generates a new energy minimum in the P direction; hence, the magnetization will switch to this direction. Notice that this switching scheme does not require any change in the bias magnetic field H_{Bias}. In order to engineer switching in the opposite directions (e.g., AP to P driven by VCMA and P to AP driven by STT, the polarity of the bias field as well as the direction of fixed need to be reversed.

The switching process can be also explained in terms of R-H loops, as illustrated in Fig. 5.8. As reasoned in the previous chapters, once a voltage V_1 of the proper polarity is applied, the

modification of the interfacial perpendicular anisotropy via the VCMA effect reduces the coercivity of the free layer. If the coercive range crosses H_{Bias}, there would be only one available state for the magnetization, forcing P to AP switching in the case of Fig. 5.8(a). When the voltage is increased to V_2, the coercivity will further decrease, but also STT effects become dominant. If the polarity is adequately designed such that STT favors the opposite direction as compared to the bias field H_{Bias}, a voltage pulse V_2 will induce a shift in the R-H loop due to the combined effect of STT and field-like torque. Hence, AP to P switching is obtained in Fig. 5.8(b) once the current is large enough to make the P state the only energetically available condition for the magnetization. This allows for a unipolar set/reset write scheme, where voltage pulses of the same polarity, but different amplitudes, can be used to switch the device between the P and AP states.

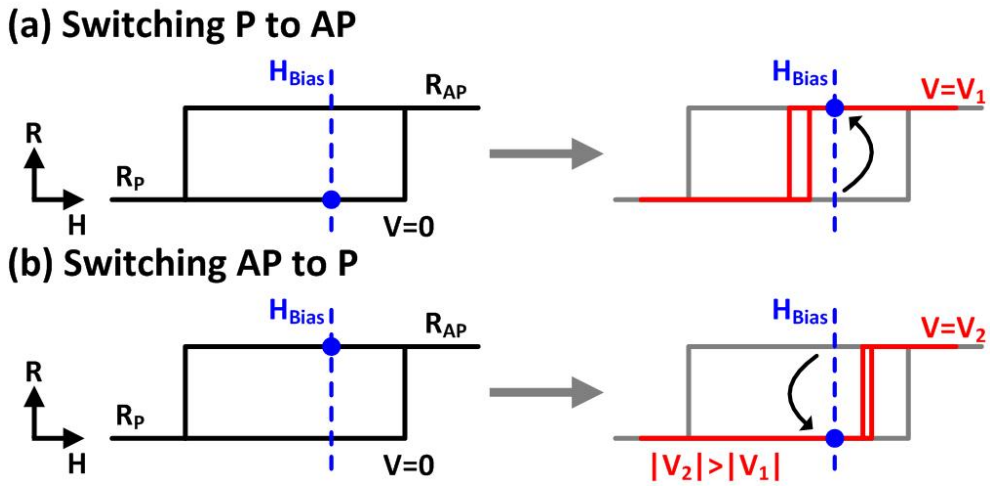

Fig. 5.8 Writing of the VCMA-driven MTJs in the P to AP direction is accomplished by a voltage V_1, which reduced the coercivity of the free layer and results in a single available state at the bias field H_{Bias} the latter provided by the fixed layer. Further increasing the magnitude of the voltage to V_2 allows STT to switch the device in the opposite (e.g., AP to P) direction due to an effective shift of the coercivity. The shift is due to combined contributions from spin-torque and field-like torque [182].

Notice that this switching scheme can be used in both, perpendicular and in-plane MTJ junctions: In perpendicular devices, the coercivity of the free layer can be directly controlled by

voltage via the VCMA effect (see Fig. 2.3), meanwhile the coercivity in in-plane devices can become sensitive to the VCMA effect by properly engineering the perpendicular anisotropy close to the compensation between in-plane and out-of-plane equilibrium states [135]. In both scenarios, there is no need for external magnetic fields and the bias field is provided by the uncompensated SAF in the fixed layer. However, the asymmetry introduced by the unbalanced fixed layer needs to be taken into account when assuring enough thermal stability for the state not favored by H_{Bias}. Finally, note that voltage pulses of the opposite polarity will not switch the device, but rather reinforce the initial state, up to the moment where STT becomes dominant.

The proof of concept of this STT-assisted mechanism was performed using our MTJ devices. The layered stack for the first demonstration was the one used in Chapter 4, but reducing the RA product to ~50 Ω-μm^2 (MTJ resistance ~ 5 kΩ) to allow for enough charge current to flow through the device in order to provide enough STT for switching. However, it is worth mentioning we have validated the concept also in in-plane devices with TMR ratios up to 110%, and in perpendicular devices with TMR up to 45%, in both cases obtaining very similar results to the ones here presented. Fig. 5.9 shows the switching probability for both switching direction (P to AP and AP to P) in a 190 × 60 nm^2 device, demonstrating the unipolar set/reset characteristics of STT-assisted switching. Data was obtained using 100 repetitions for each voltage with 100 ms pulse widths. The VCMA coefficient was estimated to be on the order of 30 fJ/V-m. Switching in the P to AP direction is achieved by voltage pulses of 0.5 V; meanwhile, AP to P requires a voltage of 1.1 V. A small overlap in between switching peaks is observed, which is expected to be reduced for larger VCMA effect values. Also, notice that the current demonstration in our devices is limited only to pulses down to 100 ms due to the small VCMA effect in Ta|CoFeB|MgO-based MTJ samples. As demonstrated in Fig. 5.6, decreasing the pulse

duration increases the required voltage, moving the first peak in Fig. 5.9 towards higher voltages, hence overlapping with the second (STT) peak and eliminating the possibility of switching in both directions. A simple calculation based on equation (5.6) assuming that the sample area remains constant and that $\Delta^*(V=0)=30$ after taking into account the effect of barrier lowering due to H_{Bias}, yields that, if we currently require 0.5 V to switch at 100 ms, an increase of 6x in the VCMA coefficient (e.g., from 40 fJ/V-m to 240 fJ/V-m) is required to switch with 0.2 V (also reducing the overlap between the set/reset peaks) at 10 ns.

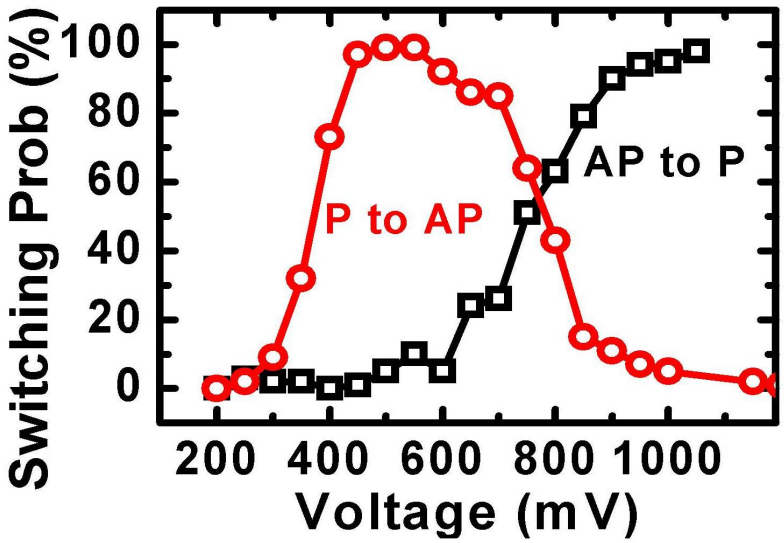

Fig. 5.9 Measured probability of switching curves for the VCMA-driven STT-assisted MTJ switching. Data was obtained using 100 repetitions for each voltage with 100 ms pulse widths. The combination of VCMA and STT effects allows for a unipolar set/reset switching scheme with switching voltages 0.5V and 1.1V respectively. It is worth noting that the current switching time is limited by the first peak (VCMA-driven switching), since STT can reach already switching times at the nanosecond regime.

As mentioned previously, having a unipolar set/reset scheme for MRAM results in potential architectural advantages over STT-MRAM. STT-MRAM normally uses a 1-Transistor/1-MTJ (1T-1MTJ) memory cell structure (see Fig. 1.9), with CMOS transistors as the access devices. However, the relatively large currents required to switch STT-based MTJs

require fairly large transistors to drive them, limiting the density of STT-MRAM (see the discussions on sections 1.6 and 2.4). Additionally, the use of three-terminal CMOS transistors also imposes a layout-based limit of 6-8F^2 on the maximum cell density.

The use of transistors in STT-MRAM is dictated by its purely current-controlled write mechanism, where currents of opposite polarities are needed to write different bits of information, preventing the realization of crossbar arrays with diodes as the access devices. However, in the VCMA-driven STT-assisted, writing is performed by using a single polarity for the voltage, therefore allowing the use of diodes as access devices. In principle, crossbars are the densest memory arrays possible (with a $4F^2$ cell size), and hence the realization of a diode-controlled memory cell for crossbar arrays can greatly increase the density and scalability of MRAM. Additionally, the crossbar architecture allows for 3D stacking of multiple diode-MTJ memory layers in the CMOS back-end-of-line (BEOL) fabrication steps, increasing the effective density with each layer ($2F^2$ for two layers, etc.).

In order to prove this concept, we performed experiments for a small array of two MTJ devices, using two discrete germanium diodes (V_{TH} = 0.2 V) as access devices. Fig. 5.10(a) shows the test array configuration, where the two diodes are connected to a common Bit Line (BL), whereas each MTJ can be biased by using the separate Source Lines (SL_1 and SL_2). During both reading and writing, unaccessed BLs are grounded while unaccessed SLs are pulled to V_{DD} (1.5 V), reverse biasing the series diode for unaccessed bits. During the write operation, the target SL is pulled to ground, while the target BL is pulsed with the appropriate set/reset voltage, V_{WRITE} = 0.5 and 1.1 V, respectively. During the read operation, the target SL is pulled to ground and the target BL is connected to a sensing voltage V_{SENSE}. To prevent disturbing the state of the desired bit cell, a sensing voltage of 0.2 V was used in our experiments, but the sensing voltage

will be a design parameter taking into account the write voltages and the desired sensing margin for memory.

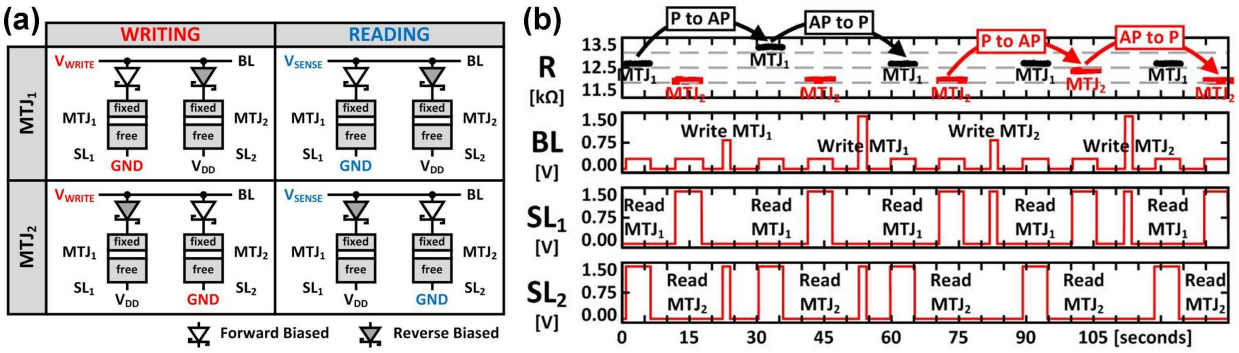

Fig. 5.10 (a) Array configuration for a diode-MTJ architecture, exploiting the unipolar set/reset characteristic of STT-assisted switching. In order write or read the information, the Bit Line (BL) is pulled to V_{WRITE} or V_{SENSE} respectively. At the same time, the selection of the device is done by grounding the desired Source Line (SL) and pulling the undesired to V_{DD}. (b) Measured transient waveforms for reading and writing the array, demonstrating that MTJ_1 can be written with unipolar set/reset voltages (0.5 and 1.1 V, respectively) and read without disturbing MTJ_2 and vice versa. A sensing voltage of 0.2 V in the SL is used for the read process, while unaccessed SLs are pulled to V_{DD} (1.5 V).

Fig. 5.10(b) shows experimental transient waveforms demonstrating the functionality of the small memory array. MTJ_1 and MTJ_2 are first initialized into the P state using an external magnetic field. Then, MTJ_1 is switched from P to AP, then back to P, without disturbing the value of MTJ_2. Similarly, MTJ_2 is also switched from P to AP, then back to P, without disturbing the value of MTJ_1. Switching is preformed using voltage pulses of 0.5 and 1.1 V for a period of 1 second. After writing, both MTJ_1 and MTJ_2 are read 20 times using 0.2 V without disturbing the state of the MTJs in the array.

In summary, we have demonstrated VCMA-driven STT-assisted switching in MeRAM bits, where switching in both directions is obtained for a fixed value of the bias magnetic field.

The unipolar set/reset characteristic of this switching mechanism results in potential architectural advantages, such as the possibility to replace transistors for BEOL diodes as access devices. The BEOL diodes could allow 3D stacking of the memory. Further, this mechanism does not necessarily place a limit on the current drive capability of its access devices, given that it can operate with currents smaller than purely STT-based memory devices. This is in contrast to STT-MRAM, where density is usually limited by the current drive capability (hence, width) of its access transistors. This can confer a potential scalability advantage to MeRAM compared to STT-MRAM.

5.5 Precessional switching

The STT-assisted switching, however, still requires charge currents, which may limit the energy efficiency of the switching. In Chapter 1 and 2, we argued that the advantage of utilizing the VCMA effect is the possibility to eliminate the need for charge current to write the information, making the switching energy competitive to the ones observed for CMOS devices. Therefore, an alternative approach to achieve purely VCMA-driven switching is to perform precessional switching, i.e., completing the magnetization reversal by properly timing the magnetization dynamics of the MTJ device [183]. VCMA-driven precessional switching in MTJ devices was first demonstrated by Shiota, *et al.*, [115] in small resistance devices, with a large contribution from STT effects. Later, the switching mechanism was demonstrated in larger resistance devices, mostly dominated by the VCMA effect [177, 184, 185]. In this section, we demonstrate VCMA-driven switching in our nanoscale MTJ devices, and study the switching results against simulations from our compact model.

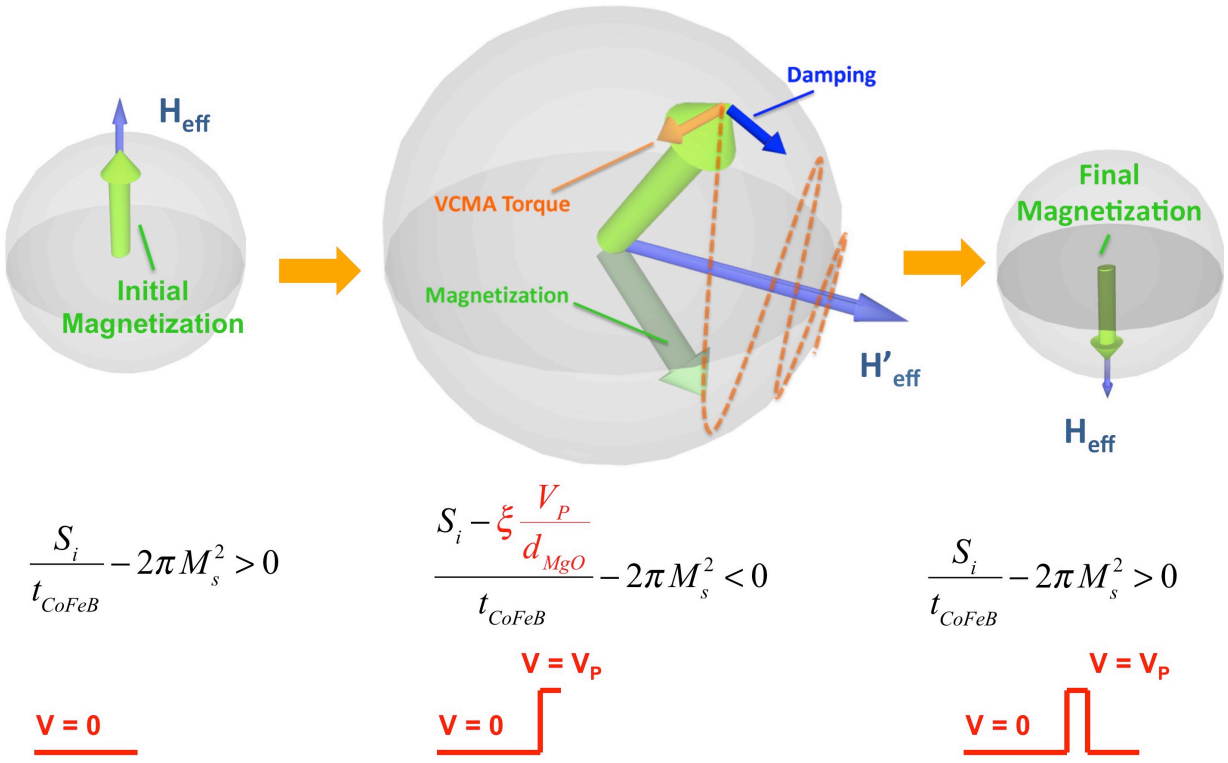

Fig. 5.11 VCMA-controlled precessional switching. In order to achieve VCMA-driven precessional switching, we start with a perpendicular configuration, where the effective perpendicular anisotropy is > 0. After the voltage increases to V_P, the effective perpendicular anisotropy is < 0 and the magnetization will precess towards the in-plane state. By properly timing the pulse, switching can be achieved by removing the voltage once the magnetization is close to the final perpendicular state.

The switching mechanism for VCMA-driven precessional switching in a perpendicular MTJ device is illustrated on Fig. 5.11. In order to achieve switching, a voltage V_P is applied to the MTJ, such that, because of VCMA, the perpendicular anisotropy is reduced and the overall first order anisotropy becomes negative, i.e., from equations (2.12) and (4.7)

$$K_{1,eff}(V_P) = \frac{S_i}{t_{\mathrm{CoFeB}}} - \xi \frac{V_P}{d_{\mathrm{MgO}} t_{\mathrm{CoFeB}}} - 2\pi M_s^2 < 0 \qquad (5.8)$$

Under such condition, the minimum energy state is in the in-plane direction, hence the magnetization will move towards the new equilibrium state by precessing around the in-plane

effective field H'_{eff} . H'_{eff} in the in-plane direction will be composed by the in-plane demagnetization field (very small, see discussion in section 1.4.1) and any applied bias magnetic field. If the voltage pulse is maintained, the magnetization will damp to the in-plane direction, coming back to the situation described in Fig. 5.1. However, if the write pulse is timed such that the pulse is removed when the magnetization precession is crossing near the final magnetization state, after pulse removal, $K_{1,eff}(V=0)>0$, hence the equilibrium states are again in the perpendicular direction and magnetization will damp to the final state, achieving switching. This scheme can also be described in terms of energy wells, as illustrated previously on Fig. 2.6.

This switching scheme can be performed at GHz (i.e., the characteristic time of magnetization precession) with reasonable voltage pulses even with the limited VCMA in Ta|CoFeB|MgO-based MTJs. Also, neither currents nor changes in the bias field are required to achieve switching. However, precessional switching requires very precise timing of the write pulse at multiples of half of the precession (e.g., a full precession cycle will return the magnetization near the initial state). Also, precessional switching does not allow to determine the final state of the magnetization since the magnetization will switch to the opposite state after every write pulse, similar to a toggle scheme. Hence, before writing the information, it is needed to read the state (P or AP) to determine if a write pulse is needed to move the state to the opposite direction or not. Yet, because of the fast writing in precessional switching, it may be possible to perform a read and write process faster than the times required for thermally activated switching. Finally, the speed of the precession is controlled by strength of the in-plane effective field H'_{eff}, specifically

$$t_{precess} = \frac{\pi}{2\gamma H'_{eff}} \tag{5.9}$$

where γ is the gyromagnetic ratio. In a perpendicular MTJ device with circular shape, there is not a preferred direction the *x*-*y* plane (in-plane) due to shape anisotropy, hence there is not a fixed H'_{eff} around which the magnetization can precess. Consequently, VCMA-driven precessional switching requires either to use elliptical MTJs where the shape anisotropy creates an effective field in the in-plane direction (undesired for scalability and density reasons discussed in Chapter 1), or to add an in-plane constant bias field in the material stack such that $H'_{eff} \approx H_{Bias}$ assuming that bias field is much larger than the demagnetization field in the x- or y-direction (hundreds versus tens of Oe, respectively). Note that proper engineering of H'_{eff} is critical since very short precessional times will reduce the write timing window and result in higher error rates, as will be discussed later, meanwhile very long precessional times will make the precession incoherent and it will become randomized by thermal fluctuations [177].

In order to demonstrate VCMA-driven precessional switching in our devices, the MTJ stack shown in Fig. 5.12(a) was patterned into circular 80 × 80 nm^2. The material stack was annealed at 300 °C for 30 minutes without any magnetic field. In the stack design, the [Co/Pd] superlattice acts as a strong perpendicular material, helping to pin the direction of the fixed layer (top CoFeB). A bottom thick CoFeB was introduced in order to serve as an in-plane layer that provides a stray (bias) into the free layer for precession. An MgO layer is grown on top of the bottom CoFeB to help in crystallization of the amorphous CoFeB. However, it also acts as an undesired series resistance, lowering the TMR of the stack. Finally, a 5 nm Ta spacer separates the stray field layer of the free layer, where the thickness of the spacer is one of the critical parameters to engineer the strength of H_{Bias} acting on the free layer. In our experiments, the H_{Bias} provided by the stray field layer had to be adjusted with an external magnetic field to optimize H'_{eff} for precessional switching and was estimated to be on the order of 200- 30Oe;

however, further optimization of the material stack should result in external-magnetic-field-free switching by engineering H_{Bias} into the value optimized for H'_{eff} in the experiments.

Fig. 5.12(b) presents the resistance versus perpendicular magnetic field curves, showing that the TMR of the device is close to 40%. However, if the effect of the series resistance due to the lower MgO is subtracted, our free layer|MgO|fixed layer perpendicular stack has a TMR of 63%. Note that the coercivity of the device utilized for this demonstration is small (~ 50 Oe) since the free layer thickness had to be chosen very close to the compensation point between interfacial anisotropy and demagnetization energy in order to reorient the easy-axis to the in-plane direction with voltages below the MgO breakdown.

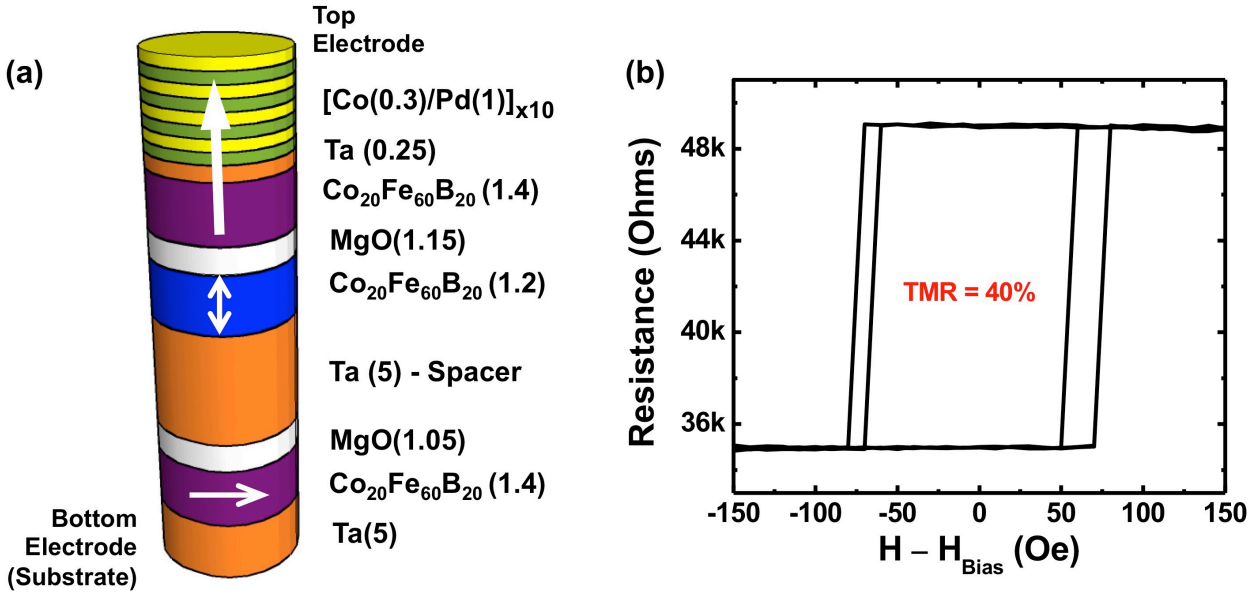

Fig. 5.12 (a) Material stack for the demonstration of VCMA-driven precessional switching. The [Co/Pd] superlattice pins the top CoFeB (fixed layer) in the perpendicular direction, meanwhile the lower CoFeB serves as a stray field layer to provide an in-plane bias field to the free layer. (b) Resistance versus perpendicular magnetic field curve for the device utilized in the demonstration. The coercivity is ~50 Oe, while the TMR, including the series resistance due to the stray field layer MgO, is close to 40%.

The experimental switching probability versus pulse duration curves for VCMA-driven precessional switching are shown on Fig. 5.13(a). The observed oscillation of the switching probability is a key signature of precessional switching. However, it may be observed that such oscillations damp very quickly, possibly indicating a very high effective damping for the free layer dynamics during switching. We are able to obtain ~100% switching probability in a time window ~ 700 ± 250 ps on the first peak of the switching probability by using a voltage pulse of 1.9 V, validating the possibility to use VCMA-driven precessional switching to write the information into MeRAM memory bits. Also, note that there is an unexpected difference between the P to AP and AP to P switching curves, where the probability does not settle at 50%; 50% switching probability is expected for long pulses as seen in Fig. 5.1. The discrepancy may be explained by either the presence of a small stay field from the fixed layer that favors one of the perpendicular states in the free layer, or by field-like-torque from the leakage current, where field-like torque behaves as a current-controlled bias field and therefore, higher resistance MTJ devices are needed to reduce field-like torque and the contribution to the energy from undesired leakage currents.

A key metric for memory devices is the write error rate (WER), defined as $WER = 1 - P_{sw}$, where P_{sw} is the switching probability. It is desired to have memory devices with low WER, in the range where the error correction coding (ECC) of the system can correct for the failed write events. Usually, WER on the order of 10^{-6} – 10^{-10} are sought, depending on the application and on the size of the memory array [186]. Fig. 5.13(b) shows the WER measured in our samples for the first peak of the probability by using 1000 trials per point. For the first demonstration, we have obtained WER on the order 10^{-2}; however, the statistical noise is on the same order taking into account the relative small number of trials. Therefore, the real WER may be smaller than

10^{-2} and it is proposed as future work to implement methodology different than our testing circuit in Fig. 5.3(a) to measure low WER in acceptable experimental times.

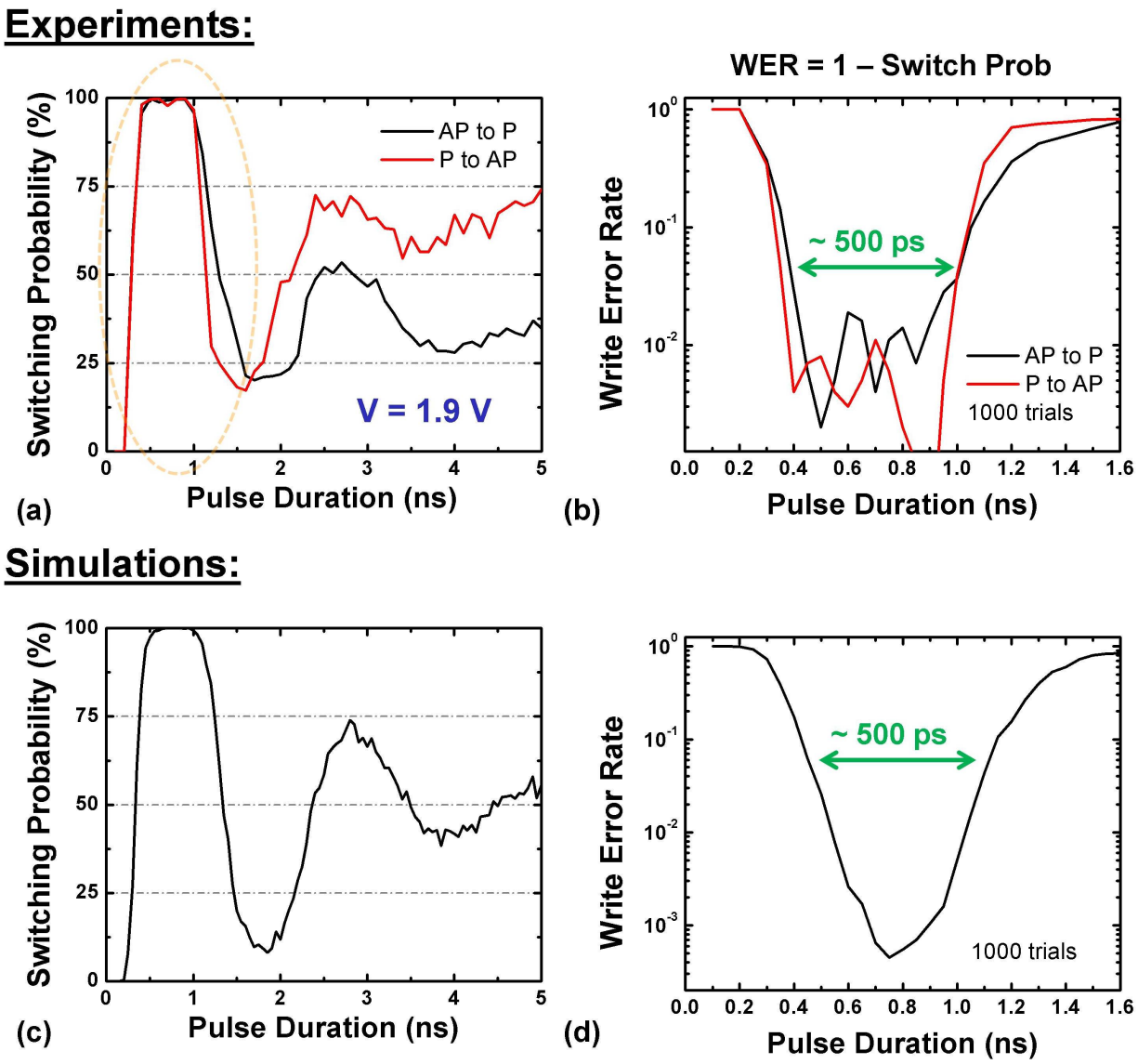

Fig. 5.13 Experiments: (a) Switching probability versus pulse duration for a voltage pulse of 1.9 V. The plot demonstrates VCMA-driven precessional switching in nanoscale MTJ devices. (b) The minimum write error rate (WER) has measured to be ~10^{-2}, however the limited number of trials gives rise to the statistical noise of comparable size. Simulations: (c) The experimental switching probability curve can be well reproduced with simulations. A large damping is predicted to reproduce the data. (d) The minimum WER in simulation is observed to be $10^{-3.5}$, which can be explained by large effective damping during magnetization reversal. Hence, reduction of the effective damping is required to lower the WER.

In order to validate the experimental results, we performed simulations using the compact model presented in section 2.6. The parameter space was optimized to reproduce the experimental data. Fig. 5.13(c) shows the switching probability versus pulse duration curves in simulations with 1000 trials per point, where we obtain a good match against experimental data. In order to reproduce the experimental observations, a large damping constant of $\alpha = 0.27$ (i.e., one order of magnitude larger than the measured damping from small signal excitations [173]) was needed, explaining the reduced number of oscillations in the experimental switching probability curves. Such large effective damping may be related to the micromagnetism of the switching process, where a small sub-volume excitation may be responsible for the reversal process; that is, such sub-volume is subjected to a strong pinning from the edges of the MTJ, effectively increasing the damping during the switching process [177]. Also, an in-plane bias field of $H_{Bias} = 230$ Oe was predicted from the model, which should be possible to obtain in the material stack of Fig. 5.12(a) by optimizing the thickness of the in-plane CoFeB stray field layer and the thickness of the Ta spacer.

Fig. 5.13(d) shows the WER from simulations, where we observe a minimum write error rate of 5×10^{-4}. The WER is observed in simulations to be mostly limited by the large effective damping, hence the minimum WER can be lowered below 10^{-5} by reducing the effective damping to 0.1. A lower effective damping may be possible by using smaller nanoscale MTJ devices, making subvolume excitations more energy costly. Specifically, if the device size is smaller than the domain wall width for the material, a domain wall cannot be localized into the free layer of the device; hence, single domain behavior is preferred over the formation of texture as the device scales down [81]. Once single-domain-like behavior is assured, coherent precessions of the magnetization will be preferred (over the formation of sub-volume excitations),

and the value effective damping is expected to decrease down to the nominal small signal values ($\alpha \sim 0.02$ for CoFeB). However, scaling to smaller MTJ may also require larger VCMA coefficients, as discussed in section 2.4. An alternative strategy verified in simulations is to reduce the bias field and slow down the center of the first peak of the switching probability to 1-1.5 ns. Going beyond 2 ns results in larger WER due to incoherent precession of the magnetization and randomization due to thermal fluctuations.

To conclude this study, we measure the thermal stability of the memory bit using the dwell time method utilized previously in section 5.3. Fig. 5.14 shows the dependence of the dwell time on the applied perpendicular magnetic field. In good agreement to the small coercivity in the R-H loop of Fig. 5.12(b), the extrapolated dwell time for the stand-by condition ($H - H_{\text{offset}} = 0$) is ~ 19 minutes for AP state (Δ_{AP} = 27.8, in black on Fig. 5.14) and ~ 36 hours for the P state (Δ_P = 32.5, in red on Fig. 5.14). Hence, the devices used in this demonstration of VCMA-driven precessional switching could be used as MeRAM memory bits in applications where relatively short retention times are acceptable, such as cache or working memories.

Beyond reducing the WER in the memory bits presented in this section, there are other challenges that need to be addressed to make this demonstration practical: First, the current switching voltage is too high (1.9 V), operating very close to the breakdown voltage of the MgO, thus significantly reducing the endurance of the memory. Therefore, increasing the VCMA effect by 2x-3x (e.g., from 40 to 120 fJ/V-m) is required in order to reduce the write voltages below 1 V. Similarly, if longer retention times are required for other applications in MeRAM, increasing the interfacial perpendicular anisotropy would be required, hence requiring larger VCMA coefficients to compensate for the increase in the interfacial anisotropy. Of all switching mechanisms, the precessional one requires the largest voltage since the VCMA effect needs to

fully destroy the energy barrier and rotate the easy-axis for the magnetization. Thus, the scaling rules outlined in section 2.4 would have to be rigorously followed to avoid an increase in the write voltage as the voltage is scaled down. However, the proof of concept here demonstrated is very promising, indicating the potential for precessional switching to reach energies below 10 fJ (and even close to 1 fJ) due to the relatively fast write (0.7-1 ns) and the possibility to further reduce the undesired leakage currents, which are not needed in this switching mechanism.

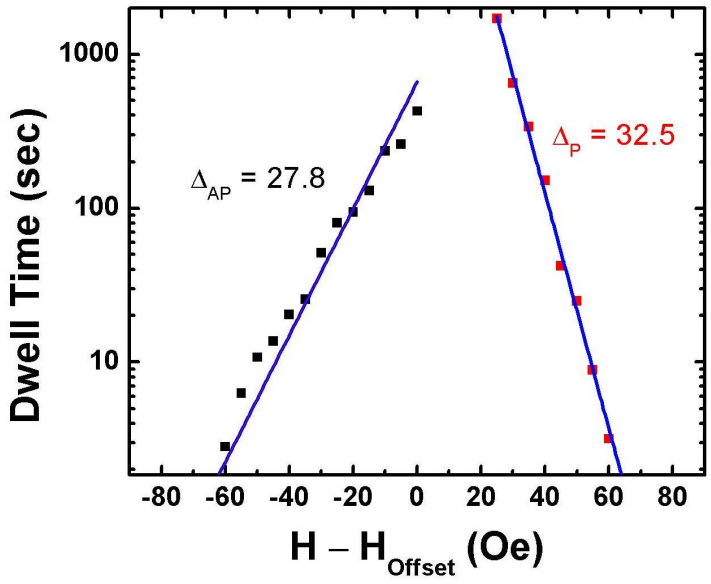

Fig. 5.14 Measurements of the dwell time for the parallel (P, in red) and antiparallel (AP, in black) states in the devices used for the demonstration of VCMA-driven precessional switching. The current devices show a relatively short retention time, on the order of a few minutes for the AP state, and on the order of 1 day for the P state. Hence, these memory bits would be limited to applications where short retention times are acceptable, or further increase of the interfacial anisotropy and the VCMA coefficient would be needed.

5.6 Combined thermally-activated/precessional switching with canted states

We conclude this chapter by introducing the last switching mechanism, which we have only observed in devices where higher order anisotropy contributions lead to canting of the

magnetization (see Chapter 4). The presence of angled magnetization allows for applying bias fields that break the symmetry for the two equilibrium states with respect to the VCMA effect [187], and permits the control of the direction of the switching, addressing one of the undesired features of the precessional switching scheme discussed in the previous section.

Fig. 5.15 explains schematically how switching is achieved in this scheme. At equilibrium and without any bias field, the canted states will have the same *z*-component of the magnetization. However, if an angled H_{Bias} is used, the equilibrium states will rotate accordingly to Fig. 5.15, where the resulting states will have different z-components and also, different resistance values, which we use to label the states as low-resistance (LR) and high-resistance (HR), respectively. In section 2.6, the effective VCMA torque was calculated to be $\vec{\tau}_{VCMA} \propto \vec{m} \times \vec{H}_{VCMA} \propto m_z V\left(\vec{m} \times \hat{z}\right)$. Hence, the torque vanishes at the perpendicular ($\vec{m} \times \hat{z} = 0$) and at the in-plane ($m_z = 0$) directions, while having a maximum value for intermediate values between such extremes. Given that the angles bias field results in two different z-components for the LR and HR states, such states will experience different VCMA torques. In the particular case of Fig. 5.15, the state LR has $m_z \sim 1$, hence the VCMA torque is small, meanwhile the HR state has $m_z \sim -0.2$ with a larger VCMA torque. Consequently, the switching mechanism can be explained as follows: For HR to LR switching, the bias field is such that, because of the angle of HR, the effective VCMA torque will be larger, hence allowing for precessional switching (Fig. 5.15(a)). Note that, contrary to the situation in the last section, in this case the opposite precessional switching (e.g, LR to HR) would not be possible due to the smaller effective VCMA torque. In order to switch from LR to HR, the bias field is set such that it favors the HR state. Hence, once the voltage is applied, the energy barrier between the two states will be lowered and the magnetization will switch to the favored HR state (Fig. 5.15(b)).

Fig. 5.15(c) shows switching probability versus pulse duration curves, demonstrating the concept. Precessional switching is obtained with a voltage of 2.6 V, with a maximum probability ~100% at 0.6-0.7 ns. On the other hand a long pulse (t > 10 ns) of 1.5 V will result in thermally activated switching for the opposite direction. In conclusion, switching can be obtained in the nanosecond regime with selection of the switching direction and also, no charge currents are required for this scheme (i.e., purely VCMA-driven switching scheme). However, the usage of canted states results in a penalty of reduced effective TMR. Also, in the present demonstration, the WER are large, therefore, further optimization of the device is needed to reduce the WER.

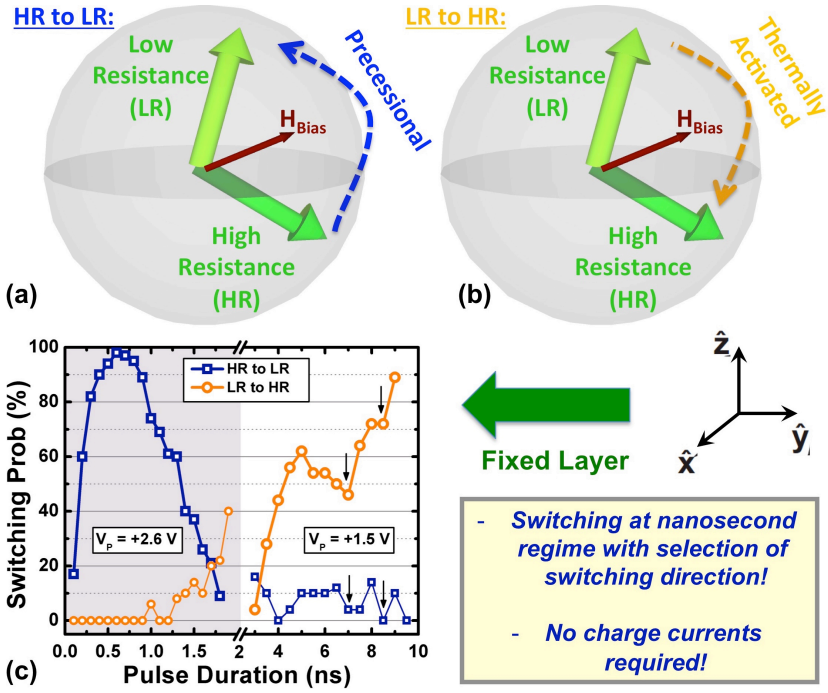

Fig. 5.15 Combined thermally activated and precessional switching. (a) Switching from the high resistance (HR) to the low resistance (LR) state is achieved due to the larger effective VCMA torque experienced by the HR state. The LR state has a magnetization state much closer to the perpendicular direction, decreasing the effective VCMA torque, hence breaking the toggle characteristic of precessional switching. (b) Switching from LR to HR is due to the thermal activation. The Bias field is set to favor the HR state, therefore when the voltage is applied, the magnetization will fall to HR. (c) Experimental switching probability curves demonstrating the combined precessional/thermally-activated switching scheme. The switching direction is set by the magnitude and duration of the write pulse utilized.

CHAPTER 6: Conclusions

The end of CMOS scaling has been predicted in multiple occasions throughout the last decades, but so far, engineers and scientist in the area have found their way around to keep pushing CMOS to its ultimate limits, creating innovative architectural and processing solutions to revamp the transistor at every new technology node. However, it seems that the end of the classical CMOS scaling is indeed finally coming, driven by the physical limits imposed in a transistor where the number of atoms in the gate can be actually counted. At least classical CMOS scaling, understood as an economics law, has been broken already since for the last technology nodes, the price per transistor started to increase instead of the decreasing trend predicted by Moore [139, 140]. In this challenging context, the same engineers and scientist are starting to look for beyond CMOS devices, exploring novel physical phenomena in nature that can help to maintain the continuous improvement of electronics.

One of the approaches for beyond CMOS is exploiting the magnetic properties of materials. Magnetism lived for very long separated from the world of electronics, only partially connected via hard-disk technology. Yet, spintronics has become in the last years one of the strongest candidates for beyond CMOS computation because of the combination of magnetic and electronic properties. In Chapter 1 of this work, we introduced the concept of spintronics and focused on how magnetism can help to alleviate one of the most energy-draining problems of scaled CMOS: The exponential increase in stand-by (static) power. We described how the integration of spin-based devices with CMOS may lead to zero stand-by power, allowing for the possibility of non-volatile computation with instant-on capabilities.

As one of the most promising spin-based devices, in Chapter 1 we introduced the magnetic tunnel junctions (MTJs) and their role into the Magnetic Random Access Memory (MRAM). MTJs have great advantages, as described throughout Chapter 1, and they are currently reaching the market via STT-MRAM technology, where spin-polarized currents are used to control the device. However, we also mentioned the limitations of spin-torque, including issues in terms of energy efficiency, scalability and density. Therefore, we claim that replacing STT for a voltage-controlled mechanism may alleviate these issues.

The voltage-controlled magnetic anisotropy (VCMA) effect was introduced in Chapter 2 as a possible mechanism for electric-field-control of magnetism. The VCMA effect is of considerable practical use since it can be easily integrated into MRAM technology. However, it is currently a rather small effect, with an energy efficiency of less than 1%. The physical mechanisms for VCMA were studied and we identified the need to discover materials with higher VCMA coefficients. In particular, the conversion between electric fields and magnetic anisotropy was understood via spin-orbit-coupling (SOC), and therefore the discovery of a 4f ferromagnetic material with larger SOC while having a large TMR ratio for read-out would be a possible avenue to enhance effects such as the VCMA. Nevertheless, in Chapter 2 we identified the potential advantages of using VCMA for a future magnetoelectric MeRAM architecture with improved metrics in terms of energy efficiency, density and scalability.

The lack of material systems with a large TMR ratio is one of the key limitations of current spintronics technology. Therefore, this dissertation focused on Ta|CoFeB|MgO system, with one of the highest signal to noise ratios for read-out, and performed a detailed characterization of the VCMA effect in such system. In Chapter 3, we studied the temperature dependence of the interfacial perpendicular anisotropy and the VCMA coefficient, finding that

the perpendicular anisotropy energy and the VCMA coefficient follow different power laws of the magnetization saturation. We argued this result could be understood in both the context of the orbitals and the Rashba contributions to VCMA, where the applied voltage modulates only part of the perpendicular anisotropy.

In Chapter 4, we studied in detail the higher order contributions to the perpendicular anisotropy and the VCMA effect. We argued that the difference in the angular dependence of the higher order contributions requires careful characterization of the higher order coefficients. We found that, even though the second order anisotropy is at least one order of magnitude smaller, the VCMA coefficient due to the second order anisotropy is of comparable strength to the first order contribution, where the two quantities tend to cancel each other. Future studies will be required to understand the physics behind the desired results on the higher order contribution.

Further, one of the main results of this dissertation was the demonstration that the VCMA effect can be used to induce electric-field-driven switching of nanoscale MTJ devices with a large TMR ratio for read-out. The VCMA effect suffers from a fundamental limitation for 180° degree switching of the magnetization, since VCMA is only able to re-direct the magnetic easy-axis, i.e., only 90° degree rotation can be achieved. Throughout Chapter 5 we explored four different possible mechanisms to address this issue, including field-assisted, STT-assisted, precessional switching and combined thermally-activated/precessional in canted states. We demonstrated that STT-assisted switching results in a unipolar set/reset scheme that allows to use diodes a access devices. Additionally, we showed VCMA-driven precessional switching of nanoscale MTJ devices with potential switching energies below 10 fJ/switch. Finally, we proved that the proposed schemes could be the used in a real MeRAM architecture, and yet, as novel phenomena for voltage-control of magnetism emerge, novel mechanisms will be also sought.

References

[1] S. Borkar, "Electronics beyond nano-scale CMOS," in *Proceedings of the 43rd ACM/IEEE Design Automation Conference*, 2006, pp. 807-808.

[2] K. Bernstein, R. K. Cavin, W. Porod, A. Seabaugh, and J. Welser, "Device and Architecture Outlook for Beyond CMOS Switches," *Proceedings of the IEEE,* vol. 98, pp. 2169-2184, 2010.

[3] G. E. Moore, "Cramming more components onto integrated circuits," *Electronics Magazine,* vol. 38, 1965.

[4] M. Mayberry. (2010). *Emerging Technologies and Moore's Law: Prospects for the Future*. Available: http://www.nist.gov/pml/div683/upload/Mayberry_March_2010.pdf

[5] K. J. Kuhn, "Considerations for Ultimate CMOS Scaling," *IEEE Transactions on Electron Devices,* vol. 59, pp. 1813-1828, 2012.

[6] E. J. Nowak, T. Ludwig, I. Aller, J. Kedzierski, M. Leong, B. Rainey, M. Breitwisch, V. Gemhoefer, J. Keinert, and D. M. Fried, "Scaling beyond the 65 nm node with FinFET-DGCMOS," in *Proceedings of the IEEE Custom Integrated Circuits Conference*, 2003, pp. 339-342.

[7] K. L. Wang, J. G. Alzate, and P. K. Amiri, "Low-power non-volatile spintronic memory: STT-RAM and beyond," *Journal of Physics D: Applied Physics,* vol. 46, p. 074003, 2013.

[8] M. Bohr, "The evolution of scaling from the homogeneous era to the heterogeneous era," in *IEEE International Electron Devices Meeting (IEDM)*, 2011, pp. 1.1.1-1.1.6.

[9] J. Stöhr and H. C. Siegmann, *Magnetism: from fundamentals to nanoscale dynamics*: Springer, 2007.

[10] P. Grünberg, R. Schreiber, Y. Pang, M. B. Brodsky, and H. Sowers, "Layered Magnetic Structures: Evidence for Antiferromagnetic Coupling of Fe Layers across Cr Interlayers," *Physical Review Letters,* vol. 57, pp. 2442-2445, 1986.

[11] M. N. Baibich, J. M. Broto, A. Fert, F. N. Van Dau, F. Petroff, P. Etienne, G. Creuzet, A. Friederich, and J. Chazelas, "Giant Magnetoresistance of (001)Fe/(001)Cr Magnetic Superlattices," *Physical Review Letters,* vol. 61, pp. 2472-2475, 1988.

[12] K. L. Wang and P. K. Amiri, "Nonvolatile Spintronics: Perspectives on Instant-on Nonvolatile Nanoelectronic Systems," *Spin,* vol. 02, p. 1250009, 2012.

[13] A. Khitun and K. L. Wang, "Nano scale computational architectures with Spin Wave Bus," *Superlattices and Microstructures,* vol. 38, pp. 184-200, 9// 2005.

[14] S. A. Wolf, D. D. Awschalom, R. A. Buhrman, J. M. Daughton, S. von Molnár, M. L. Roukes, A. Y. Chtchelkanova, and D. M. Treger, "Spintronics: A Spin-Based Electronics Vision for the Future," *Science,* vol. 294, pp. 1488-1495, November 16, 2001 2001.

[15] A. Khitun, M. Bao, and K. L. Wang, "Spin Wave Magnetic NanoFabric: A New Approach to Spin-Based Logic Circuitry," *IEEE Transactions on Magnetics,* vol. 44, pp. 2141-2152, 2008.

[16] J. G. Alzate, P. Upadhyaya, M. Lewis, J. Nath, Y. T. Lin, K. Wong, S. Cherepov, P. K. Amiri, K. L. Wang, J. Hockel, A. Bur, G. P. Carman, S. Bender, Y. Tserkovnyak, J. Zhu, Y. J. Chen, I. N. Krivorotov, J. Katine, J. Langer, P. Shabadi, S. Khasanvis, S. Narayanan, C. A. Moritz, and A. Khitun, "Spin wave nanofabric update," in *2012 IEEE/ACM International Symposium on Nanoscale Architectures (NANOARCH)*, 2012, pp. 196-202.

[17] S. Datta and B. Das, "Electronic analog of the electro-optic modulator," *Applied Physics Letters,* vol. 56, pp. 665-667, 1990.

[18] C.-X. Liu, X.-L. Qi, X. Dai, Z. Fang, and S.-C. Zhang, "Quantum anomalous hall effect in Hg 1-y Mn y Te quantum wells," *Physical Review Letters,* vol. 101, p. 146802, 2008.

[19] X.-L. Qi and S.-C. Zhang, "Topological insulators and superconductors," *Reviews of Modern Physics,* vol. 83, pp. 1057-1110, 2011.

[20] J. E. Moore, "The birth of topological insulators," *Nature,* vol. 464, pp. 194-198, 2010.

[21] E. Y. Tsymbal and I. Zutic, *Handbook of spin transport and magnetism*: CRC press, 2011.

[22] Y. Tserkovnyak, A. Brataas, and G. E. W. Bauer, "Enhanced Gilbert Damping in Thin Ferromagnetic Films," *Physical Review Letters,* vol. 88, p. 117601, 2002.

[23] E. Saitoh, M. Ueda, H. Miyajima, and G. Tatara, "Conversion of spin current into charge current at room temperature: Inverse spin-Hall effect," *Applied Physics Letters,* vol. 88, pp. -, 2006.

[24] T. Shinjo, *Nanomagnetism and spintronics*: Elsevier, 2013.

[25] P. P. Freitas, R. Ferreira, S. Cardoso, and F. Cardoso, "Magnetoresistive sensors," *Journal of Physics: Condensed Matter,* vol. 19, p. 165221, 2007.

[26] S. S. P. Parkin, C. Kaiser, A. Panchula, P. M. Rice, B. Hughes, M. Samant, and S.-H. Yang, "Giant tunnelling magnetoresistance at room temperature with MgO (100) tunnel barriers," *Nat Mater,* vol. 3, pp. 862-867, 2004.

[27] S. Yuasa, T. Nagahama, A. Fukushima, Y. Suzuki, and K. Ando, "Giant room-temperature magnetoresistance in single-crystal Fe/MgO/Fe magnetic tunnel junctions," *Nat Mater,* vol. 3, pp. 868-871, 2004.

[28] S. D. Bader and S. S. P. Parkin, "Spintronics," *Annual Review of Condensed Matter Physics,* vol. 1, pp. 71-88, 2010.

[29] I. Žutić, J. Fabian, and S. Das Sarma, "Spintronics: Fundamentals and applications," *Reviews of Modern Physics,* vol. 76, pp. 323-410, 2004.

[30] G. E. W. Bauer, E. Saitoh, and B. J. van Wees, "Spin caloritronics," *Nat Mater,* vol. 11, pp. 391-399, 2012.

[31] F. Xiu, Y. Wang, J. Kim, A. Hong, J. Tang, A. P. Jacob, J. Zou, and K. L. Wang, "Electric-field-controlled ferromagnetism in high-Curie-temperature Mn0.05Ge0.95 quantum dots," *Nat Mater,* vol. 9, pp. 337-344, 2010.

[32] J. C. Slonczewski, "Current-driven excitation of magnetic multilayers," *Journal of Magnetism and Magnetic Materials,* vol. 159, pp. L1-L7, 1996.

[33] L. Berger, "Emission of spin waves by a magnetic multilayer traversed by a current," *Physical Review B,* vol. 54, pp. 9353-9358, 1996.

[34] D. C. Ralph and M. D. Stiles, "Spin transfer torques," *Journal of Magnetism and Magnetic Materials,* vol. 320, pp. 1190-1216, 2008.

[35] J. A. Katine and E. E. Fullerton, "Device implications of spin-transfer torques," *Journal of Magnetism and Magnetic Materials,* vol. 320, pp. 1217-1226, 2008.

[36] P. K. Amiri, Z. M. Zeng, P. Upadhyaya, G. Rowlands, H. Zhao, I. N. Krivorotov, J. P. Wang, H. W. Jiang, J. A. Katine, and J. Langer, "Low write-energy magnetic tunnel junctions for high-speed spin-transfer-torque MRAM," *Electron Device Letters, IEEE,* vol. 32, pp. 57-59, 2011.

[37] L. Liu, C.-F. Pai, Y. Li, H. W. Tseng, D. C. Ralph, and R. A. Buhrman, "Spin-Torque Switching with the Giant Spin Hall Effect of Tantalum," *Science,* vol. 336, pp. 555-558, 2012.

[38] Y. Fan, P. Upadhyaya, X. Kou, M. Lang, S. Takei, Z. Wang, J. Tang, L. He, L.-T. Chang, M. Montazeri, G. Yu, W. Jiang, T. Nie, R. N. Schwartz, Y. Tserkovnyak, and K. L. Wang, "Magnetization switching through giant spin–orbit torque in a magnetically doped topological insulator heterostructure," *Nat Mater,* vol. 13, pp. 699-704, 2014.

[39] P. Khalili Amiri and K. L. Wang, "Voltage-Controlled Magnetic Anisotropy in Spintronic Devices," *SPIN,* vol. 02, p. 1240002, 2012.

[40] C.-G. Duan, S. S. Jaswal, and E. Y. Tsymbal, "Predicted Magnetoelectric Effect in Fe/BaTiO3 Multilayers: Ferroelectric Control of Magnetism," *Physical Review Letters,* vol. 97, p. 047201, 2006.

[41] M. Weisheit, S. Fähler, A. Marty, Y. Souche, C. Poinsignon, and D. Givord, "Electric Field-Induced Modification of Magnetism in Thin-Film Ferromagnets," *Science,* vol. 315, pp. 349-351, 2007.

[42] T. Maruyama, Y. Shiota, T. Nozaki, K. Ohta, N. Toda, M. Mizuguchi, A. A. Tulapurkar, T. Shinjo, M. Shiraishi, S. Mizukami, Y. Ando, and Y. Suzuki, "Large voltage-induced magnetic anisotropy change in a few atomic layers of iron," *Nat Nano,* vol. 4, pp. 158-161, 2009.

[43] S. E. Barnes, J. i. Ieda, and S. Maekawa, "Rashba Spin-Orbit Anisotropy and the Electric Field Control of Magnetism," *Sci. Rep.,* vol. 4, 2014.

[44] C. J. Lin, S. H. Kang, Y. J. Wang, K. Lee, X. Zhu, W. C. Chen, X. Li, W. N. Hsu, Y. C. Kao, M. T. Liu, W. C. Chen, L. YiChing, M. Nowak, N. Yu, and T. Luan, "45nm low power CMOS logic compatible embedded STT MRAM utilizing a reverse-connection 1T/1MTJ cell," in *2009 IEEE International Electron Devices Meeting (IEDM)*, 2009, pp. 1-4.

[45] M. Julliere, "Tunneling between ferromagnetic films," *Physics Letters A,* vol. 54, pp. 225-226, 1975.

[46] J. S. Moodera, L. R. Kinder, T. M. Wong, and R. Meservey, "Large Magnetoresistance at Room Temperature in Ferromagnetic Thin Film Tunnel Junctions," *Physical Review Letters,* vol. 74, pp. 3273-3276, 1995.

[47] T. Miyazaki and N. Tezuka, "Giant magnetic tunneling effect in Fe/Al2O3/Fe junction," *Journal of Magnetism and Magnetic Materials,* vol. 139, pp. L231-L234, 1995.

[48] C. Chappert, A. Fert, and F. N. Van Dau, "The emergence of spin electronics in data storage," *Nat Mater,* vol. 6, pp. 813-823, 2007.

[49] S. Yuasa and D. D. Djayaprawira, "Giant tunnel magnetoresistance in magnetic tunnel junctions with a crystalline MgO(0 0 1) barrier," *Journal of Physics D: Applied Physics,* vol. 40, p. R337, 2007.

[50] W. H. Butler, X. G. Zhang, T. C. Schulthess, and J. M. MacLaren, "Spin-dependent tunneling conductance of Fe|MgO|Fe sandwiches," *Physical Review B,* vol. 63, p. 054416, 2001.

[51] J. Mathon and A. Umerski, "Theory of tunneling magnetoresistance of an epitaxial Fe/MgO/Fe(001) junction," *Physical Review B,* vol. 63, p. 220403, 2001.

[52] S. Ikeda, J. Hayakawa, Y. Ashizawa, Y. M. Lee, K. Miura, H. Hasegawa, M. Tsunoda, F. Matsukura, and H. Ohno, "Tunnel magnetoresistance of 604% at 300K by suppression of Ta diffusion in CoFeB/MgO/CoFeB pseudo-spin-valves annealed at high temperature," *Applied Physics Letters,* vol. 93, pp. -, 2008.

[53] S. Ikeda, H. Sato, M. Yamanouchi, H. Gan, K. Miura, K. Mizunuma, S. Kanai, S. Fukami, F. Matsukura, N. Kasai, and H. Ohno, "Recent Progress of Perpendicular Anisotropy Magnetic Tunnel Junctions For Nonvolatile VLSI," *SPIN,* vol. 02, p. 1240003, 2012.

[54] D. D. Tang and Y.-J. Lee, *Magnetic memory: fundamentals and technology*: Cambridge University Press, 2010.

[55] J. G. Alzate, P. Khalili Amiri, G. Yu, P. Upadhyaya, J. A. Katine, J. Langer, B. Ocker, I. N. Krivorotov, and K. L. Wang, "Temperature dependence of the voltage-controlled perpendicular anisotropy in nanoscale MgO|CoFeB|Ta magnetic tunnel junctions," *Applied Physics Letters,* vol. 104, p. 112410, 2014.

[56] E. Chen, D. Apalkov, Z. Diao, A. Driskill-Smith, D. Druist, D. Lottis, V. Nikitin, X. Tang, S. Watts, S. Wang, S. A. Wolf, A. W. Ghosh, J. W. Lu, S. J. Poon, M. Stan, W. H. Butler, S. Gupta, C. K. A. Mewes, T. Mewes, and P. B. Visscher, "Advances and Future Prospects of Spin-Transfer Torque Random Access Memory," *IEEE Transactions on Magnetics,* vol. 46, pp. 1873-1878, 2010.

[57] A. Driskill-Smith, D. Apalkov, V. Nikitin, X. Tang, S. Watts, D. Lottis, K. Moon, A. Khvalkovskiy, R. Kawakami, X. Luo, A. Ong, E. Chen, and M. Krounbi, "Latest Advances and Roadmap for In-Plane and Perpendicular STT-RAM," in *3rd IEEE International Memory Workshop (IMW)*, 2011, pp. 1-3.

[58] D. Apalkov, S. Watts, A. Driskill-Smith, E. Chen, Z. Diao, and V. Nikitin, "Comparison of Scaling of In-Plane and Perpendicular Spin Transfer Switching Technologies by Micromagnetic Simulation," *IEEE Transactions on Magnetics,* vol. 46, pp. 2240-2243, 2010.

[59] R. Sbiaa, H. Meng, and S. N. Piramanayagam, "Materials with perpendicular magnetic anisotropy for magnetic random access memory," *physica status solidi (RRL) – Rapid Research Letters,* vol. 5, pp. 413-419, 2011.

[60] B. Wang, H. Oomiya, A. Arakawa, T. Hasegawa, and S. Ishio, "Perpendicular magnetic anisotropy and magnetization of L10 FePt/FeCo bilayer films," *Journal of Applied Physics,* vol. 115, p. 133908, 2014.

[61] S. Ikeda, K. Miura, H. Yamamoto, K. Mizunuma, H. D. Gan, M. Endo, S. Kanai, J. Hayakawa, F. Matsukura, and H. Ohno, "A perpendicular-anisotropy CoFeB–MgO magnetic tunnel junction," *Nat Mater,* vol. 9, pp. 721-724, 2010.

[62] Y. Huai, "Spin-Transfer Torque MRAM (STT-MRAM): Challenges and Prospects," *AAPPS Bulletin,* vol. 18, pp. 33-40, 2008.

[63] K. Zhang, *Embedded memories for nano-scale VLSIs* vol. 2: Springer, 2009.

[64] "International Technology Roadmap for Semiconductors (ITRS)," 2011-2012.

[65] K. L. Wang, I. Ovchinnikov, F. X. Xiu, A. Khitun, and M. Bao, "From Nanoelectronics to Nano-Spintronics," *Journal of Nanoscience and Nanotechnology,* vol. 11, pp. 306-313, 2011.

[66] R. Dorrance, R. Fengbo, Y. Toriyama, A. A. Hafez, C. K. K. Yang, and D. Markovic, "Scalability and Design-Space Analysis of a 1T-1MTJ Memory Cell for STT-RAMs," *Electron Devices, IEEE Transactions on,* vol. 59, pp. 878-887, 2012.

[67] J. Z. Sun, "Spin-current interaction with a monodomain magnetic body: A model study," *Physical Review B,* vol. 62, pp. 570-578, 2000.

[68] G. E. Rowlands, T. Rahman, J. A. Katine, J. Langer, A. Lyle, H. Zhao, J. G. Alzate, A. A. Kovalev, Y. Tserkovnyak, Z. M. Zeng, H. W. Jiang, K. Galatsis, Y. M. Huai, P. K. Amiri, K. L. Wang, I. N. Krivorotov, and J. P. Wang, "Deep subnanosecond spin torque switching in magnetic tunnel junctions with combined in-plane and perpendicular polarizers," *Applied Physics Letters,* vol. 98, Mar 7 2011.

[69] A. D. Kent, B. Ozyilmaz, and E. del Barco, "Spin-transfer-induced precessional magnetization reversal," *Applied Physics Letters,* vol. 84, pp. 3897-3899, May 10 2004.

[70] H. Liu, D. Bedau, D. Backes, J. A. Katine, J. Langer, and A. D. Kent, "Ultrafast switching in magnetic tunnel junction based orthogonal spin transfer devices," *Applied Physics Letters,* vol. 97, Dec 13 2010.

[71] J. G. Alzate, "Micromagnetic States of Magnetic Tunnel Junction Memory Cells with Perpendicular Polarizer," Thesis for Master of Science in Electrical Engineering, UCLA, 2011.

[72] O. J. Lee, D. C. Ralph, and R. A. Buhrman, "Spin-torque-driven ballistic precessional switching with 50 ps impulses," *Applied Physics Letters,* vol. 99, 2011.

[73] Z. M. Zeng, P. K. Amiri, G. Rowlands, H. Zhao, I. N. Krivorotov, J. P. Wang, J. A. Katine, J. Langer, K. Galatsis, K. L. Wang, and H. W. Jiang, "Effect of resistance-area product on spin-transfer switching in MgO-based magnetic tunnel junction memory cells," *Applied Physics Letters,* vol. 98, 2011.

[74] L. Q. Liu, T. Moriyama, D. C. Ralph, and R. A. Buhrman, "Reduction of the spin-torque critical current by partially canceling the free layer demagnetization field," *Applied Physics Letters,* vol. 94, 2009.

[75] P. K. Amiri, Z. M. Zeng, J. Langer, H. Zhao, G. Rowlands, Y. J. Chen, I. N. Krivorotov, J. P. Wang, H. W. Jiang, J. A. Katine, Y. Huai, K. Galatsis, and K. L. Wang, "Switching current reduction using perpendicular anisotropy in CoFeB-MgO magnetic tunnel junctions," *Applied Physics Letters,* vol. 98, p. 112507, 2011.

[76] M. T. Rahman, A. Lyle, P. K. Amiri, J. Harms, B. Glass, H. Zhao, G. Rowlands, J. A. Katine, J. Langer, I. N. Krivorotov, K. L. Wang, and J. P. Wang, "Reduction of switching current density in perpendicular magnetic tunnel junctions by tuning the anisotropy of the CoFeB free layer," *Journal of Applied Physics,* vol. 111, p. 07C907, 2012.

[77] D. C. Worledge, G. Hu, D. W. Abraham, J. Z. Sun, P. L. Trouilloud, J. Nowak, S. Brown, M. C. Gaidis, E. J. O'Sullivan, and R. P. Robertazzi, "Spin torque switching of perpendicular Ta vertical bar CoFeB vertical bar MgO-based magnetic tunnel junctions," *Applied Physics Letters,* vol. 98, p. 022501, 2011.

[78] J. Kim, H. Zhao, Y. Jiang, A. Klemm, J.-P. Wang, and C. H. Kim, "Scaling Analysis of In-plane and Perpendicular Anisotropy Magnetic Tunnel Junctions Using a Physics-Based Model," in *Device Research Conference (DRC)*, 2014.

[79] NIMO. (2012). *Predictive Technology Model*. Available: http://ptm.asu.edu/

[80] C. Yu and Z. Wei, "Predictive Technology Model for Nano-CMOS Design Exploration," in *1st International Conference on Nano-Networks and Workshops (NanoNet '06)*, 2006, pp. 1-5.

[81] H. Sato, E. C. I. Enobio, M. Yamanouchi, S. Ikeda, S. Fukami, S. Kanai, F. Matsukura, and H. Ohno, "Properties of magnetic tunnel junctions with a MgO/CoFeB/Ta/CoFeB/MgO recording structure down to junction diameter of 11 nm," *Applied Physics Letters,* vol. 105, p. 062403, 2014.

[82] A. Deac, K. J. Lee, Y. Liu, O. Redon, M. Li, P. Wang, J. P. Nozi√®res, and B. Dieny, "Current-induced magnetization switching in exchange-biased spin valves for current-perpendicular-to-plane giant magnetoresistance heads," *Physical Review B,* vol. 73, p. 064414, 2006.

[83] M. Hatami, G. E. W. Bauer, Q. Zhang, and P. J. Kelly, "Thermal Spin-Transfer Torque in Magnetoelectronic Devices," *Physical Review Letters,* vol. 99, p. 066603, 2007.

[84] S. Bandiera, R. C. Sousa, M. M. de Castro, C. Ducruet, C. Portemont, S. Auffret, L. Vila, I. L. Prejbeanu, B. Rodmacq, and B. Dieny, "Spin transfer torque switching assisted by thermally induced anisotropy reorientation in perpendicular magnetic tunnel junctions," *Applied Physics Letters,* vol. 99, pp. 202507-3, 2011.

[85] Y. K. Kato, R. C. Myers, A. C. Gossard, and D. D. Awschalom, "Observation of the Spin Hall Effect in Semiconductors," *Science,* vol. 306, pp. 1910-1913, 2004.

[86] C.-F. Pai, L. Liu, Y. Li, H. W. Tseng, D. C. Ralph, and R. A. Buhrman, "Spin transfer torque devices utilizing the giant spin Hall effect of tungsten," *Applied Physics Letters,* vol. 101, pp. 122404-4, 2012.

[87] G. Yu, P. Upadhyaya, Y. Fan, J. G. Alzate, W. Jiang, K. L. Wong, S. Takei, S. A. Bender, L.-T. Chang, Y. Jiang, M. Lang, J. Tang, Y. Wang, Y. Tserkovnyak, P. K. Amiri, and K. L. Wang, "Switching of perpendicular magnetization by spin-orbit torques in the absence of external magnetic fields," *Nat Nano,* vol. 9, pp. 548-554, 2014.

[88] L. Liu, O. J. Lee, T. J. Gudmundsen, D. C. Ralph, and R. A. Buhrman, "Current-Induced Switching of Perpendicularly Magnetized Magnetic Layers Using Spin Torque from the Spin Hall Effect," *Physical Review Letters,* vol. 109, p. 096602, 2012.

[89] A. Brataas and K. M. D. Hals, "Spin-orbit torques in action," *Nat Nano,* vol. 9, pp. 86-88, 2014.

[90] D. E. Nikonov and I. A. Young, "Overview of Beyond-CMOS Devices and a Uniform Methodology for Their Benchmarking," *Proceedings of the IEEE,* vol. 101, pp. 2498-2533, 2013.

[91] D. Nikonov. (2013). *Beyond CMOS computing: Magnetoelectric Switching*. Available: http://nanohub.org/resources/18358/download/NikonovBeyondCMOS_10_magnetoelectric.pdf

[92] D. E. Nikonov and I. A. Young, "Benchmarking spintronic logic devices based on magnetoelectric oxides," *Journal of Materials Research,* vol. 29, pp. 2109-2115, 2014.

[93] O. B. Oleg, R.-D. Pedro, R. D. Tamene, and S. S. Valeri, "Controlling magnetism on metal surfaces with non-magnetic means: electric fields and surface charging," *Journal of Physics: Condensed Matter,* vol. 26, p. 093001, 2014.

[94] N. A. Spaldin and M. Fiebig, "The Renaissance of Magnetoelectric Multiferroics," *Science,* vol. 309, pp. 391-392, July 15, 2005 2005.

[95] F. Manfred, "Revival of the magnetoelectric effect," *Journal of Physics D: Applied Physics,* vol. 38, p. R123, 2005.

[96] R. Ramesh and N. A. Spaldin, "Multiferroics: progress and prospects in thin films," *Nat Mater,* vol. 6, pp. 21-29, 2007.

[97] J. T. Heron, M. Trassin, K. Ashraf, M. Gajek, Q. He, S. Y. Yang, D. E. Nikonov, Y. H. Chu, S. Salahuddin, and R. Ramesh, "Electric-field-induced magnetization reversal in a ferromagnet-multiferroic heterostructure," *Physical review letters,* vol. 107, p. 217202, 2011.

[98] S. Cherepov, P. Khalili Amiri, J. G. Alzate, K. Wong, M. Lewis, P. Upadhyaya, J. Nath, M. Bao, A. Bur, T. Wu, G. P. Carman, A. Khitun, and K. L. Wang, "Electric-field-induced spin wave generation using multiferroic magnetoelectric cells," *Applied Physics Letters,* vol. 104, p. 082403, 2014.

[99] W. Tao, A. Bur, P. Zhao, K. P. Mohanchandra, K. Wong, K. L. Wang, C. S. Lynch, and G. P. Carman, "Giant electric-field-induced reversible and permanent magnetization reorientation on magnetoelectric Ni/(011) [Pb(Mg1/3Nb2/3)O3](1−x)–[PbTiO3]x heterostructure," *Applied Physics Letters,* vol. 98, p. 012504, 2011.

[100] J.-M. Hu, Z. Li, L.-Q. Chen, and C.-W. Nan, "High-density magnetoresistive random access memory operating at ultralow voltage at room temperature," *Nat Commun,* vol. 2, p. 553, 11/22/online 2011.

[101] H. Ohno, D. Chiba, F. Matsukura, T. Omiya, E. Abe, T. Dietl, Y. Ohno, and K. Ohtani, "Electric-field control of ferromagnetism," *Nature,* vol. 408, pp. 944-946, 2000.

[102] I. V. Ovchinnikov and K. L. Wang, "Voltage sensitivity of Curie temperature in ultrathin metallic films," *Physical Review B,* vol. 80, p. 012405, 2009.

[103] D. Chiba, S. Fukami, K. Shimamura, N. Ishiwata, K. Kobayashi, and T. Ono, "Electrical control of the ferromagnetic phase transition in cobalt at room temperature," *Nat Mater,* vol. 10, pp. 853-856, 2011.

[104] R. O. Cherifi, V. Ivanovskaya, L. C. Phillips, A. Zobelli, I. C. Infante, E. Jacquet, V. Garcia, S. Fusil, P. R. Briddon, N. Guiblin, A. Mougin, A. A. Ünal, F. Kronast, S. Valencia, B. Dkhil, A. Barthélémy, and M. Bibes, "Electric-field control of magnetic order above room temperature," *Nat Mater,* vol. 13, pp. 345-351, 2014.

[105] X. Marti, I. Fina, C. Frontera, J. Liu, P. Wadley, Q. He, R. J. Paull, J. D. Clarkson, J. Kudrnovský, I. Turek, J. Kuneš, D. Yi, J. H. Chu, C. T. Nelson, L. You, E. Arenholz, S. Salahuddin, J. Fontcuberta, T. Jungwirth, and R. Ramesh, "Room-temperature antiferromagnetic memory resistor," *Nat Mater,* vol. 13, pp. 367-374, 2014.

[106] S. Yoichi, M. Takuto, N. Takayuki, S. Teruya, S. Masashi, and S. Yoshishige, "Voltage-Assisted Magnetization Switching in Ultrathin Fe 80 Co 20 Alloy Layers," *Applied Physics Express,* vol. 2, p. 063001, 2009.

[107] M. Endo, S. Kanai, S. Ikeda, F. Matsukura, and H. Ohno, "Electric-field effects on thickness dependent magnetic anisotropy of sputtered MgO/Co40Fe40B20/Ta structures," *Applied Physics Letters,* vol. 96, p. 212503, 2010.

[108] T. Nozaki, Y. Shiota, M. Shiraishi, T. Shinjo, and Y. Suzuki, "Voltage-induced perpendicular magnetic anisotropy change in magnetic tunnel junctions," *Applied Physics Letters,* vol. 96, p. 022506, 2010.

[109] J. Zhu, J. A. Katine, G. E. Rowlands, Y.-J. Chen, Z. Duan, J. G. Alzate, P. Upadhyaya, J. Langer, P. K. Amiri, K. L. Wang, and I. N. Krivorotov, "Voltage-Induced Ferromagnetic Resonance in Magnetic Tunnel Junctions," *Physical Review Letters,* vol. 108, p. 197203, 2012.

[110] T. Nozaki, Y. Shiota, S. Miwa, S. Murakami, F. Bonell, S. Ishibashi, H. Kubota, K. Yakushiji, T. Saruya, A. Fukushima, S. Yuasa, T. Shinjo, and Y. Suzuki, "Electric-field-induced ferromagnetic resonance excitation in an ultrathin ferromagnetic metal layer," *Nat Phys,* vol. 8, pp. 491-496, 2012.

[111] P. Upadhyaya, R. Dusad, S. Hoffman, Y. Tserkovnyak, J. G. Alzate, P. K. Amiri, and K. L. Wang, "Electric field induced domain-wall dynamics: Depinning and chirality switching," *Physical Review B,* vol. 88, p. 224422, 2013.

[112] J. G. Alzate, P. K. Amiri, S. Cherepov, J. Zhu, P. Upadhyaya, M. Lewis, I. N. Krivorotov, J. Katine, J. Langer, K. Galatsis, and K. L. Wang, "Voltage-Induced Switching of CoFeB-MgO Magnetic Tunnel Junctions," in *56th Conference on Magnetism and Magnetic Materials (MMM)*, 2011, pp. EG-11.

[113] J. G. Alzate, P. K. Amiri, P. Upadhyaya, S. S. Cherepov, J. Zhu, M. Lewis, R. Dorrance, J. A. Katine, J. Langer, and K. Galatsis, "Voltage-induced switching of nanoscale magnetic tunnel junctions," in *IEEE International Electron Devices Meeting (IEDM)* 2012, pp. 29.5.1-4.

[114] W.-G. Wang, M. Li, S. Hageman, and C. L. Chien, "Electric-field-assisted switching in magnetic tunnel junctions," *Nat Mater,* vol. 11, pp. 64-68, 2012.

[115] Y. Shiota, T. Nozaki, F. Bonell, S. Murakami, T. Shinjo, and Y. Suzuki, "Induction of coherent magnetization switching in a few atomic layers of FeCo using voltage pulses," *Nat Mater,* vol. 11, pp. 39-43, 2012.

[116] J. M. Rondinelli, M. Stengel, and N. A. Spaldin, "Carrier-mediated magnetoelectricity in complex oxide heterostructures," *Nat Nano,* vol. 3, pp. 46-50, 2008.

[117] P. V. Ong, N. Kioussis, P. K. Amiri, J. G. Alzate, K. L. Wang, G. P. Carman, J. Hu, and R. Wu, "Electric field control and effect of Pd capping on magnetocrystalline anisotropy in FePd thin films: A first-principles study," *Physical Review B,* vol. 89, p. 094422, 2014.

[118] H. X. Yang, M. Chshiev, B. Dieny, J. H. Lee, A. Manchon, and K. H. Shin, "First-principles investigation of the very large perpendicular magnetic anisotropy at Fe|MgO and Co|MgO interfaces," *Physical Review B,* vol. 84, p. 054401, 2011.

[119] M. K. Niranjan, C.-G. Duan, S. S. Jaswal, and E. Y. Tsymbal, "Electric field effect on magnetization at the Fe/MgO(001) interface," *Applied Physics Letters,* vol. 96, p. 072503, 2010.

[120] K. H. He, J. S. Chen, and Y. P. Feng, "First principles study of the electric field effect on magnetization and magnetic anisotropy of FeCo/MgO(001) thin film," *Applied Physics Letters,* vol. 99, p. 072503, 2011.

[121] A. Manchon and S. Zhang, "Theory of spin torque due to spin-orbit coupling," *Physical Review B,* vol. 79, p. 094422, 2009.

[122] T. Liu, J. W. Cai, and L. Sun, "Large enhanced perpendicular magnetic anisotropy in CoFeB/MgO system with the typical Ta buffer replaced by an Hf layer," *AIP Advances,* vol. 2, p. 032151, 2012.

[123] N. Takayuki, Y. Kay, T. Shingo, S. Masaki, M. Rie, K. Makoto, K. Hitoshi, F. Akio, and Y. Shinji, "Voltage-Induced Magnetic Anisotropy Changes in an Ultrathin FeB Layer Sandwiched between Two MgO Layers," *Applied Physics Express,* vol. 6, p. 073005, 2013.

[124] Y. Shiota, F. Bonell, S. Miwa, N. Mizuochi, T. Shinjo, and Y. Suzuki, "Opposite signs of voltage-induced perpendicular magnetic anisotropy change in CoFeB|MgO junctions with different underlayers," *Applied Physics Letters,* vol. 103, p. 082410, 2013.

[125] A. A. Khan, J. Schmalhorst, A. Thomas, O. Schebaum, and G. Reiss, "Dielectric breakdown in Co–Fe–B/MgO/Co–Fe–B magnetic tunnel junction," *Journal of Applied Physics,* vol. 103, p. 123705, 2008.

[126] C. Yoshida, M. Kurasawa, L. Young Min, K. Tsunoda, M. Aoki, and Y. Sugiyama, "A study of dielectric breakdown mechanism in CoFeB/MgO/CoFeB magnetic tunnel junction," in *IEEE International Reliability Physics Symposium*, 2009, pp. 139-142.

[127] A. Rajanikanth, T. Hauet, F. Montaigne, S. Mangin, and S. Andrieu, "Magnetic anisotropy modified by electric field in V/Fe/MgO(001)/Fe epitaxial magnetic tunnel junction," *Applied Physics Letters,* vol. 103, p. 062402, 2013.

[128] U. Bauer, M. Przybylski, J. Kirschner, and G. S. D. Beach, "Magnetoelectric Charge Trap Memory," *Nano Letters,* vol. 12, pp. 1437-1442, 2012.

[129] F. Bonell, S. Murakami, Y. Shiota, T. Nozaki, T. Shinjo, and Y. Suzuki, "Large change in perpendicular magnetic anisotropy induced by an electric field in FePd ultrathin films," *Applied Physics Letters,* vol. 98, p. 232510, 2011.

[130] T. Seki, M. Kohda, J. Nitta, and K. Takanashi, "Coercivity change in an FePt thin layer in a Hall device by voltage application," *Applied Physics Letters,* vol. 98, p. 212505, 2011.

[131] K. Kita, D. W. Abraham, M. J. Gajek, and D. C. Worledge, "Electric-field-control of magnetic anisotropy of Co0.6Fe0.2B0.2/oxide stacks using reduced voltage," *Journal of Applied Physics,* vol. 112, p. 033919, 2012.

[132] A. J. Schellekens, A. van den Brink, J. H. Franken, H. J. M. Swagten, and B. Koopmans, "Electric-field control of domain wall motion in perpendicularly magnetized materials," *Nat Commun,* vol. 3, p. 847, 2012.

[133] C.-G. Duan, J. P. Velev, R. F. Sabirianov, Z. Zhu, J. Chu, S. S. Jaswal, and E. Y. Tsymbal, "Surface Magnetoelectric Effect in Ferromagnetic Metal Films," *Physical Review Letters,* vol. 101, p. 137201, 2008.

[134] K. Nakamura, T. Akiyama, T. Ito, M. Weinert, and A. J. Freeman, "Role of an interfacial FeO layer in the electric-field-driven switching of magnetocrystalline anisotropy at the Fe/MgO interface," *Physical Review B,* vol. 81, p. 220409, 2010.

[135] P. Khalili Amiri, P. Upadhyaya, J. G. Alzate, and K. L. Wang, "Electric-field-induced thermally assisted switching of monodomain magnetic bits," *Journal of Applied Physics,* vol. 113, p. 013912, 2013.

[136] M. Beleggia, M. D. Graef, Y. T. Millev, D. A. Goode, and G. Rowlands, "Demagnetization factors for elliptic cylinders," *Journal of Physics D: Applied Physics,* vol. 38, p. 3333, 2005.

[137] H. Sato, M. Yamanouchi, S. Ikeda, S. Fukami, F. Matsukura, and H. Ohno, "Perpendicular-anisotropy CoFeB-MgO magnetic tunnel junctions with a MgO/CoFeB/Ta/CoFeB/MgO recording structure," *Applied Physics Letters,* vol. 101, p. 022414, 2012.

[138] S. Hoffman, Y. Tserkovnyak, P. Khalili Amiri, and K. L. Wang, "Magnetic bit stability: Competition between domain-wall and monodomain switching," *Applied Physics Letters,* vol. 100, p. 212406, 2012.

[139] Z. Or-Bach. (2014). *28nm – The Last Node of Moore's Law*. Available: http://www.eetimes.com/author.asp?section_id=36&doc_id=1321536&&elq=e83a21f63e5a432a9de62ddc673e281d&elqCampaignId=18060

[140] Z. Or-Bach. (2014). *Embedded SRAM Scaling is Broken and with it Moore's Law*. Available: http://www.monolithic3d.com/blog/the-most-expensive-sram-in-the-world-20

[141] S. Mittal, J. S. Vetter, and D. Li, "A Survey Of Architectural Approaches for Managing Embedded DRAM and Non-volatile On-chip Caches," *IEEE Transactions on Parallel and Distributed Systems,* pp. 1-14, 2014.

[142] C. J. Xue, S. Guangyu, Z. Youtao, J. J. Yang, C. Yiran, and L. Hai, "Emerging non-volatile memories: Opportunities and challenges," in *Proceedings of the 9th International Conference on Hardware/Software Codesign and System Synthesis (CODES+ISSS)*, 2011, pp. 325-334.

[143] P. K. Amiri and K. L. Wang, "Low-power MRAM for nonvolatile electronics: Electric field control and spin-orbit torques," in *IEEE 6th International Memory Workshop (IMW)*, 2014, pp. 1-4.

[144] D. V. Berkov and J. Miltat, "Spin-torque driven magnetization dynamics: Micromagnetic modeling," *Journal of Magnetism and Magnetic Materials,* vol. 320, pp. 1238-1259, 2008.

[145] R. Dorrance, "Modeling and Design of STT-MRAMs," Thesis for Master of Science in Electrical Engineering, UCLA, 2011.

[146] S. Zhang, P. M. Levy, and A. Fert, "Mechanisms of Spin-Polarized Current-Driven Magnetization Switching," *Physical Review Letters,* vol. 88, p. 236601, 2002.

[147] G. Tatara and H. Kohno, "Theory of Current-Driven Domain Wall Motion: Spin Transfer versus Momentum Transfer," *Physical Review Letters,* vol. 92, p. 086601, 2004.

[148] D. Srinivasan, "Compact Modeling of STT-RAM and MeRAM: A Verilog-A model of Magnetic Tunnel Junction Behavioral Dynamics," Project for Master of Science in Electrical Engineering, UCLA, 2013.

[149] D. S. Matic, "A Magnetic Tunnel Junction Compact Model for STT-RAM and MeRAM," Project for Master of Science in Electrical Engineering, UCLA, 2013.

[150] J. Z. Sun, "Spin angular momentum transfer in current-perpendicular nanomagnetic junctions," *IBM Journal of Research and Development,* vol. 50, pp. 81-100, 2006.

[151] W. F. Brown, "Thermal Fluctuations of a Single-Domain Particle," *Physical Review,* vol. 130, pp. 1677-1686, 06/01/ 1963.

[152] G. Grinstein and R. H. Koch, "Coarse Graining in Micromagnetics," *Physical Review Letters,* vol. 90, p. 207201, 05/19/ 2003.

[153] S.-C. Oh, S.-Y. Park, A. Manchon, M. Chshiev, J.-H. Han, H.-W. Lee, J.-E. Lee, K.-T. Nam, Y. Jo, Y.-C. Kong, B. Dieny, and K.-J. Lee, "Bias-voltage dependence of perpendicular spin-transfer torque in asymmetric MgO-based magnetic tunnel junctions," *Nat Phys,* vol. 5, pp. 898-902, 2009.

[154] C. A. F. Vaz, J. A. C. Bland, and G. Lauhoff, "Magnetism in ultrathin film structures," *Reports on Progress in Physics,* vol. 71, p. 056501, 2008.

[155] H. B. Callen and E. Callen, "The present status of the temperature dependence of magnetocrystalline anisotropy, and the l(l+1)2 power law," *Journal of Physics and Chemistry of Solids,* vol. 27, pp. 1271-1285, 1966.

[156] J. C. Slonczewski, "Conductance and exchange coupling of two ferromagnets separated by a tunneling barrier," *Physical Review B,* vol. 39, pp. 6995-7002, 1989.

[157] N. W. Ashcroft and N. D. Mermin, *Solid State Physics* vol. 1976, 1976.

[158] K. Zakeri, T. Kebe, J. Lindner, and M. Farle, "Power-law behavior of the temperature dependence of magnetic anisotropy of uncapped ultrathin Fe Films on GaAs(001)," *Physical Review B,* vol. 73, p. 052405, 2006.

[159] Á. Buruzs, P. Weinberger, L. Szunyogh, L. Udvardi, P. I. Chleboun, A. M. Fischer, and J. B. Staunton, "Ab initio theory of temperature dependence of magnetic anisotropy in layered systems: Applications to thin Co films on Cu(100)," *Physical Review B,* vol. 76, p. 064417, 2007.

[160] J. B. Staunton, L. Szunyogh, A. Buruzs, B. L. Gyorffy, S. Ostanin, and L. Udvardi, "Temperature dependence of magnetic anisotropy: An ab initio approach," *Physical Review B,* vol. 74, p. 144411, 2006.

[161] R. Skomski, O. N. Mryasov, J. Zhou, and D. J. Sellmyer, "Finite-temperature anisotropy of magnetic alloys," *Journal of Applied Physics,* vol. 99, p. 08E916, 2006.

[162] J. B. Staunton, S. Ostanin, S. S. A. Razee, B. L. Gyorffy, L. Szunyogh, B. Ginatempo, and E. Bruno, "Temperature Dependent Magnetic Anisotropy in Metallic Magnets from an Ab Initio Electronic Structure Theory: L1_{0}-Ordered FePt," *Physical Review Letters,* vol. 93, p. 257204, 2004.

[163] R. Skomski, A. Kashyap, and D. J. Sellmyer, "Finite-temperature anisotropy of PtCo magnets," *IEEE Transactions on Magnetics,* vol. 39, pp. 2917-2919, 2003.

[164] S. Okamoto, N. Kikuchi, O. Kitakami, T. Miyazaki, Y. Shimada, and K. Fukamichi, "Chemical-order-dependent magnetic anisotropy and exchange stiffness constant of FePt (001) epitaxial films," *Physical Review B,* vol. 66, p. 024413, 2002.

[165] J. U. Thiele, K. R. Coffey, M. F. Toney, J. A. Hedstrom, and A. J. Kellock, "Temperature dependent magnetic properties of highly chemically ordered Fe55−xNixPt45L10 films," *Journal of Applied Physics,* vol. 91, pp. 6595-6600, 2002.

[166] O. N. Mryasov, U. Nowak, K. Y. Guslienko, and R. W. Chantrell, "Temperature-dependent magnetic properties of FePt: Effective spin Hamiltonian model," *EPL (Europhysics Letters),* vol. 69, p. 805, 2005.

[167] M. Getzlaff, *Fundamentals of magnetism*: Springer, 2007.

[168] J. M. Beaujour, D. Ravelosona, I. Tudosa, E. E. Fullerton, and A. D. Kent, "Ferromagnetic resonance linewidth in ultrathin films with perpendicular magnetic anisotropy," *Physical Review B,* vol. 80, p. 180415, 2009.

[169] C. Chappert, K. L. Dang, P. Beauvillain, H. Hurdequint, and D. Renard, "Ferromagnetic resonance studies of very thin cobalt films on a gold substrate," *Physical Review B,* vol. 34, pp. 3192-3197, 1986.

[170] A. Kozioł-Rachwał, W. Skowroński, T. Ślęzak, D. Wilgocka-Ślęzak, J. Przewoźnik, T. Stobiecki, Q. H. Qin, S. van Dijken, and J. Korecki, "Room-temperature perpendicular magnetic anisotropy of MgO/Fe/MgO ultrathin films," *Journal of Applied Physics,* vol. 114, p. 224307, 2013.

[171] P. J. Jensen and K. H. Bennemann, "Magnetic structure of films: Dependence on anisotropy and atomic morphology," *Surface Science Reports,* vol. 61, pp. 129-199, 2006.

[172] Y. Wang, D. Wei, K.-Z. Gao, J. Cao, and F. Wei, "The role of inhomogeneity of perpendicular anisotropy in magnetic properties of ultra thin CoFeB film," *Journal of Applied Physics,* vol. 115, p. 053901, 2014.

[173] I. Satoshi, M. Qinli, K. Takahide, M. Shigemi, A. Yasuo, and M. Terunobu, "Damping of Magnetization Precession in Perpendicularly Magnetized CoFeB Alloy Thin Films," *Applied Physics Express,* vol. 5, p. 083001, 2012.

[174] K. Makoto, I. Hiroshi, T. Tomohiro, Y. Kay, K. Hitoshi, F. Akio, A. Koji, and Y. Shinji, "Effect of MgO Cap Layer on Gilbert Damping of FeB Electrode Layer in MgO-Based Magnetic Tunnel Junctions," *Applied Physics Express,* vol. 6, p. 073002, 2013.

[175] M. Kotaro, Y. Michihiko, S. Hideo, I. Shoji, K. Shun, M. Fumihiro, and O. Hideo, "Size Dependence of Magnetic Properties of Nanoscale CoFeB–MgO Magnetic Tunnel Junctions with Perpendicular Magnetic Easy Axis Observed by Ferromagnetic Resonance," *Applied Physics Express,* vol. 6, p. 063002, 2013.

[176] M. Urbaniak. (2012). *Magnetic anisotropy*. Available: http://www.ifmpan.poznan.pl/~urbaniak/Wyklady2012/urbifmpan2012lect5_03.pdf

[177] S. Kanai, Y. Nakatani, M. Yamanouchi, S. Ikeda, F. Matsukura, and H. Ohno, "In-plane magnetic field dependence of electric field-induced magnetization switching," *Applied Physics Letters,* vol. 103, p. 072408, 2013.

[178] C. Kittel, "On the Theory of Ferromagnetic Resonance Absorption," *Physical Review,* vol. 73, pp. 155-161, 1948.

[179] J. C. Sankey, Y.-T. Cui, J. Z. Sun, J. C. Slonczewski, R. A. Buhrman, and D. C. Ralph, "Measurement of the spin-transfer-torque vector in magnetic tunnel junctions," *Nat Phys,* vol. 4, pp. 67-71, 2008.

[180] Z. Li and S. Zhang, "Thermally assisted magnetization reversal in the presence of a spin-transfer torque," *Physical Review B,* vol. 69, p. 134416, 2004.

[181] R. Skomski, J. Zhou, R. D. Kirby, and D. J. Sellmyer, "Micromagnetic energy barriers," *Journal of Applied Physics,* vol. 99, p. 08B906, 2006.

[182] R. Dorrance, J. G. Alzate, S. S. Cherepov, P. Upadhyaya, I. N. Krivorotov, J. A. Katine, J. Langer, K. L. Wang, P. K. Amiri, and D. Markovic, "Diode-MTJ Crossbar Memory Cell Using Voltage-Induced Unipolar Switching for High-Density MRAM," *IEEE Electron Device Letters,* vol. 34, pp. 753-755, 2013.

[183] I. N. Krivorotov, G. E. Rowlands, T. Rahman, J. A. Katine, J. Langer, A. Lyle, H. Zhao, J. G. Alzate, A. A. Kovalev, Y. Tserkovnyak, Z. M. Zeng, H. W. Jiang, K. Galatsis, Y. M. Huai, P. K. Amiri, K. L. Wang, and J. Wang, "Ultrafast spin torque memory based on magnetic tunnel junctions with combined in-plane and perpendicular polarizers," in *70th Annual Device Research Conference (DRC)* 2012, pp. 211-212.

[184] Y. Shiota, S. Miwa, T. Nozaki, F. Bonell, N. Mizuochi, T. Shinjo, H. Kubota, S. Yuasa, and Y. Suzuki, "Pulse voltage-induced dynamic magnetization switching in magnetic tunneling junctions with high resistance-area product," *Applied Physics Letters,* vol. 101, p. 102406, 2012.

[185] S. Kanai, M. Yamanouchi, S. Ikeda, Y. Nakatani, F. Matsukura, and H. Ohno, "Electric field-induced magnetization reversal in a perpendicular-anisotropy CoFeB-MgO magnetic tunnel junction," *Applied Physics Letters,* vol. 101, p. 122403, 2012.

[186] Z. Wang, Y. Zhou, J. Zhang, and Y. Huai, "Write Error Rate in Spin Transfer Torque Magnetic Random Access Memory," *Spin,* vol. 02, p. 1240001, 2012.

[187] J. G. Alzate, K. L. Wang, and P. K. Amiri, "Voltage-controlled magnetic memory element with canted magnetization," U.S. Patent Application 14/101,260 Patent, 2013.